https://doi.org/10.15388/vu.thesis.904
https://orcid.org/0009-0001-2582-8766

VILNIUS UNIVERSITY
CENTER FOR PHYSICAL SCIENCES AND TECHNOLOGY

Povilas Jurkšaitis

Fluorescence Dynamics of Plasmon-Exciton Polaritonic States

DOCTORAL DISSERTATION

Natural Sciences,
Physics (N 002)

VILNIUS 2026

This dissertation was written between 2021 and 2026 at Center for Physical Sciences and Technology.

Academic supervisor:
Prof. Dr. Zigmas Balevičius (Center for Physical Sciences and Technology, Natural Sciences, Physics – N 002).

Dissertation Defense Panel:

Chairman – Prof. Habil. Dr. Sigitas Tamulevičius (Kaunas University of Technologies, Natural Sciences, Physics, N 002).

Members:
Prof. Dr. Jonas Gradauskas (Center for Physical Sciences and Technology, Natural Sciences, Physics, N 002),
Prof. Dr. Saulius Juodkazis (Swinburne University of Technology, Natural Sciences, Physics, N 002),
Dr. Gediminas Račiukaitis (Center for Physical Sciences and Technology, Natural Sciences, Physics, N 002),
Dr. Irmantas Kašalynas (Center for Physical Sciences and Technology, Natural Sciences, Physics, N 002).

The dissertation shall be defended at a public meeting of the Dissertation Defense Panel at 10:00 on 17 April 2026 in Room D401 of the Center for Physical Sciences and Technology.
Address: Saulėtekio av. 3, NFTMC, Room D401, Vilnius, Lithuania.
Tel. +370 5 264 9211; email: office@ftmc.lt.

https://doi.org/10.15388/vu.thesis.904
https://orcid.org/0009-0001-2582-8766

VILNIAUS UNIVERSITETAS
FIZINIŲ IR TECHNOLOGIJOS MOKSLŲ CENTRAS

Povilas Jurkšaitis

Plazmonų-Eksitonų Poliaritoninių Būsenų Fluorescencijos Dinamika

DAKTARO DISERTACIJA

Gamtos mokslai,
Fizika (N 002)

VILNIUS 2026

Disertacija rengta 2021–2026 metais Fizinių ir technologijos mokslų centre.

Mokslinis vadovas:
Prof. dr. Zigmas Balevičius (Fizinių ir technologijos mokslų centras, gamtos mokslai, fizika – N 002).

Gynimo taryba:
Pirmininkas – prof. habil. dr. Sigitas Tamulevičius (Kauno technologijos universitetas, gamtos mokslai, gamtos mokslai, fizika, N 002).

Nariai:
Prof. dr. Jonas Gradauskas (Fizinių ir technologijos mokslų centras, gamtos mokslai, fizika, N 002),
Prof. dr. Saulius Juodkazis (Svinburno universitetas, gamtos mokslai, fizika, N 002),
Dr. Gediminas Račiukaitis (Fizinių ir technologijos mokslų centras, gamtos mokslai, fizika, N 002),
Dr. Irmantas Kašalynas (Fizinių ir technologijos mokslų centras, gamtos mokslai, fizika, N 002).

Disertacija ginama viešame Gynimo tarybos posėdyje 2026 m. balandžio 17 d. 10:00. Nacionalinio fizinių ir technologijos mokslų centro D401 auditorijoje. Adresas: Saulėtekio al. 3, NFTMC, D401 aud., Vilnius, Lietuva.
Tel. +370 5 264 9211; el. paštas: office@ftmc.lt.

ACKNOWLEDGEMENTS

First and foremost, I would like to express my gratitude to my supervisor Prof. dr. Zigmas Balevičius, for providing me with the opportunity to work on this dissertation topic. I am grateful for the opportunity to engage in scientific discussions and for the strong support and assistance provided throughout the years.

Secondly, I would like to thank dr. Vytautas Žičkus. The enthusiasm and the opportunities that he provided, including the opportunity to visit and work at the University of Glasgow, played a huge role during my dissertation years.

I would also like to thank dr. Ernesta Bužavaitė-Vertelienė for fruitful discussions and help with the publications, dr. Justina Anulytė for the preparation of the samples as well as the ellipsometric measurements and also Evita Spalinskaitė for the help.

Finally, I would like to thank my family for their support during my studies, and especially Dainora for her patience and continuous support.

CONTENT

LIST OF ABBREVIATIONS

AOI	angle of incidence
BFP	back focal plane
CS	coverslip
ER	exciton reservoir
FLIM	fluorescence lifetime imaging microscopy
FRET	Förster resonance energy transfer
FWHM	Full width half maximum
G	ground state
HSA	human serum albumin
IRF	instrument response function
LDOS	local density of states
LP	lower polariton
PL	photoluminescence
PMMA	poly(methyl methacrylate)
Q factor	quality factor
QE	quantum emitter
R6G	rhodamine 6G
SE	spectroscopic ellipsometry
SPP	surface plasmon polariton
SPR	surface plasmon resonance
SPAD	single photon avalanche diode
SPCE	surface plasmon coupled emission
TCSPC	time-correlated single-photon counting
TIR	total internal reflection
TIRE	total internal reflection ellipsometry
TIRF	total internal reflection fluorescence
UP	upper polariton

INTRODUCTION

When considering light, one usually discusses topics such as interference, diffraction, wave propagation, etc. These phenomena belong to the field of optics, which studies light composed of classical electromagnetic waves propagating in the far field ($d >> \lambda$), where d is propagation length. Practical applications of these optical phenomena have enabled the development of tools such as lasers, microscopes, optical fibres, to name a few. Moreover, these effects are usually investigated in the macroscale, meaning that the spatial features are much larger than the wavelength of the corresponding light [1]. This is no coincidence because classical optics is governed by diffraction, which forbids localization of light below a certain limit. This limit is referred to as the Abbe diffraction limit and is described as $\lambda/2NA$, where NA is numerical aperture [2]. This is around 200 - 300 nanometers in the visible range. Abbe's criterion was considered to be the ultimate limit, limited by the fundamental laws of physics. However, the shift began in the 1970s and 1980s when it was experimentally demonstrated that the diffraction limit can be overcome by making use of evanescent waves in the near field [3–6]. With the advent of nanotechnology, a new field of nanophotonics has started to emerge with the purpose of searching for new ways to control light at the nanoscale. Emerging new platforms comprising different materials, structures and configurations have allowed to confine electromagnetic fields to sub-wavelength dimensions, opening ways to observe new physical phenomena for both fundamental science and practical applications [7, 8]. Dimensions of nanophotonic devices are typically in the range between $1 - 1000$ nm. At such scales, classical optical approximations break down, with quantum and near-field effects becoming highly important. Some of the most popular platforms for nanophotonics include dielectric nanostructures [9], plasmonics [10], photonic crystal platforms and 2D materials [11]. Dielectric and photonic crystal platforms usually exhibit low optical losses with high Q factors, when compared with other platforms, however, they exhibit rather weak interaction capabilities. In contrast, plasmonic nanostructures exhibit high field confinement ($< \lambda/10$) and field enhancement leading to strong interactions, but are also affected by high loss due to electron collisions.

Confining electromagnetic fields down to sub-wavelength scales has also permitted the observation of new physical phenomena regarding light-matter interactions [12,13]. Evanescent fields arise together with high field confinement and enhancement. A well-known result, when considering light-matter interactions, occurs when placing the emitter, such as a fluorescence dye molecule or quantum dot, in a nanophotonic environment [14]. The resulting interaction between emitter and optical environment leads to changes in the density of states, resulting in enhanced or suppressed spontaneous emission, first predic-

ted by Purcell in 1946 [15]. This is also known as the *weak coupling* regime. Even more radical modifications of the excited state can be observed when the interaction strength g between an emitter and the nanophotonic structure is increased above the loss rate of the individual systems $g >> \kappa, \omega$. This leads to the hybridization of the cavity and emitter modes, resulting in the emergence of *polaritonic* states referred to as *strong coupling* regime [13,16]. Apart from a wide range of available nanoscale structures, there is a huge variety of emitter species used in nanophotonics, ranging from organic molecular dyes [17], quantum dots [18] to single molecules [16] or atoms [19], thus allowing to achieve new advancements in ultrafast nanophotonics [20, 21], chemistry [22, 23] and biological applications [24].

This thesis is dedicated to the investigation of the strong coupling regime in plasmonic nanostructures using fluorescent dye molecules and their application in nanophotonic devices and nanoscale optical sensing. Investigation of polaritonic states in the strong coupling regime was performed using nanostructures composed of continuous silver or gold films in conjunction with either Rhodamine 6G or Alexa633 molecular dyes.

Fluorescent molecular dye labeled human serum albumin (HSA) protein molecules were investigated when coupled with uniform gold nanolayers with a thickness of $45nm$. Numerical model using the effective Bruggeman approximation model was used to simulate optical response in the strong coupling regime. This revealed that the coupling strength was proportional to the molecular concentration on the gold surface, allowing for effective evaluation of labeled protein-complex mass adsorbed to the plasmonic sensor through optical response in TIRE configuration.

Another part of the dissertation is dedicated to the investigation of polariton lifetime dynamics. Polaritons were investigated using the time-correlated single photon counting technique. The investigation was performed using coupled surface plasmon polariton states in continuous silver (Ag) layers formed on a glass coverslip (CS) together with Rhodamine 6G fluorescence dye. Measured ellipsometric data indicated about strong coupling regime with coupling strengths of around 200 meV. Total internal reflection fluorescence (TIRF) was used for the generation of exciton reservoir states in back focal plane (BFP) imaging configuration for the evaluation of the dynamical mechanism governing polariton decay in strongly coupled systems. The investigation expanded the current understanding of coupling dynamics in plasmonic-excitonic systems.

Lastly, a part of the dissertation investigates spatiotemporal fluorescence lifetime characteristics in strongly coupled plasmonic-excitonic states between Rhodamine 6G and silver films. Normal mode splitting observed using total internal reflection ellipsometry was fitted using a coupled oscillator model with coupling strength $g = 160\ meV$. Modified BFP imaging was presented, which exploits spatial filtering technique in the conjugate Fourier plane, allowing the

investigation of direction-dependent polaritonic decay characteristics. The study presented here suggested new ways of obtaining angular characteristics in a back focal plane microscopy setup, which is crucial for nanophotonic devices.

Goals

- Examine strong coupling behaviour between SPP and labeled protein (HSA) molecules, focusing on the modified optical properties and sensing applications.
- Investigate the influence of the excitonic reservoir on the polariton decay dynamics under SPP-Rhodamine 6G strong coupling by introducing variable excitation parameters.
- Investigate angular polaritonic emission behaviour of strongly coupled SPP-Rhodamine 6G states using spatially filtered BFP measurement method.

Tasks of the research

- Investigate the optical response of labeled and non-labeled HSA molecules placed in the near field of gold nano-layer using numerically simulated dispersion data.
- Analyse the optical dispersion properties, and Rabi splitting under strong SPP-HSA coupling, and investigate the dependence on the molecular concentration.
- Evaluate strong coupling behaviour from SPP-R6G hybrid states and observe polaritonic emission under non-resonant excitation conditions.
- Investigate fluorescence lifetime decay dynamics of SPP-R6G hybrid states by incorporating variable angle excitation and fluorescence detection schemes.
- Analyse polaritonic decay dynamics using rate equation models to investigate the influence of exciton reservoir states.
- Investigate SPP-R6G strong coupling using a coupled oscillator model and evaluate coupling strength from TIRE ellipsometry data.
- Apply optical image processing configuration to fluorescence microscopy setup and obtain emission angle-dependent polaritonic lifetime characteristics.

Statements to be defended

- Normal mode splitting of the strong coupling regime between labeled protein excitons and plasmonic excitation enables protein concentration detection through the changes of coupling strength.

- The contribution of the exciton reservoir to the coherent energy exchange between plasmonic and excitonic parts in the hybrid polaritonic state can be controlled by the polariton excitation conditions.

- Spatial filtering of lifetimes in the back focal plane allows to distinguish between weak and strong coupling regimes for plasmon-exciton based polaritonic states.

Scientific novelty

Novelty of this study lies in the combined measurement of fluorescence emission intensity in the back focal plane with fluorescence lifetime decay under resonant and nonresonant conditions. This approach reveals the critical role of exciton reservoir transitions in the lifetime dynamics of plasmon–exciton polaritons in Rhodamine 6G. The measured fluorescence lifetimes, spanning hundreds of picoseconds, are far longer than the femtosecond scale lifetimes typically expected in plasmonic strong coupling regimes. This discrepancy indicates that the standard coupled oscillator model does not fully capture the dynamics of coherent energy exchange and that additional incoherent decay mechanisms, such as transitions from the exciton reservoir to the lower polaritonic branch, should be taken into account. This new insight provides a deeper understanding of light–matter interaction in the strong coupling regime and has practical implications for the design of quantum optical nanodevices, polaritonic lasers, and polariton condensation systems.

Recent advances in nanophotonics have enabled breakthroughs across spectroscopy, imaging, quantum optics, and sensing. Central to these developments are advanced optical characterization techniques, among which back focal plane (BFP) imaging has become an indispensable tool. In this work, we introduce a fluorescence lifetime resolved BFP imaging technique, representing a significant expansion of the conventional Fourier plane methodology. By implementing spatial filtering within a time-correlated single photon counting detection scheme, we directly measure angle dependent fluorescence lifetimes, enabling correlation between momentum-space emission and radiative decay dynamics. Combining lifetime and intensity information further allows direct evaluation of radiative rate enhancement across emission angles. This method introduces a new experimental dimension to BFP imaging, bridging k-space emission analysis with time-resolved photophysics, and opening opportunities to explore the spatiotemporal dynamics and collective quantum behaviour of hybrid nanophotonic systems.

Practical value

The practical value of this work lies in providing new experimental tools and insights for the design of next-generation nanophotonic and biosensing devices. By demonstrating angle-resolved fluorescence lifetime imaging in the Fourier domain, we introduce a powerful method to probe emission dynamics with angular resolution. This enables researchers to extract information about weakly and strongly coupled states that is compatible with existing BFP microscopy methods, offering a more complete picture of light–matter interactions. Such capability is especially important for the optimization of plasmonic sensors, optical filters, and devices where directionality and mode selectivity are critical.

In addition, our observation of exciton reservoir contributions to polaritonic lifetimes highlights the importance of incoherent decay pathways in strongly coupled systems. This understanding has practical implications for engineering longer-lived polaritonic states, which could improve the stability and efficiency of devices such as polaritonic lasers, quantum light sources, and nanoscale optical switches. Furthermore, by providing a more accurate framework for interpreting lifetime measurements in coupled systems, this work can guide the development of advanced biosensing techniques that rely on changes in coupling strength to detect molecular interactions. Together, these outcomes bridge fundamental physics with application-driven research, opening pathways toward innovative technologies in quantum nanophotonics, quantum optics, and advanced biomedical sensing.

Structure of the dissertation

The structure of this dissertation consists of five core chapters, each of which addresses critical aspects of the investigation of plasmonic strong coupling and potential applications in polaritonic lifetime estimation and optical biosensing. The dissertation is structured as follows:

Chapter 1 starts with a literature overview about scientific research carried out in the field and introduces core theoretical concepts needed for the investigation of strongly coupled plasmonic nanostructures.

Chapter 2 discusses the methodology of the thesis, which includes back focal plane imaging, time-correlated single photon counting, total internal reflection ellipsometry, sample fabrication, and photoluminescence techniques used during the research.

The main results are presented in the subsequent *Chapters 3* to *5*.

Chapter 3 studies polaritonic emission and fluorescence lifetime dynamics when influenced by the excitonic reservoir generated under resonant and non-resonant excitation.

Chapter 4 investigates the spatial filtering technique in a back focal plane

imaging configuration to detect direction-dependent polaritonic lifetime characteristics.

Chapter 5 introduces an optical polaritonic biosensing technique capable of detecting and evaluating labeled protein molecules adsorbed to the nanostructure using a plasmonic strong coupling regime.

*F*inally, conclusions of the dissertation are presented in the *Conclusions* chapter, which summarizes the main results, followed by a short *Summary* in the Lithuanian language.

Contribution of the author

Numerical simulation and data analysis describing the optical response of strongly coupled HSA molecules were performed by the author in discussion with the supervisor and co-authors. The author performed time-correlated single photon counting and back focal plane imaging experiments, including optical system design, assembly, and alignment. Introduced the spatial filtering technique from the initial idea to experimental verification and data acquisition. The author applied the coupled oscillator model for the determination of coupling strengths. The author participated in the experimental detection and measurements of angle-dependent polariton emission spectra. Interpretation and numerical simulation of polariton decay dynamics were performed by the author. All initial publication manuscripts were prepared by the author in discussion with the supervisor and co-authors. A significant contribution to the reviewers' comments was made by the author.

LIST OF PUBLICATIONS

P1 **P. Jurkšaitis**, J. Anulytė, E. Spalinskaitė, E. Bužavaitė-Vertelienė, V. Žičkus, I. Plikusienė Z. Balevičius, Spatially filtered back focal plane imaging for directional fluorescence lifetime study of polaritonic states, *Photonics* , 12, 1165, (2025), doi: 10.3390/photonics12121165.

P2 **P. Jurkšaitis**, J. Anulytė, E. Spalinskaitė, E. Bužavaitė-Vertelienė, V. Žičkus, D. Banevičius, K. Kazlauskas, Z. Balevičius, Plasmon-exciton polaritonic emission lifetime dynamics under strong coupling, *Nanophotonics*, 14, 14, 2485-2493, (2025), doi: 10.1515/nanoph-2025-0129.

P3 **P. Jurkšaitis**, E. Bužavaitė-Vertelienė, Z. Balevičius, Strong coupling between surface plasmon resonance and exciton of labeled protein-dye complex for immunosensing applications, *Int. J. Mol. Sci.*, 24, 3, 2009, (2023), doi: 10.3390/ijms24032029.

Conference presentations

C1 **P. Jurkšaitis**, J. Anulytė, D. Banevičius, E. Bužavaitė-Vertelienė, Z. Balevičius. Paviršinio plazmono ir R6G eksitono emisija stipriosios sąveikos režime, Fiztech, Vilnius, Lithuania, October 15-17, 2024, (oral)

C2 **P. Jurkšaitis**, V.Žičkus, A. Lyons, R. Alvarez-Mendoza, Z.Balevičius, D. Faccio. Hong-Ou-Mandel enhanced fluorescence interferometry. International conference on quantum optics and quantum information, Innsbruck, Austria, September 16-20, 2024, (poster).

C3 **P. Jurkšaiti**s, V.Žičkus, J. Anulytė, E. Bužavaitė-Vertelienė, Z.Balevičius. Surface plasmon coupled emission of Rhodamine 6G dye in strong coupling regime, Photon, Swansea, United Kingdom, September 2-6, 2024, (poster).

C4 **P. Jurkšaitis**, J. Anulytė, Z. Balevičius. Stipriosios sąveikos režimas tarp paviršinių plazmonų ir Rodamino 6G molekulių, Fiztech, Vilnius, Lithuania, October 18-19, 2023, (oral).

C5 **P. Jurkšaitis**, J. Anulytė, Z.Balevičius. Light-matter coupling between surface plasmon polaritons and Rhodamine 6G dye, Hybrid quantum systems, Viena, Austria, August 28 – September 1, 2023, (poster).

C6 **P. Jurkšaitis**, Z.Balevičius. Strong Light-matter coupling between surface plasmon polaritons and Rhodamine 6G dye, Advanced Materials and Technologies, Palanga, Lithuania, August 21 – 25, 2023, (poster)

C7 **P. Jurkšaiti**s, E. Bužavaitė-Vertelienė, Z. Balevičius. Strong coupling between surface plasmon resonance and exciton labeled protein-dye complex for immunosensing applications. 64th International conference for students of physics and natural sciences Open Readings, Vilnius, Lithuania, April 17-21, 2023 (poster)

C8 **P. Jurkšaiti**s, Z. Balevičius. Modelling of strong coupling between surface plasmon polaritons and protein-dye complex exciton of HSA antibody labeled with Rhodamine101 dye, Fiztech, Vilnius, Lithuania, October 19-20 2022 (poster)

1. LITERATURE REVIEW

1.1. Evanescence fields and total internal reflection

One of the most important phenomena in nanophotonics is the evanescent electromagnetic field. These fields have the characteristic of a plane wave $Ee^{i(kr-\omega t)}$, where E is the amplitude of the electric field. However, at least one component of the wavevector k is imaginary. This corresponds to the exponential decay of the wave along the direction defined by the imaginary wavevector component k, while still propagating along the direction described by real k. Therefore, evanescent fields can describe optical fields which are confined to subwavelength dimensions. Creation of an evanescent field requires a non-homogeneous environment and is usually observed at the interface between two media with different permittivities ϵ_1, ϵ_2 and permeabilities μ_1, μ_2 (Fig. 1.1). When a plane wave hits the interface between two media, part of the light will be reflected or refracted, depending on Fresnel's coefficients and Snell's Law. Increasing the angle of incidence increases the angle of reflection up until the critical angle, at which total internal reflection (TIR) occurs, indicating that all incident light is reflected and there is no refraction. Critical angle is defined as [8]:

$$\theta_c = \arcsin\left(\frac{n_1}{n_2}\right), \tag{1.1}$$

where n_1 and n_2 are the refractive indices of the two media, respectively. Ratio n_1/n_2 must be less than 1 for TIR to occur. For the glass/air interface, the critical angle is around 41.8°. Incidence above critical angle $\theta_1 > \theta_c$ results in an imaginary wavector k_z, thus a propagating evanescent field is created, which decays exponentially along the z axis. At an angle of 45° intensity of the evanescent wave falls to $1/e$ at a distance $\sim \lambda/2$. Increasing the angle even further, the decay will be even faster. The excited evanescent field decays exponentially perpendicular to the surface [8]:

$$I(z) = I(0)e^{-z/d}. \tag{1.2}$$

The penetration depth d of the evanescent wave into the lower-index medium is dependent on the wavelength of the incident light λ, and is given by [8]:

$$d = \frac{\lambda}{2\pi\sqrt{n_1^2 \sin^2\theta - n_2^2}}. \tag{1.3}$$

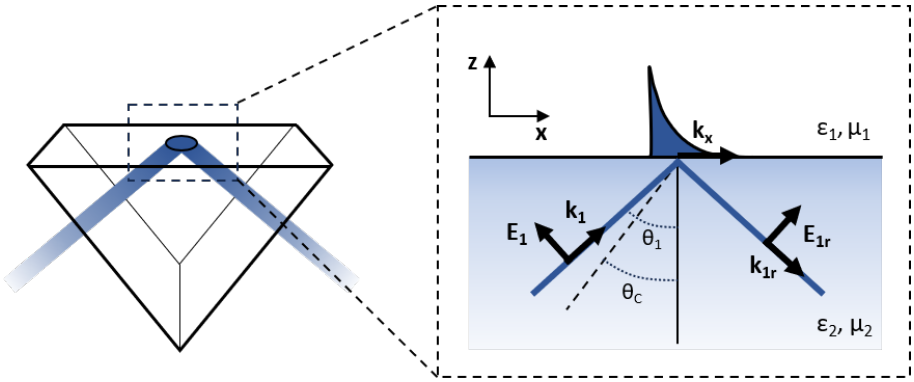

1.1 Fig. Evanescent waves during total internal reflection. Excitation light is directed at the prism/air interface, where the evanescent field is created upon hitting the interface at an angle greater than the critical angle $\theta_1 > \theta_c$.

Intensity of the evanescent wave is usually higher compared to the excitation beam, due to subwavelength dimensions. Much stronger enhancement can be achieved using metallic layers, which is governed by surface plasmonic resonance. One of the most important characteristics of an evanescent field is that it can be converted into propagating radiation upon interaction with matter. For example, by placing a second prism very close to the excited evanescent field (within the typical penetration depth), it is possible to partly convert the evanescent field into far-field radiation and obtain information about subwavelength structures. This is referred to as *frustrated total internal reflection* and plays an important role in probing light at the nanoscale.

1.2. **Surface plasmon polaritons**

Nanophotonics studies the interactions between electromagnetic field modes and various nanoscale structures. Research field, which discusses light interaction with metals, has been termed plasmonics or nanoplasmonics. These interactions with metals are mainly dictated by free electrons in the conduction band. Drude's model, which describes the electrical and thermal properties of the metal, shows that electrons in the metal oscillate 180° out of phase relative to the impinging electromagnetic field. This is the reason why most metals exhibit a very high reflectivity at optical and microwave frequencies. Moreover, free electrons within the metal can sustain charge-density oscillations, giving rise to distinctive resonances at optical frequencies. These modes are usually referred to as plasmons and are characterized by their plasma frequency. Noble metals such as gold and silver feature a dielectric function (the material's

response to an applied electric field), which is negative at optical frequencies, giving their distinctive look.

Optical modes such as plane and spherical waves form the basic concepts for understanding how light propagates. When considering light propagation in optical fibers, one typically uses optical modes confined within the waveguides. Optical modes confined at the interface between metal and dielectric material can be described using surface plasmon modes. More specifically, surface plasmon polaritons (SPP) emerge upon excitation of surface plasmons with an external light source at resonance angles, also known as SPR angle [25], where surface plasmons are the quanta of surface-bound charge oscillations. Electromagnetic wave couples to plasmons at the metal interface, forming a SPP at optical or infrared frequencies. Due to resonance conditions required to achieve these excitations, they are also called SPR modes. These modes exhibit several important characteristics, one of which is confinement on a subwavelength scale, which arise due to electronic properties intrinsic to the SPP mode. This makes plasmonic structures highly important for the development of coherent light sources at the nanoscale. In contrast to the previously mentioned classical optical modes, SPPs exhibit matter-like properties such as effective mass, a high degree of confinement, allowing for localization and propagation on nanometre scales, far below the Rayleigh diffraction limit. This allows to achieve high optical field confinement and enhancement at the metal interface [14]. By introducing various metallic nanostructures, such as corrugated surfaces or nanoparticles, it is possible to tune the resonance conditions of the excitation, making such structures attractive for optical sensing [26]. The ability of SPPs to achieve high electric field enhancement is crucial since it allows to facilitate strong light-matter coupling in the near field [7, 27]. Besides, such local field enhancement has already been used to boost fluorescence [14,28], lasing [29,30], and Raman scattering [31]. Mathematically, SPPs can be described as a solution to Maxwell's equations with boundary conditions, described by dielectric functions at the interface between metal and dielectric. The corresponding electric field E_i is [8]:

$$\mathbf{E}_i = (E_{ix},\, 0,\, E_{iz})\, e^{-k_i|z|} e^{i(k_i x - \omega t)}, \tag{1.4}$$

where E_{ix} and E_{iz} describe electric field along the x and z coordinates, respectively, k_i is the wavevector and ω is the frequency of light. Here i refers either to dielectric or metallic media. The equation shows that the field lies only in **x-z** plane and has no **y** component. Moreover, the wave exponentially decays in $\pm\mathbf{z}$ directions, which is typically $\sim$ 500nm in dielectric material and $\sim$ 30 nm in metallic environment [8], while propagating along **x** direction (interface between two media).

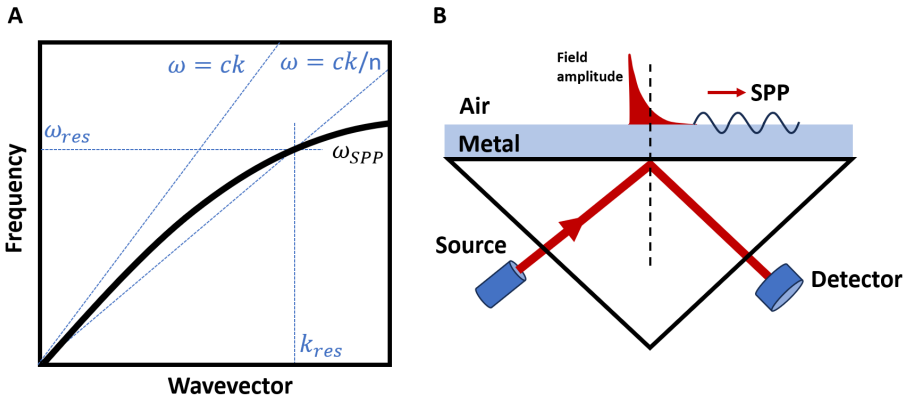

1.2 Fig. Excitation of surface plasmon waves: A) Dispersion relation of surface plasmon polariton; B) Experimental excitation of plasmonic waves using Kretschmann configuration.

Only p-polarized waves need to be considered, because no surface bound states exist for s-polarization. SPP can be described by a complex wavenumber $k_{spp} = k'_{spp} + ik''_{spp}$, which defines wave propagation (k'_{spp}) and damping (k''_{spp}) along the metal-dielectric interface. The energy-momentum dispersion relation can be described as (Fig. 1.2A) [8]:

$$k_{\text{spp}} = \frac{\omega}{c}\sqrt{\frac{\varepsilon_m \varepsilon_d}{\varepsilon_m + \varepsilon_d}}, \tag{1.5}$$

where ε_m and ε_d are frequency dependent relative permittivity of the metal and dielectric materials, respectively. The plasmon wavelength is always shorter compared to the same wavelength in a dielectric material and can be expressed as [8]:

$$\lambda_{\text{spp}} = \frac{2\pi}{k_{spp}} \approx \lambda\sqrt{\frac{\varepsilon_m + \varepsilon_d}{\varepsilon_m \varepsilon_d}}. \tag{1.6}$$

Energy and momentum conservation must be satisfied in order to excite SPPs, thus dispersion relations describing the relation between energy E and momentum k_{spp} must be taken into account. The wavevector k_{spp} corresponding to the surface plasmon is always larger compared to the freely propagating photon, therefore, SPPs can not decay directly or be excited by freely propagating photons, and some kind of wavevector matching technique is required. In order to achieve SPP excitation, several methods can be implemented, such as Otto or Kretschmann configurations, by performing excitation using a glass prism. In the Kretschmann configuration, light is incident from within the glass prism with a refractive index of n, which enhances the wavevector component to $nk_{||}$, allowing to excite surface plasmons (Fig. 1.2B). Increasing the incidence angle above the critical angle, total internal reflection (TIR) occurs, which produces exponentially decaying evanescent field along the metal. Therefore, SPPs can

be identified as a decrease in the reflected light when measured in reflection geometry. On the other hand, light can also radiate by the same process, which is usually called surface plasmon coupled emission (SPCE) [32]. Plasmons propagate along the metal surface as damped oscillatory waves with a propagation length described by:

$$L = \frac{1}{2k''_{\mathrm{sp}}}, \tag{1.7}$$

length of the propagation is defined as the distance at which the intensity of the electric field decays to $1/e$ ($\sim 37\%$). Similarly, the propagation depth d_p into the surrounding media is described as the distance from the surface equal to $1/e$ of the value. This is typically described by [8]:

$$d_p^{\mathrm{dielectric}} = \frac{\lambda}{2\pi}\sqrt{\frac{|\varepsilon'_m| + \varepsilon_d}{\varepsilon_d^2}}, \tag{1.8}$$

$$d_p^{\mathrm{metal}} = \frac{\lambda}{2\pi}\sqrt{\frac{|\varepsilon'_m| + \varepsilon_d}{\varepsilon_m^2}}. \tag{1.9}$$

Other excitation methods include Otto configuration (Fig. 1.3A), near-field probes [33, 34], single-quantum emitters [35], confined optical near-fields [36], fluorescence molecules [37], where direct excitation of surface plasmons can be accomplished locally. Near field coupling, such as excitation using fluorescence dye molecules, is especially important in the context of strong coupling, since the coupling is dependent on the distance between emitters and SPP modes. This enables to achieve high coupling rates, facilitating a strong coupling regime, which is mainly due to the fact that electric field amplitudes decay exponentially into surrounding media, reaching only ~ 30 nm into the metals. This spatial confinement at the metal surface leads to field enhancement, which facilitates strong coupling even in the strongly damped metallic environment. The biggest drawback when using plasmonic nanostructures is the high ohmic losses in metallic materials, which limit the propagation length of the SPP (Eq. 1.7). It is estimated that propagation lengths is ~ 60 µm for silver and ~ 10 µm for gold [8]. Higher propagation lengths can be achieved using localized surface plasmon resonance mode, which allows to reach propagation distances up to centimetre [13]. Due to internal losses, surface plasmon modes in metals usually suffer from low Q factor, typically in the range of $5 - 100$, however, low mode volume and high field enhancement help to facilitate interactions with plasmonic excitation.

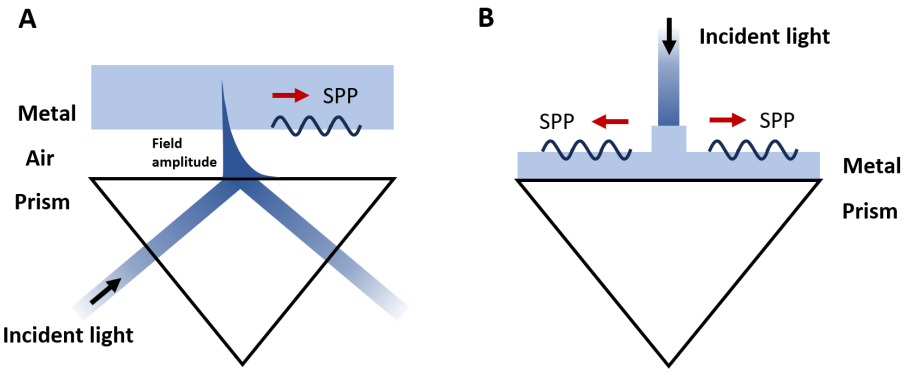

1.3 Fig. Excitation of surface plasmon polaritons using: (A) Otto configurations. SPP is excited when placed in the near field of an evanescent wave; (B) Excitation using nanoparticles or a grating.

Particularly interesting applications of SPP modes have emerged when considering optical sensing techniques [38, 39]. High SPP sensitivity to the refractive index of the bulk medium has become an important tool for studying various chemical and biological interactions [38]. Small changes in the local refractive index alter the SPP resonance angle and can be directly observed using spectroscopic techniques. This change of SPP resonance angle can be exploited to determine the thickness, optical constants of the layers formed on metal film [40]. These sensors can measure film thicknesses ranging from ~ 1 nm to ~ 35 nm, which are formed after absorption of molecules [41, 42]. Optical sensing of antibodies [39], proteins [43], hormones [44], viruses [45] has also been developed using SPP technology. The aforementioned sensing techniques are label free, however, SPPs can also be exploited in fluorescently labeled samples.

1.3. **Surface plasmon coupled emission and sensing**

Fluorescence detection methods have been rapidly increasing in the fields of biology, biotechnology, and medicine. Fluorescence has permitted numerous advances in sensing, medical diagnostics, and gene expression [14, 46, 47]. Randomly distributed excited fluorophores typically exhibit nearly isotropic emission in free space, and the collection efficiency of the signal is typically small (less than 1%) [32]. Recent advances in nanophotonics have allowed to increase the detection efficiency up to 50% when using plasmonic samples, allowing for increased sensitivity. This is achieved due to interactions between plasmons and fluorophores when placed in close proximity. Under strong coupling, polaritonic states decay via either scattering or emission of radiation. Polaritonic states exhibit emission characteristics of SPCE, which is typically

observed when coupled with plasmonic materials. Highly polarized SPCE is observed with a precisely defined direction of radiation.

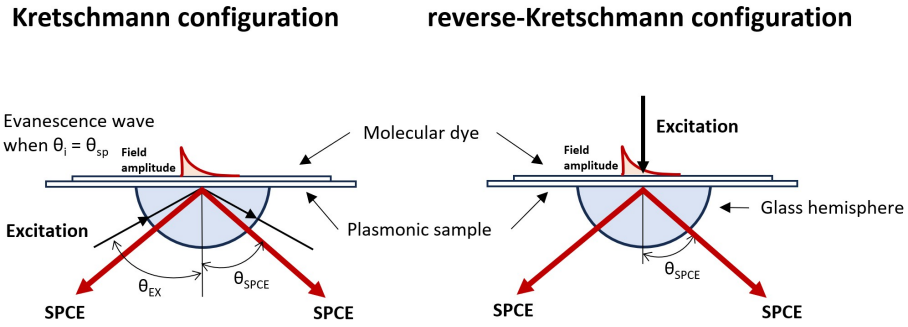

1.4 Fig. Surface plasmon coupled emission under Kretschmann and reverse-Kretschmann configurations.

SPCE phenomenon is closely related to SPR, however, the main difference is in the participating field modes. While SPR emerges due to the coupling of excitation light with the evanescent field of SP, in the SPCE case, the coupling is between excited fluorophores and SP. The phenomenon of surface plasmon resonance can also be utilized for fluorescence detection. When incident light excites surface plasmons at a metal–dielectric interface, an excited fluorophore located near the surface can couple its emission into the plasmon mode. This process produces a directional surface-plasmon–coupled emission confined to a narrow angular cone defined by the emission angle (θ_{SPCE}), as illustrated in Fig. 1.4.

The emission angle differs from the excitation SPR angle (θ_{EX}) because plasmon resonance is wavelength-dependent. For example, a fluorophore excited at 633 nm and emitting at 700 nm due to the Stokes shift would exhibit a reflectivity minimum at $\theta_{EX} = 43.6°$ for the excitation wavelength, shifting slightly to $\theta_{SPCE} = 43°$ at the emission wavelength. Although this angular difference appears small, it is significant compared with the sub–0.1° sensitivity typical of conventional SPR measurements. Consequently, fluorophores emitting at different wavelengths couple to distinct plasmonic angles determined by their emission spectra and the optical properties of the multilayer system.

SPCE follows the same coupling mechanism as SPR, fluorophores located within the evanescent field region (up to 500 nm from the metal surface [8, 48, 49]) will emit into the prism at well-defined plasmonic angles specific to their emission wavelengths. Experimental observations [32, 48] confirm that θ_{EX} is largely independent of the fluorophore's precise distance from the metal surface, except for small variations introduced by the thickness and refractive index of the overlying dielectric layers.

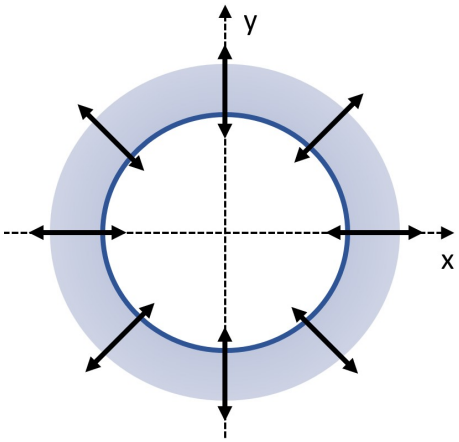

1.5 Fig. Intensity profile and polarization of the radially symmetrical emission cone of p-polarized surface plasmon coupled emission observed at the BFP of microscope objective [49].

Intensity distribution in BFP exhibits rotational symmetry with a ring whose radius corresponds to the emission angle of the plasmon mode (Fig. 1.5). Light emitted from surface plasmon coupled mode exhibits polarization directions parallel to the plane of incidence of the optical interface (p-polarization). However, this corresponds to a radial polarization profile when observing at the BFP of the objective. The intensity profile observed at the BFP corresponds to the square of the electric field $\hat{\mathbf{E}}(k_{\parallel})$ at the interface [33]:

$$\hat{\mathbf{E}}(k_{\parallel}) = \frac{ip_z}{8\pi^2\varepsilon_0}\frac{k_{\parallel}\, t^{(p)}(k_{\parallel})}{\sqrt{1-k_{\parallel}^2/k_0^2}}\exp[ik_0 z_0\sqrt{1-k_{\parallel}^2/k_0^2}]\mathbf{n}_{\rho}, \tag{1.10}$$

plasmon oscillations can be represented as oscillating vertical dipoles p_z, $k_{\parallel}$ is the in-plane momentum distribution, z_0 is the distance measured from the surface to the dipole, $\mathbf{n}_{\rho}$ is the unit vector pointed along the radial direction along the metal/dielectric interface.

1.4. **Strong light–matter coupling**

1.4.1. Classical description

The working principles of the strong coupling regime can be discussed in terms the simple classical coupled oscillator model or the quantum mechanical version of the phenomena. A simple picture, describing the interaction of SPPs and emitters, can be considered when placing emitters in the vicinity of the

plasmonic cavity. The interaction between the cavity and emitter leads to fast energy transfer between the cavity mode and emitter. Classical analogy can be thought of as two coupled oscillators, where energy is transferred back and forth between the oscillators via the coupler (Fig. 1.6).

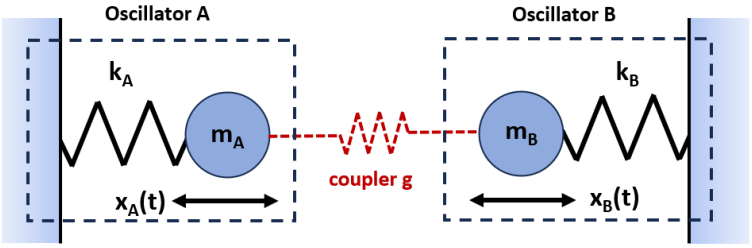

1.6 Fig. Classical strong coupling regime illustrated as two coupled harmonic oscillators. Oscillators with mass m_i and spring constant k_i are coupled using the additional spring with coupling energy g, which leads to a shift of the original eigenfrequencies.

In strong coupling, it is impossible to distinguish between different excitation modes, and the two interacting modes must be viewed as one, i.e., the energy becomes delocalised over the two modes. Newtonian equations of motion with two coupled oscillators with masses m_i, spring constants k_i, and coupling strength g can be denoted as [8]:

$$\begin{cases} m_A\ddot{x}_A + k_A x_A + g(x_A - x_B) = 0, \\ m_B\ddot{x}_B + k_B x_B - g(x_A - x_B) = 0. \end{cases} \tag{1.11}$$

Non-trivial solutions to the differential equations can be found only when $det[M] = 0$, where M describes two coupled linear solutions for x_A^0 and x_B^0 written in matrix form. New eigenfrequencies emerge as new normal modes of the systems [8]:

$$\omega_{\pm}^2 = \frac{1}{2}\left[\omega_A^2 + \omega_B^2 \pm \sqrt{(\omega_A^2 - \omega_B^2)^2 + 4\Omega_R^2\omega_A\omega_B}\right], \tag{1.12}$$

polaritonic states emerge, usually distinguished as Upper Polariton (UP) with eigenfrequency ω_+ and Lower Polariton (LP) with eigenfrequency ω_- (Fig. 1.7). The energy difference between ω_+ and ω_- at the resonance (k_0) is the normal-mode splitting Ω_R. Many systems in nanophotonics and quantum optics can be explained using the coupled oscillator model. For example, coupling between quantum dots [50], coupling between photons and phonons in cavities [51], and atoms in external fields [52].

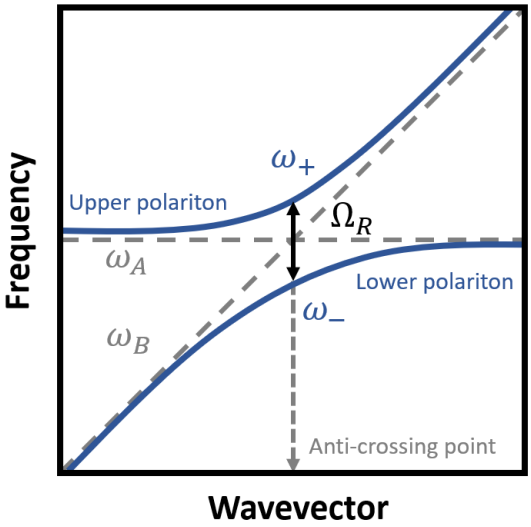

1.7 Fig. Eigenfrequencies in case of uncoupled oscillators (gray dashed lines). Splitting of the eigenfrequencies appears in the strongly coupled case (blue lines).

Invoking a full electrodynamical description where the emitter is described as a Lorentzian oscillator and driven by an electromagnetic wave of SPP, the normal mode splitting can be described as [27]:

$$\Omega_R = \sqrt{\frac{N}{V}} \frac{e}{\sqrt{\varepsilon_0 m}}, \tag{1.13}$$

where e and m are the charge and mass of the electron, respectively, and ε_0 is the dielectric constant. Splitting is proportional to the density of the emitters and is a important result for sensing applications [27]. Moreover, the smaller mode volume of the SPP benefits strong coupling, since the electric field is confined far below the diffraction limit, as compared with other cavity modes. These states can be associated with dressed states in a quantum mechanical description.

Experimental investigations of strong coupling are usually performed by optical measurements, such as reflection, scattering, transmission, extinction, and photoluminescence [7, 17, 53–55], where it is observed that upon strong coupling spectral response is modified. It must be noted that when considering quantum mechanical treatment of the problem, normal mode splitting is also called Rabi splitting. Constant absorption and re-emission processes of the emitter correspond to a decrease in the group velocity $d\omega/dk$ of SPPs, causing bending of the dispersion curve.

An important boundary condition arises in order to achieve the strong coupling regime [27]:

$$g > \tfrac{1}{4} \left(\gamma_{SPP} + \gamma_{ex} \right), \tag{1.14}$$

where γ_{SPP} and γ_{ex} are plasmonic and exciton losses in the system, respectively, and g is the coupling strength. These losses correspond to the uncoupled linewidths and can be influenced by other mechanisms such as non-radiative dephasing, scattering, and inhomogeneous broadening [56]. Whether the system is in a weak or strong coupling regime depends on whether the linewidths of the individual systems are lower or higher than g. An important property of the strong coupling regime is the collective nature of participating particles. Typically, noncoherent excitonic states can inherit coherent behavior from SPPs, when in strong coupling. As demonstrated by Guebrou et al. [57], coherent emission can be detected even from spatially remote emitters. Coherent energy transfer back and forth is another important characteristic of strong coupling, however, direct observation of Rabi oscillations in time is extremely complex [58], and most of the studies report about spectral response, which is more easily obtained. For example, typical plasmonic Rabi splitting of about 100 meV corresponds to a Rabi oscillation period of about tens of femtoseconds. Since the polaritonic states are part light and part matter, the typical effective mass of a polariton is around $10^{-4} - 10^{-5}$ times the electron mass, allowing to achieve large de Broglie wavelength. This property allows to achieve Bose-Einstein condensation [54, 59] and superfluidity [60]. Dispersive characteristics have become the primary feature of polaritonic quasiparticles, and strong light-matter interaction has become the technique, which allows tuning physical, optical, and chemical properties of the emitter and plasmonic mode [61, 62]. Typical material excitations, exhibiting non-dispersive behaviour, become highly dispersive at the anti-crossing point, allowing to observe modified chemical dynamics among other things [22, 53, 63].

Various optical configurations have been used for the investigation of the strong coupling regime between a emitters and optical resonance modes. Advanced manufacturing methods allowed to achieve high coupling values using localised surface plasmons [64, 65], single plasmonic particles [66], NPoM [16], surface lattice resonances [67]. QE has also been strongly coupled with a wide range of dielectric microcavities as well [68–70]. Coupling can also be achieved between two resonant modes, rather than using QE and a single resonance mode [71, 72]. Dielectric microcavities typically exhibit much higher Q factors ($10^3 - 10^4$), however also have larger modal volumes V which are limited by the diffraction $(\lambda/2)^3$ leading to decreased electric field amplitude. Small plasmonic mode volumes permit strong coupling even with single quantum dots [17, 73, 74]. One of the advantages of using plasmonic structures when compared with dielectrics is that plasmonic cavities exhibit room-temperature strong coupling, whereas dielectric cavities often require ultracold temperatures. Moreover, open cavity architecture, provided by plasmonic resonances, is much more favourable for real-world applications.

1.4.2. Quantum description

In the quantum description of strong light–matter coupling, the electromagnetic field and the material excitation are both treated as quantized systems that exchange energy coherently. When the interaction strength between a photon mode (such as a cavity or plasmonic resonance) and an exciton exceeds their respective loss rates, the two systems can no longer be described independently. Excitation splits into two separate polaritonic eigenstates (Fig. 1.8).

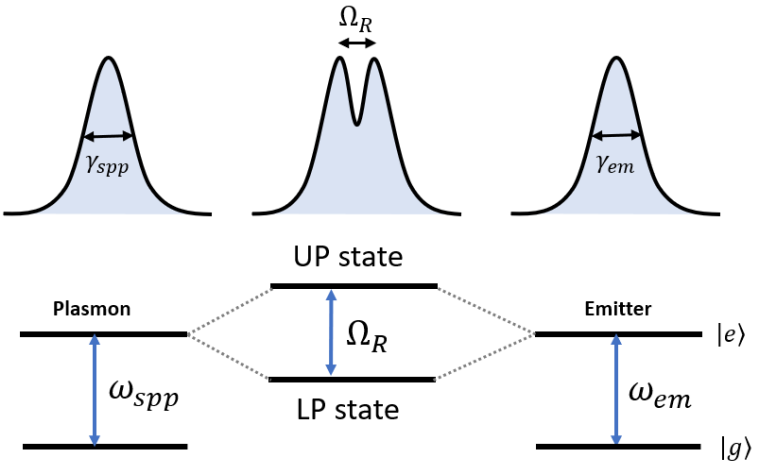

1.8 Fig. Energy exchange between two coupled eigenmodes described by damping rate γ_{spp} and γ_{em}. Plasmon and emitter modes become delocalized when in strong coupling. Polaritonic eigenstates emerge as new eigenfrequencies of the coupled modes with Rabi splitting Ω_R equal to the energy difference between UP and LP states.

Highly dispersive characteristics of polaritonic states are evident when considering the quantum description of the phenomena. Typical quantum description of strong coupling starts with a discussion for the single emitter case interacting with a quantized field, the so-called Jaynes-Cummings Hamiltonian, which is equivalent to [27]:

$$H = \frac{1}{2}\,\hbar\omega_{ex}\sigma_z + \hbar\omega_{pl}\hat{a}^\dagger\hat{a} + \hbar\left(g\,\hat{a}\sigma_+ + \text{h.c.}\right), \tag{1.15}$$

here g describes the coupling strength and is proportional to the dipole moment of the emitter, $\hat{a}^\dagger$ and $\hat{a}$ correspond to creation and annihilation operators, and ω_{ex} and ω_{pl} are the respective transition eigenfrequencies of exciton and plasmonic modes. Hamiltonian couples the state $|e,n\rangle$ to $|g,n+1\rangle$, where $|e,n\rangle$ describes a state with an excited emitter and n photons, and $|g,n+1\rangle$ is a state with the emitter in the ground state and n+1 photons in the system. The coupling term in the Hamiltonian therefore describes transitions between the atom's excited and ground states, while emitting/absorbing a photon in

the process. After diagonalization, one obtains the following eigenvalues [27]:

$$E_{\pm} = \hbar\left(n + \frac{1}{2}\right)\omega \pm \frac{1}{2}\hbar\sqrt{\delta^2 + 4g^2(n+1)}, \tag{1.16}$$

with generalized Rabi frequency described as [27]:

$$\Omega_R = \sqrt{\delta^2 + 4g^2(n+1)}. \tag{1.17}$$

Under strong coupling, new eigenstates are [27]:

$$|\psi_-\rangle = -\sin\theta_n\,|e,n\rangle + \cos\theta_n\,|g,n+1\rangle\,, \tag{1.18}$$

$$|\psi_+\rangle = \cos\theta_n\,|e,n\rangle + \sin\theta_n\,|g,n+1\rangle\,. \tag{1.19}$$

The polaritonic states $|\psi\pm\rangle$ emerge as new eigenstates of the system, which are described as a superposition of material excitation and optical transition of the system, thus inheriting properties from both. Coefficients $sin(\theta_n)$ and $cos(\theta_n)$ are Hopfield coefficients. They allow to quantify light-matter hybridization. At resonance ($\theta_n = 45°$), the mixing ratio is 50/50, meaning that the polariton is exactly half-photon and half-exciton quasiparticle, whereas at $\theta_n = 0$ polariton is purely photonic. This shows that polaritonic states are highly dispersive, exhibiting light-like and matter-like behaviour depending on the detuning parameter θ_n. Due to the influence of photonic mode, polaritonic states at $k_{||} \sim 0$ exhibit effective mass which is much lower compared to bare exciton mass ($m_{pl} \sim 10^{-4} m_{ex}$), thus allowing to achieve Bose-Einstein condensates (BEC) at very high critical temperatures [54,59]. Lasing from polaritonic condensates has been observed [75]. Polaritonic lasers are known to operate with significantly lower threshold values as compared to the standard photonic lasers [76], with some reports indicating the expected threshold-less lasing in the strong coupling regime [77]. In a standard laser, coherence is achieved by stimulated emission, while in a polaritonic laser, the underlying physical mechanism is totally different. Here, coherence is attained from the formation of BEC, and electron population inversion is not required [78]. For multiparticle systems, relevant for SPP strong coupling experiments, the Hamiltonian can be described by the Dicke model, which predicts phenomena such as superradiance [79], coherent phase transitions [59]. Superfluidity is another property observed in polaritonic condensates [60]. This property is closely related to the formation of BEC. Superfluidity allows to achieve a dissipation-less flow of mass whenever many-particle quantum coherence in BEC is achieved [78].

Using Hopfield coefficients, polaritonic states can be described as a coherent mixture of light and matter particles, with varying degrees of weight [80]. Moreover, polariton fluorescence lifetime should also exhibit dispersive behavior, since it follows from Hopfield theory. However, observations of dispersive po-

lariton lifetime behaviour have been complicated due to internal interactions with the exciton reservoir state, which result in the polariton bottleneck effect, whenever non-resonant excitation is applied [81, 82]. An exciton reservoir is a population of excitons that are created by optical pumping but do not directly participate in coherent strong coupling regime [83]. These excitons are typically high in energy or momentum and therefore couple only weakly to the cavity photon mode. Instead of forming polaritons immediately, they act as an incoherent particle bath that can scatter into lower-energy polariton states [84]. The reservoir often has a longer lifetime than polaritons and can strongly influence system dynamics by feeding polaritons [85], inducing energy shifts [86], and contributing to nonlinear effects [87].

This is where the increase in the lifetime of the polaritonic state can be obtained if the polariton bottleneck effect is present. New polaritonic eigenstates with modified dispersion relations can be excited by several different mechanisms, due to the different nature of particles participating - light and matter quasiparticles. Resonant excitation is applied whenever the excitation conditions match the polaritonic dispersion line, usually UP, and on the other hand, we can also excite the polaritons non-resonantly. This excitation happens whenever excitation light does not meet the conditions for resonant polaritonic excitation, rather, the material is excited, which in turn decays to LP excitation. Investigation of losses in polaritonic systems are crucial for understanding the decay mechanisms that govern the systems.

1.5. **Fluorescence in coupled systems**

A lot of current research in plasmonic strong coupling focuses on coherence properties of the emitted light [57,88,89] or modified chemical dynamics [22,63], however important property arises from a splitting in the frequency domain which corresponds to modified dynamics in the time domain [58]. Typical excited state dynamics of a molecule or atom consist of spontaneous emission, which describes the transition from the excited state to a lower energy state and emits a photon in the process. Spontaneous emission is also called fluorescence, whenever a molecule or atom is excited by the absorption of light. Light interaction with molecules typically involves *excitonic states*. These states are described as bound states of an electron and a hole, which are attracted to each other by the electrostatic Coulomb force.

An exciton is a neutral quasiparticle regarded as an elementary excitation in condensed matter physics. Molecular excitons in fluorescence dye can be regarded as excited states of molecules. After a molecule in the ground state absorbs a photon with energy equal to or greater than the higher excited states

(S_1, S_2,...S_n), an electron is excited to a higher level. Electronic transition to the ground state is permitted via different energy transfer mechanisms typical in molecular systems [90]: due to vibrational relaxation, electrons can relax from the upper vibrational level of the excited state to the lowest vibrational level of the same excited state non-radiatively (Fig. 1.9). This process is known as *internal conversion*. Radiative or non-radiative electronic transitions to the ground state follow shortly after. Radiative process by which the molecules transitions to the ground state after emission of a photon is called fluorescence. This process typically takes around 10^{-9} ns for organic dye. Energy associated with the fluorescent photon is lower compared to the energy required for excitation, thus emission is typically observed at longer wavelengths. This shift in energy (wavelength) is due to internal conversion processes and is known as the Stokes shift (Fig. 1.10).

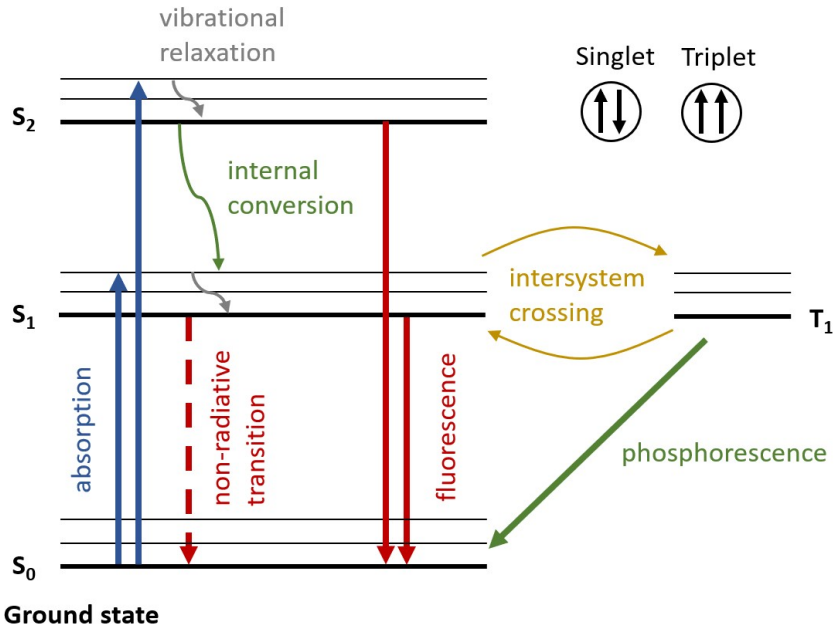

1.9 Fig. Jablonski diagram depicting various energy transfer mechanisms between excited singlet states S_1, S_2, excited triplet state T_1, and ground state S_0.

Another emission process, which occurs when electron energy is transferred to triplet states (T_1, T_2,...T_n), is known as phosphorescence, and the energy transfer between S_i and T_i states is referred to as intersystem crossing. As opposed to singlet states, electrons in triplet states have parallel spins. These transitions are "spin-forbidden", exhibiting decreased transition rates, and the emission of phosphorescence photons to the ground states typically occurs from milliseconds to several minutes.

Resonant excitation occurs when the excitation light energy matches the energy of an optical transition or cavity mode, leading to efficient and selective population of that specific state. Under resonant conditions, light couples directly to the desired electronic or polaritonic level, often resulting in coherent excitation and minimal excess heating. In contrast, non-resonant excitation uses photons with higher energy than the resonance. The system is first excited into higher-lying electronic or vibronic states, and relaxation processes (such as phonon scattering or internal conversion) bring the excitation down to the resonant level before emission occurs. Non-resonant excitation is less selective but can populate multiple modes simultaneously, making it common in photoluminescence and fluorescence studies where broad excitation is desired.

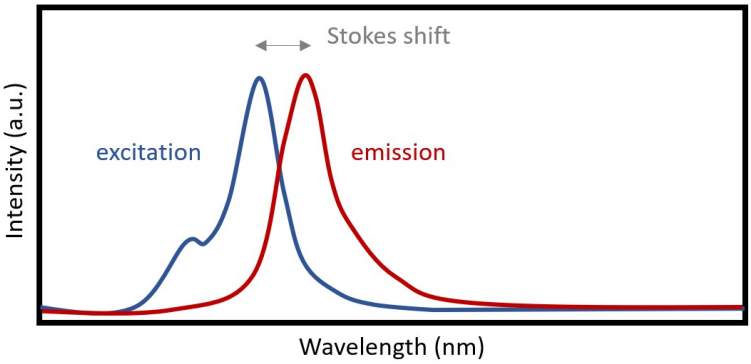

1.10 Fig. Absorption and emission spectra of R6G molecular dye. Emission occurs at a lower energy when compared to excitation due to internal conversions. This shifts the emission spectrum to longer wavelengths. Stoke shift for R6G molecule is around 25 nm.

Fluorescent photons exhibit random phase and emission direction, in contrast to stimulated emission observed in lasers. Fluorescence in the time domain can be described using decay models. If the number of excited states at time t is given by $P(t)$ then decay of P is given by [91]:

$$\frac{\partial P(t)}{\partial t} = -\Gamma_{rad} P(t), \tag{1.20}$$

where Γ_{rad} is the radiative decay rate. Γ_{rad} is dependent on the particular transition process within the molecule. The solution to the differential equation gives [91]:

$$P(t) = P(0)e^{-\Gamma_{rad} t}. \tag{1.21}$$

Excited states decay exponentially with a particular lifetime given by $\tau_{rad} = 1/\Gamma_{rad}$. The model assumes that excited states decay radiatively with 100% quantum efficiency, however, in order to determine the total decay rate, nonradiative transitions, which often arise due to coupling to phonons, must be taken into account. In case of several different decay channels, such as non-radiative

transitions, exciton-exciton interactions, etc., the net lifetime is inversely proportional to the sum of different transition rates:

$$\tau_{rad} = \frac{1}{\Gamma_{rad} + \Gamma_{nrad} + \Gamma_{ex} + \cdots}. \tag{1.22}$$

Even though the rate-equation model predicts the exponential decay, the process is fundamentally quantum mechanical and cannot be explained by classical electromagnetic theory [91]. In order to correctly describe fluorescence rates Γ_i, one typically uses a quantum mechanical description based on Fermi's golden rule [92]:

$$\Gamma_{\mathrm{rad}}(r) = \tfrac{\pi\omega}{3\hbar\varepsilon_0}|\mathbf{p}|^2\rho(r,\omega), \tag{1.23}$$

where ω is the emission frequency, r is the position, p is the dipole momentum of the emitter, ε_0 is the permittivity of free space, and $\rho(r,\omega)$ is the density of states. It was not until the pioneering work of Purcell, who recognized that the lifetime of the excited state depends also on its environment [15]. Experiments have already shown that the spontaneous emission rate is modified whenever coupling between plasmon and emitter is achieved [14, 92, 93]. More specifically, changes in local density of states (LDOS) due to the presence of a nanophotonic environment result in enhancement or suppression of emission rates, corresponding to changes in the lifetime of fluorescence sources [92–95]. This regime is strongly affected by the quality factor and mode volume of the cavity and is described by the Purcell factor:

$$F_p(\omega) = \frac{6\pi c^3 Q}{\omega^3 V_m} \sim \frac{\Gamma}{\Gamma_0}, \tag{1.24}$$

here, Q is the quality factor of the photonic mode, c is the speed of light, ω is the electric dipole frequency, and V_m is the mode volume of the cavity, Γ and Γ_0 are the total decay rates in the presence and absence of the optical cavity, respectively. Even though light-matter coupling remains in the weak coupling regime, large Purcell enhancement has been of particular interest for enhancing the radiative emission rate of single photon sources.

Even more radical changes to the dynamics of excited states occur upon strong light-matter interaction (**Fig.** 1.11). The internal mechanism governing polariton formation is characterized as rapid energy exchange between material and light excitations. This is equivalent to fast emission and absorption processes, which occur on a femtosecond timescale for plasmonic excitations [23, 58]. Without damping, the probability of finding an exciton (P_{ex}) in the excited states is transformed from an initially exponential function (Eq. 1.21) to [13]:

$$P_{ex}(t) = \cos^2\left(\Omega_R\, t/2\right), \tag{1.25}$$

where Ω_R is the Rabi frequency. Rabi oscillation frequency is dependent on

several factors, such as dipole moment, concentration of participating particles. To be more exact, a higher number of particles participating, with specified volume, results in a collective dipole moment described by the formula (Eq. 1.13). In order to observe such dynamics, one should have a timing resolution of the order of 10s of femtoseconds for plasmonic excitation.

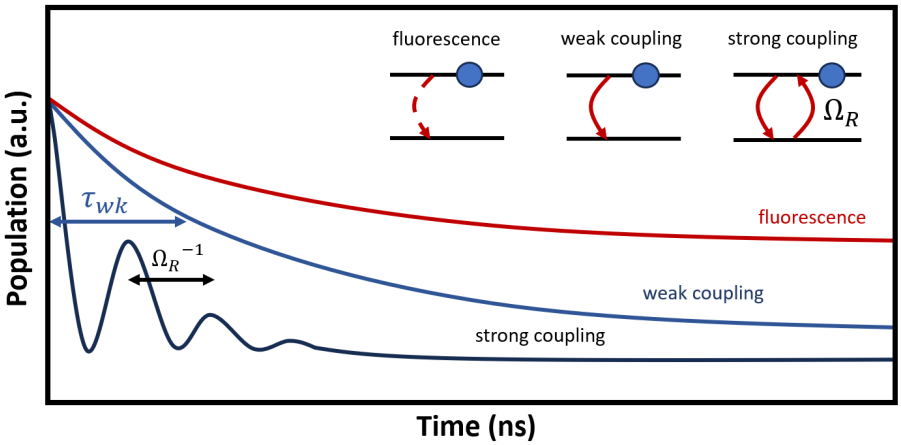

1.11 Fig. Excited state population decay: Regular fluorescence exhibits exponentially decaying profile with a particular lifetime τ_{rad}. In case of weak coupling, modification in the photonic density of states results in enhanced emission with lifetime τ_{wk}. In the strong coupling regime, repopulation of the excited state is governed by Rabi oscillations with frequency Ω_R, with damping responsible for the amplitude.

Fluorescence lifetime can be measured using several experimental techniques that differ in temporal resolution and detection scheme. The most common approach is time-correlated single-photon counting (TCSPC), where the arrival times of individual photons are recorded relative to a pulsed excitation source to reconstruct the decay curve with picosecond precision [96]. Alternatively, streak camera systems directly image time-resolved fluorescence by converting photon arrival times into spatial coordinates, allowing sub-picosecond temporal resolution [97]. In the frequency domain, phase-modulation or frequency-resolved lifetime measurements are used to determine the lifetime from the phase shift and modulation depth of the emitted signal relative to the excitation [98]. More recently, fluorescence lifetime imaging microscopy (FLIM) techniques have enabled mapping of spatially varying lifetimes across a sample, providing both temporal and spatial information in biological and nanophotonic systems [99]. Recently, new approaches for measuring fluorescence lifetime on the picosecond timescale have been suggested that utilize the quantum two photon interference effect [100]. Investigation about population dynamics and observation of Rabi oscillations in strongly coupled plasmonic devices has been permitted using the fs pump-probe technique [58].

Attempts to experimentally investigate emission from fluorescent molecular dyes are often hindered by photobleaching. Photobleaching refers to the irreversible loss of fluorescence that occurs when fluorophores undergo permanent photochemical degradation during repeated excitation–emission cycles. Each excitation event promotes the molecule to an excited electronic state, from which nonradiative transitions or intersystem crossing to a triplet state may occur. In this long-lived triplet state, the molecule is highly reactive and can interact with molecular oxygen or nearby species, leading to bond breakage or oxidation that destroys its ability to fluoresce. The process depends strongly on excitation intensity, wavelength, local chemical environment, and the availability of oxygen. Photobleaching limits the achievable observation time and signal-to-noise ratio in fluorescence imaging and spectroscopy. To mitigate bleaching effects, experimental conditions are often optimized by reducing excitation power, using pulsed excitation, introducing oxygen scavengers or antifade reagents, and selecting more photostable fluorophores. Understanding and minimizing photobleaching is particularly important in time-resolved and single-molecule measurements, where stable emission is essential for reliable lifetime or intensity analysis. Attempts to minimize the photobleaching reactions within fluorescent molecules have been performed by using strong coupling regime [53, 63].

2. EXPERIMENTAL PROCEDURE

Investigating dynamical processes in strongly coupled light-matter systems requires precise sample fabrication and time-resolved detection. In plasmonic strong coupling, the optical response is highly sensitive to metal film thickness (typically a few tens of nanometers), demanding nanometer scale control and smooth surfaces to minimize scattering losses.

Probing dynamics such as modified radiative rates further requires time-resolved techniques capable of single-photon detection with sub-nanosecond resolution. Experimental design must ensure spectral overlap between molecular excitons and plasmonic modes, while taking into account the angular and polarization dependencies of the hybrid states.

Combining thin-film deposition with ellipsometry techniques, back focal plane (BFP) imaging, and time-correlated single-photon counting (TCSPC) enables direct access to fluorescence lifetimes and angular emission properties that characterize the strong coupling regime.

2.1. **Time-correlated single photon counting**

2.1.1. Fluorescence lifetime measurement

Investigation of time-dependent emission of various emitter species allows us to gain an understanding of dynamical processes within the system. This is especially useful when considering very fast transitions of the order of 100s of picoseconds. TCSPC is based on the precisely timed registration of single fluorescent photons, where the excitation pulse is used as a reference. Upon excitation of emitter species, such as quantum dots and organic dye molecules, spontaneous emission follows shortly after. As already mentioned in Chapter 1.5, excited molecules have a corresponding lifetime τ_{rad} which describes the average amount of time a molecule spends in the excited state. Detection of a single photon event does not provide full information about the time-dependent fluorescence intensity profile of the emitter. TCSPC is thus used to retrieve the full picture describing dynamical processes and can reach sub-ns timescales only limited by the system's instrument response function (IRF). This technique consists of exciting the sample with ultrashort laser pulses, which in turn spontaneously emit photons after each excitation event (Fig. 2.1). Emitted photons are spectrally filtered, collected, and sent to a detector, which transforms photons into electronic pulses. For every optical pulse emitted from

the ultrafast laser, an electronic pulse is sent to timing electronics (TCSPC) to act as a reference pulse. Ultimately, observation of light sources, with intensities down to the single photon level, can only be achieved using single photon detectors. Photons, which are spontaneously emitted by the molecules after transition to the ground state, can be detected using detectors such as a single photon avalanche diode (SPAD) or a photomultiplier tube (PMT). The SPAD detector used during the experiments is a semiconductor device, working as an avalanche photodiode operating in Geiger mode (biased above its breakdown voltage). A photon is capable of triggering around 10^8 carriers, allowing the observation of single photon events.

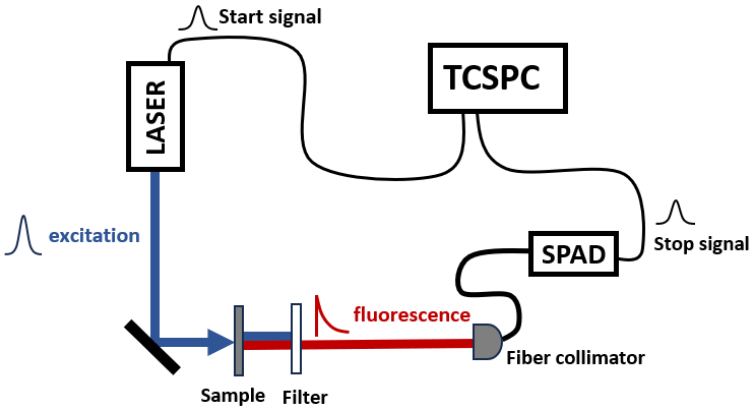

2.1 Fig. Typical experimental layout for fluorescence lifetime measurement using the TCSPC technique.

Experiments were performed using IDQ ID100-MMF50 fiber-coupled SPAD detector with an active area of 50 µm with fluorescence light detected in the 600 - 700 nm range. Spectral response of the detectors in this range is 18% to 28%, indicating that only around one-fifth of the photons, which reach the active area, are detected. Timing resolution of the SPAD is ∼40 ps at FWHM. An output pulse with an amplitude of 2V and a width of 10 ns was sent to a 10 dB attenuator before reaching TCSPC. Dark count rate, which is caused not due to absorption of photons but originates because of thermally generated carriers within the device, was kept at <100 cps (counts per second) during the experiment.

Techniques such as START-STOP or reverse START-STOP in more modern systems are used to precisely time the arrival times of detected photons (Fig. 2.2). In the START-STOP configuration laser pulse acts as a START signal to start the timer, while the detected photon acts as a STOP signal. The time difference between START and STOP is calculated for a single emission event at the TCSPC unit. In a reverse START-STOP configuration detected photon acts as START, while the STOP is the following excitation pulse. This

prevents unnecessary ON-OFF cycles of the detector electronics when using a high-repetition rate laser (>1MHz), as the emission rates in typical experiments have to be below 10% of the laser repetition rate to reliably sample the decay statistics. This pulse starts the internal timing counter of the TCSPC unit. Precise timing of the arrival of the photon can be measured whenever the STOP pulse is registered at the TCSPC unit.

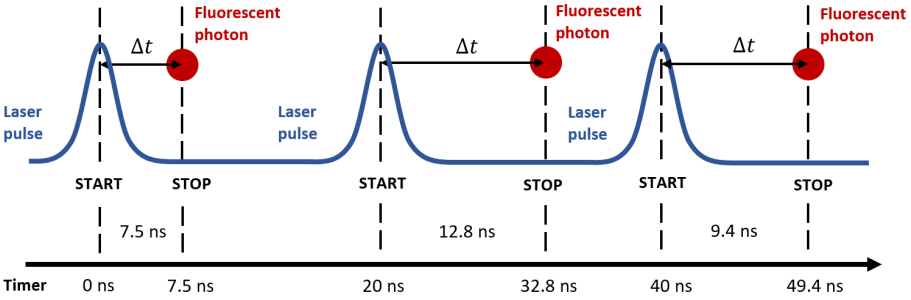

2.2 Fig. Fluorescence lifetime measurement using START-STOP TCSPC: photon arrival time is measured as a time difference between the excitation pulse (50 MHz) and the detected photon.

Time-correlated single photon counting was performed using PicoQuant MultiHarp 150N, with a minimal time bin width of 80 ps. Dead-time of the detector and timing electronics describes the period after a photon is detected during which the device cannot detect any new photons. In SPAD, this occurs because SPAD must be reset after an avalanche event to become operational again. SPAD detector dead time is around ∼45 ns. Dead time of TCSPC is <650 ps, indicating that the total dead time of the system is dominated by the SPAD detector. Triggering was set at the falling edge (0.4 V). Experiments were performed with an excitation rate of 1 MHz or 50 MHz. In both cases fluorescence rate was kept low at <5 % of the excitation frequency to avoid pulse pile-up. Pulse pile-up occurs when the rate of fluorescence pulses is very high, and two or more photons arriving at the detector skew the results toward shorter lifetime values (Fig. 2.3).

Detections of time-tagged fluorescence photons allow to build a histogram of the time difference between excitation and emission events in the sample. The full temporal intensity profile of the emission process is thus obtained and can be described using multi-exponential function.

The average length of time a molecule spends in the excited state is dependent on the type of molecule and its local environment. When a sample under study contains a mixture of different molecules or the molecule undergoes interactions within the sample, the decay is generally more complex and is typically described by a multi-exponential function with A_i corresponding to the relative concentration of molecules (Fig. 2.4). Decrease in the intensity

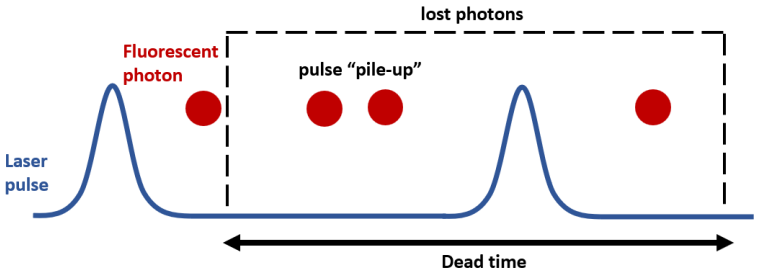

2.3 Fig. Pulse pile-up and detector deadtime effects when measuring fluorescent lifetime.

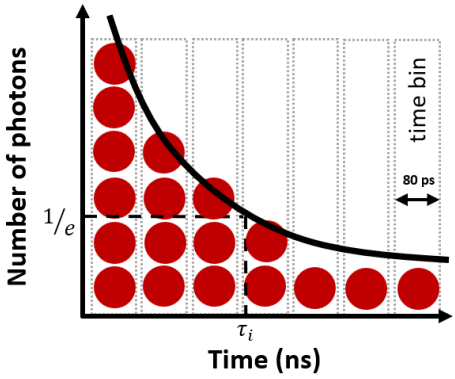

2.4 Fig. Detected photons are divided into separate time bins according to the time difference between START and STOP. Spontaneous decay of the excited state is the histogram of the measured photon number vs time. Experiments were performed with time bin of 80 *ps*.

$I(t)$ of the emitted light is thus:

$$I(t) = \sum_{i}^{n} A_i e^{-t/\tau_i}, \tag{2.1}$$

where τ_i corresponds to the fluorescence lifetime of the species. Moreover, τ_i is independent on the concentration of particular species. This technique allows to investigate effects such as Förster resonant energy transfer (FRET), non-radiative processes or quenching via molecular collisions [101].

2.1.2. Estimation of fluorescence lifetime

Precise timing of the arrival of the photons is performed by the TCSPC unit, which divides the measurement timing interval into separate time bins, with resolution defined by the detector and TCSPC electronics. Experiments

were performed with a time bin size equal to 80 ps, meaning that TCSPC can distinguish between two photons whenever the time difference between the two is not smaller than 80 ps. Other factors, such as excitation pulse width, detector, and electronic jitter set limit for minimal measurable lifetime, and are described by Instrument Response Function (IRF). Contribution of these

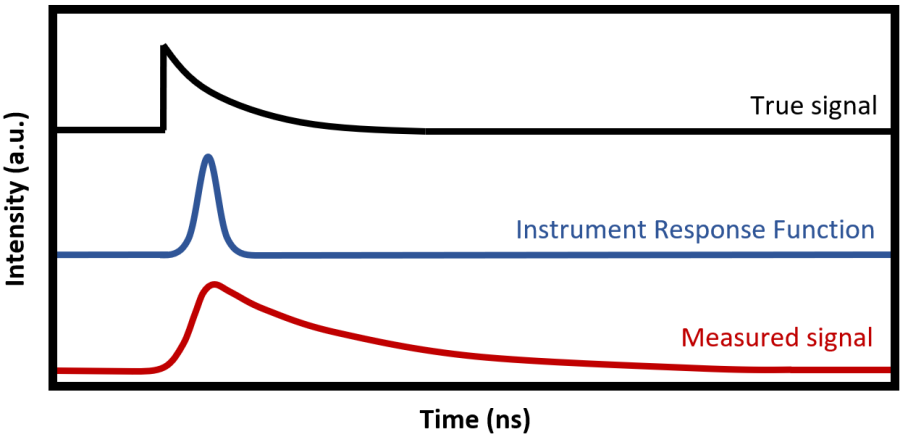

2.5 Fig. Excited state decay is modified by system's IRF. Measured signal is obtained in TCSPC, which is a convolution between true signal and IRF.

inputs to the IRF can be identified as:

$$FWHM_{\text{system}}^{\text{IRF}} = \sqrt{\sum FWHM_{\text{component}}^2}, \tag{2.2}$$

IRF describes how the instrument responds to instantaneous, short-duration events. Excited state decay is blurred by the system IRF. Upon measuring the signal, it is necessary to remove the system's distortion from the recorded data. Mathematically, the signal obtained upon measuring the sample corresponds to a convolution between the IRF and the true exponential decay function of the excited state. Thus, mathematical corrections to the measured signal are crucial in order to obtain true excited state decay. Convolution between functions $f_{true}(t)$ and $IRF(t)$ is identified as:

$$f_{measured}(t) = f_{true}(t) * IRF(t) = \int_{-\infty}^{\infty} f_{true}(\tau)\, IRF(t-\tau)\, d\tau. \tag{2.3}$$

Obtaining $f_{true}(t)$ from the convolution integral remains challenging because the expression cannot be inverted analytically. There is no closed-form solution for $f_{true}(t)$ given $f_{measured}(t)$ and $IRF(t)$. An additional complication arises from measurement noise: $f_{measured}(t)$ contains statistical photon noise thus, it cannot be considered perfectly accurate. As a result, direct calculation of $f_{true}(t)$ from the recorded data is impractical. The standard approach to this

deconvolution problem is to employ a fitting procedure [47, 102, 103]. The biexponential function (Eq. 2.1) for the fluorescence decay is defined, convolved with the instrument response function, and the resulting curve is compared with the measured data. The parameters of the biexponential function are then iteratively adjusted until the best agreement with the experimental decay is achieved. Comparison to the experimentally observed data was performed using the least square fitting method defined as:

$$S(p) = \sum_i r_i^2 = \sum_i [y_i - f(x_i, p)]^2. \tag{2.4}$$

Least squares fitting method was used to find the set of parameters (A_i and τ_i) in a biexponential model that best describes a set of experimental data by minimizing the sum of squared differences between the data and the model. Goodness of fit was evaluated using the R^2 coefficient. Modelling was performed in a Python environment. Other methods to evaluate fluorescence lifetime include 'tail-fitting', which might be sufficient when the IRF « decay. Alternatively, a technique that does not rely on deconvolution is called phasor analysis [90], but it is beyond the scope of this work.

2.2. **Back focal plane imaging**

Optical microscopy has experienced enormous growth in the last decades. The emergence of new optical imaging techniques accelerated the use for research and commercial applications. Early use of microscopy techniques was hindered by optical aberrations, blurred images, and poor lens designs [104]. However, the use of microscopy tools allowed the observation of spatial features down to sub-micron resolution and was only limited by the diffraction of light. That was until super-resolution imaging techniques such as stimulated emission depletion (STED) and photo-activated localization microscopy (PALM) showed that the diffraction limit can be overcome, enabling resolution down to the near-atomic level [105–107]. Other techniques based on dark field [108], phase contrast [109], were invented to improve the detection of transparent samples. Lateral resolution and optical sectioning in microscopy were increased using various techniques such as confocal microscopy [110,111], light-sheet microscopy [112], and non-linear microscopy [113,114]. Therefore, various microscopy techniques are employed to investigate spatial features.

Investigation of nano-photonic devices using microscopy techniques requires a somewhat different approach. More specifically, nano-photonic devices exhibit angular characteristics, which are not directly observable using real plane microscopy setups. A method to obtain k-space information from the

samples by measuring the full electric field (both amplitude and phase) in the near field and taking the Fourier transform [115]. However, phase measurements of the electric field can become challenging. An all-optical method, such as back focal plane (BFP) microscopy, allows access to angular information by exploiting the Fourier transform properties of a lens (Fig. 2.6). In particular, when an object, such as a molecule, is at the focus of a lens, a corresponding Fourier transformed image is formed at the back-focal plane, directly giving (k-space) information. Therefore, BFP microscopy has emerged as an important tool in nano-photonics. This technique allows to gain information that is not directly accessible using conventional real plane imaging techniques [116]. In particular, BFP microscopy gives access to in-plane momentum space (k-space) of the light that comes from the samples [117] and allows investigation of photon emission and scattering processes in nanophotonic devices. This method is especially useful when measuring plasmonic excitations [118].

Light emission and scattering properties of single point-like particles are not isotropic but are represented by a sine square radiation pattern, which is typically referred to as the "doughnut pattern". Therefore, the light collected from such a particle will be strongly dependent on the collection angle and the dipole orientation. BFP imaging technique has been used to investigate dipole orientation properties of single molecules [119]. Later on, this technique has been used to investigate dipole orientations in various other nanophotonic platforms [120, 121]. Radiation patterns can be manipulated by the implementation of nano-scale structures. This is achieved due to the interference of the scattered light, which is dependent on the size, shape, and nature of the nanophotonic device [122]. Precise manufacturing of the structures of nanophotonic devices, therefore, gives a wide range of available radiation patterns [123].

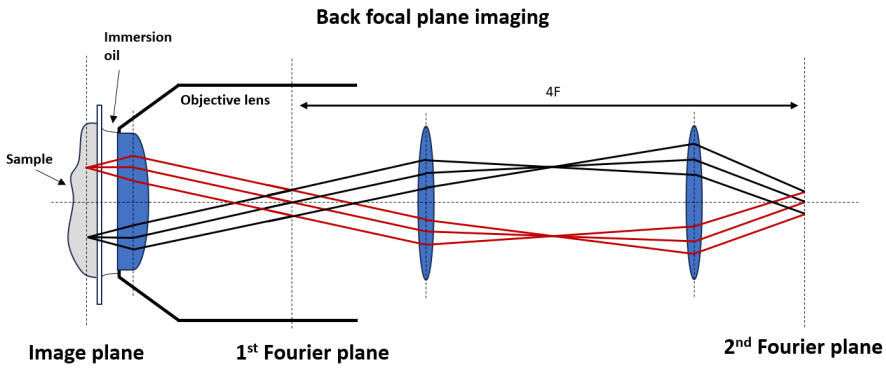

2.6 Fig. Schematic representation of BFP imaging configuration. Light rays emitted from two spatially separate spots on the sample focus according to the angle of radiation on 1^{st} Fourier plane. Images formed on 1^{st} Fourier plane are re-imaged by a double lens setup on 2^{nd} Fourier plane.

BFP imaging is based on the Fourier transformation properties, therefore, the technique has several names, such as *Fourier microscopy*, *k-space imaging*, *momentum resolved optical characterization*, *energy and momentum spectroscopy*. Fourier transformations provide the ability to decompose any signal into its frequency components, offering a way to analyze, synthesize, and filter various signals and extract additional information. When considering optical signals used for imaging, one usually studies intensity profiles formed at the focal points of optical lenses. Fourier optics describes light propagation based on the plane wave basis. Mathematical treatment starts by summing a range of plane waves, propagating at different angles. This allows to construct any spatially varying light distribution, where the distribution of angular spectrum $E(u, v)$ and spatial distribution $E(x, y)$ are related via the Fourier transform [1, 116]:

$$E(u, v) = \frac{e^{ikf}}{i\lambda f}\mathcal{F}_{f_x, f_y}[E(x, y)], \tag{2.5}$$

$$E(u, v) = \frac{e^{\frac{2\pi i f}{\lambda}}}{i\lambda f}\int_x\int_y E(x, y)e^{-\frac{2\pi i}{\lambda f}(ux+vy)}\,dx\,dy, \tag{2.6}$$

with spatial frequencies $f_x = u/\lambda f$ and $f_y = v/\lambda f$. The wavefront at the focal plane of the lens is the Fourier transform of the input field in the imaging plane of the lens, with an additional phase term appearing due to the effect of wave-front curvature. Imaging in the BFP corresponds to the direct measurement of the radiation pattern of the source, since each wavevector with a specific propagation direction will focus on the specific point in BFP (1^{st} Fourier plane in Fig. 2.6). By placing a second lens with focal length f_2 at a distance $f_1 + f_2$ from the first lens (with focal length f_1), we can effectively perform a reverse optical Fourier transform and obtain the original image of the field. This technique is often referred to as $4f$ *imaging setup*, which obtains the original image at a distance equal to $2f_1+2f_2$ from the input plane. Moreover, the factor f_2/f_1 is the magnification of the optical system and describes the fundamental principle of a microscope. A large magnification is achieved using an objective lens with a small f_1. One of the most important characteristics of the objective lens is the ability to gather light and resolve fine details. This is usually characterized by the numerical aperture (NA) of the lens:

$$\mathrm{NA} = n\sin\left[\arctan\left(\frac{D}{2f}\right)\right] \approx n\frac{D}{2f}, \tag{2.7}$$

NA is a dimensionless parameter that describes the range of angles over which the lens can accept or emit light, n is the refractive index and D is the diameter of the entrance pupil. Air objectives can reach up to 0.95 NA, however, especially designed oil objectives can have NA as big as 1.7 when combined with immersion oil. Experiments were conducted using microscope objective with

NA = 1.49. This corresponds to acceptance angles of around ±78.5°. High NA values also increase the resolution of the objective lens and can be described by Abbe's diffraction limit for the smallest resolvable detail:

$$\Delta \mathrm{x} = \frac{\lambda}{2NA}. \tag{2.8}$$

In practice, the resolution of the imaging system is also influenced by other factors, such as diffraction and optical aberrations. The output signal is thus not an exact Fourier transform described by eq. 2.5, but a convolution with the point spread function of the optical system [1]:

$$E(u,v) = \frac{e^{ikf}}{i\lambda f}\mathcal{F}_{f_x,f_y}[E(x,y)] * \mathrm{PSF}(u,v). \tag{2.9}$$

Spatial filtering is a technique that exploits the Fourier transformation property of a lens, enabling modification of the field in the Fourier plane. Modifications to the image can be carried out by physically blocking some of the light or introducing phase-shifting to the selected components, allowing to perform optical image processing tasks. Typical spatial filtering setups exploit a double-lens $4f$ structure, where the imaging plane is at a distance equal to the focal length of the first lens. BFP image is formed at 1^{st} Fourier plane is a

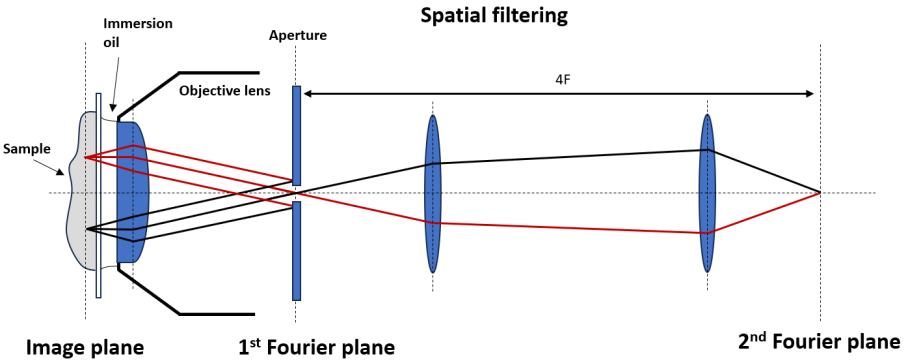

2.7 Fig. Schematic representation of spatial filtering. Light rays are effectively blocked by placing an aperture at the 1^{st} Fourier plane, acting as a low-pass filter in k-space.

Fourier transform of the original image, followed by a second Fourier transform, performed by the second lens. By placing suitable apertures or masks in the Fourier plane, we can modify the nature of images formed after the second lens, which is the main idea behind spatial filtering (Fig. 2.7). Low-pass filtering corresponds to the transmission of low frequency wavevector components $k_{||}$ and is performed by placing an aperture, while, on the contrary, high-pass filtering is performed by placing an opaque mask on the axis, which blocks low

frequency wavevector components and transmits only high frequency. Schematic representation (Fig. 2.7) demonstrates how the light rays emerging at different angles from the sample travel through the lens system. Rays that travel along the optical axis are only allowed to pass through, while the ones that travel at higher angles are effectively blocked by the aperture.

2.3. **Total internal reflection fluorescence**

Total internal reflection fluorescence (TIRF) was used during the experiments. TIRF enables to excite the molecules very close to the surface without exciting regions farther away. The excitation depth is typically < 100 nm from the sample surface. The excitation is performed by the evanescent field, resulting in very low background emission and almost no out-of-focus fluorescence [124]. Method is based on excitation using evanescent fields, which are formed at the interface between two media at a critical excitation angle. When the angle of incidence exceeds the critical angle θ_c (Eq. 3.7), TIR occurs, and the evanescent wave is formed. The electric field of this wave decays exponentially with distance from the interface, enabling highly sensitive probing of surface layers, while avoiding the excitation of molecules above.

Several different optical configurations can be employed for TIRF. For example, excitation using a prism can be performed, similarly to the TIRE configuration used in ellipsometry. Experiments were performed which involve using a high (NA $= 1.49$) microscope objective. Using an objective, a supercritical angle was achieved upon illumination through the objective. The excitation beam was contained within the objective's pupil emerging with a narrow angular dispersion. This was achieved by focusing the beam on the BFP of the lens. By shifting the focus to an off-axis position, the beam emerged at a controllable angle into immersion oil (Fig. 2.8), with the maximum angle limited by the NA. Laser excitation beam focus was shifted using mechanical translation stage with micrometer precision.

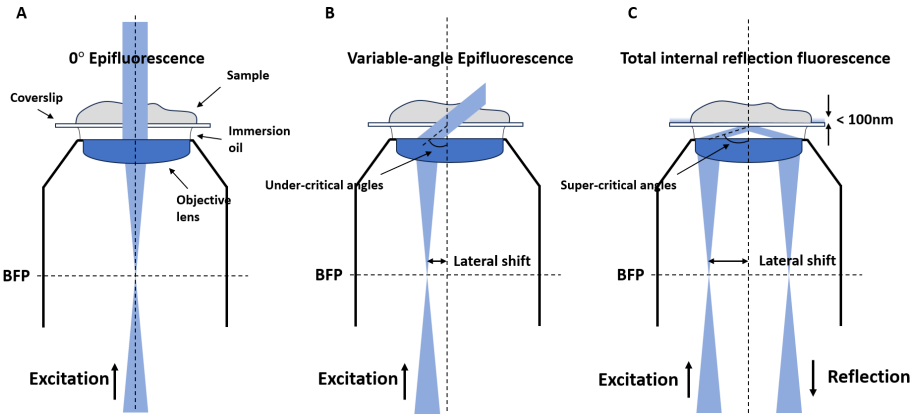

2.8 Fig. Total internal reflection fluorescence configuration using microscope objective lens: (a) and (b) excitation is performed using variable angle laser illumination for laser incidence below critical angle; (c) excitation through near-field for laser incidence above critical angle.

2.4. **Photoluminescence**

Photoluminescence was detected and investigated from uncoupled PMMA-R6G and coupled AG/PMMA-R6G samples. Detection was performed in reverse-Kretschmann configuration (Fig. 2.9), with excitation laser impinging perpendicularly to the PMMA-R6G side of the sample. The samples were excited using EKSPLA Nd:YAG laser source equipped with an external parametric generator (210 - 2600 nm). Excitation was set to 132 µW at $\lambda = 480$ nm and pulse duration around ∼4.5 ns. Detected light was collected from the hemispherical glass side. Fiber probed was placed on the rotational stage with detection angles ranging from 40° to 50°. Fiber probe was connected to a Czerny-Turner type spectrum analyzer (Hamamatsu PMA-12) with wavelength accuracy of $< \pm 0.75$ nm. Acquisition time was set to 10 s.

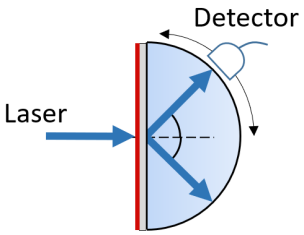

2.9 Fig. Photoluminescence detection in reverse-Kretschmann configuration using hemispherical glass. Excitation with a 480 nm laser and detection at a variable angle using a fiber probe connected Czerny-Turner type spectrum analyser.

2.5. **Total internal reflection ellipsometry**

Spectroscopic ellipsometry (SE) is a powerful tool used for characterizing thin films and surfaces by measuring changes in the polarization state of light upon reflection. It provides highly accurate information about film thickness, materials' refractive index and extinction coefficient, and other material properties [125–127]. In SE, the reflected light is analysed by the change in the polarization and is quantified by two parameters: Psi (Ψ), which describes the amplitude ratio, and Delta (Δ), which describes the phase difference between p- and s-polarized components. These quantities are related using the equation:

$$\rho = \frac{r_p}{r_s} = \tan\Psi\, e^{i\Delta}, \tag{2.10}$$

where r_p and r_s denote the reflection coefficients for p- and s-polarized light, respectively [125]. For a single interface, the complex reflection coefficients are:

$$r_p = \frac{n_t \cos\theta_i - n_i \cos\theta_t}{n_t \cos\theta_i + n_i \cos\theta_t}, \tag{2.11}$$

$$r_s = \frac{n_i \cos\theta_i - n_t \cos\theta_t}{n_i \cos\theta_i + n_t \cos\theta_t}, \tag{2.12}$$

where n_i and n_t are the refractive indices of the incident and transmission media, respectively. θ_i denotes the angle of incidence (AOI), and θ_t is the transmission angle, which is related to θ_i using Snell's law [40].

SE is widely employed to measure thin-film thickness with sub-nanometre precision, essential in fields such as semiconductor manufacturing, coatings, and biofilm analysis. In addition to thickness, SE provides the optical constants n (refractive index) and k (extinction coefficient), which are used for understanding a material's optical response. The technique can also provide information on composition, crystallinity, and other material properties [128]. Since SE measurements can be performed across a broad spectral range from ultraviolet to infrared—it enables comprehensive material characterization [129].

A typical SE setup consists of a broadband light source, polariser, analyser, and a detector (Fig. 2.10). Polarisers define the polarization state of the incident beam, while analysers measure the polarization state after reflection, thus providing the ellipsometric parameters Psi (Ψ) and Delta (Δ). These parameters are directly related to the film's refractive index and thickness. As in conventional ellipsometry, total internal reflection ellipsometry (TIRE) determines the ellipsometric parameters Ψ and Δ, which are modified by the optical properties of the film or surface layer interacting with the evanescent field. In TIRE, the use of total internal reflection further enhances surface sensitivity, making precise control and measurement of polarization essential for reliable results [127]

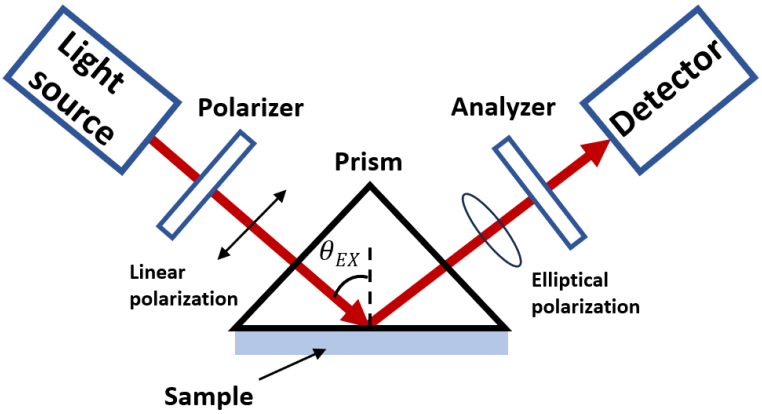

2.10 Fig. A typical spectroscopic ellipsometry setup consists of a white light source to illuminate the sample, a polarizer, a compensator (positioned in the path of either the incident or reflected beam), an analyzer (a second polarizer), and a detector.

Theoretical models are used to extract valuable information about the material's properties from measured ellipsometric data. This process typically involves fitting the experimental results to a model describing the sample structure, often performed with advanced software tools [128]. For multilayer films, the overall reflection coefficient is calculated using a transfer matrix approach, which accounts for multiple reflections within the stack. The complex dielectric function, ε, is related to the refractive index (n) and extinction coefficient (k) by:

$$\varepsilon = (\tilde{n})^2 = (n + ik)^2. \tag{2.13}$$

For a thin film of thickness d deposited on a substrate, the total reflection coefficient can be written as

$$\rho = \frac{r_{12} + r_{23}e^{2i\delta}}{1 + r_{12}r_{23}e^{2i\delta}}, \tag{2.14}$$

where r_{12} and r_{23} denote the reflection coefficients at the air–film and film–substrate interfaces, respectively, and δ represents the phase thickness:

$$\delta = \frac{2\pi}{\lambda} n_2 d \cos(\theta_t). \tag{2.15}$$

TIRE is an advanced optical technique that integrates the principles of ellipsometry with total internal reflection to analyze thin films and surface properties with high sensitivity. It exploits the evanescent wave generated under total internal reflection (TIR) conditions to probe the sample.

Light undergoes TIR at the interface between a high-refractive-index prism and a medium of lower refractive index. This reflection generates an evanescent

wave that penetrates only a short distance into the sample. By measuring changes in the polarization state of this evanescent field, information about the sample's surface and thin-film properties can be extracted.

When employing the TIR configuration, where $\theta_i > \theta_c$, the behavior of the ellipsometric parameters Ψ and Δ differs from that observed under conventional external incidence in SE. In this regime, the transmission angle θ_t loses its physical meaning, as the angle of transmission and becomes a complex-valued angle θ_1, where θ_0 is the AOI

$$\cos\theta_1 = -i\sqrt{\left(\frac{\sin\theta_0}{\sin\theta_c}\right)^2 - 1}. \tag{2.16}$$

Thus, for purely dielectric media (n_0 and n_1 represent refractive indices of the media), the Fresnel expressions would be

$$r_s = \frac{n_0\cos\theta_0 + in_1\sqrt{\left(\frac{\sin\theta_0}{\sin\theta_c}\right)^2 - 1}}{n_0\cos\theta_0 - in_1\sqrt{\left(\frac{\sin\theta_0}{\sin\theta_c}\right)^2 - 1}}, \tag{2.17}$$

$$r_p = \frac{n_1\cos\theta_0 + in_0\sqrt{\left(\frac{\sin\theta_0}{\sin\theta_c}\right)^2 - 1}}{n_1\cos\theta_0 - in_0\sqrt{\left(\frac{\sin\theta_0}{\sin\theta_c}\right)^2 - 1}}, \tag{2.18}$$

From this, it can be seen that reflection coefficients are complex numbers with unit modulus $|r_p| = |r_s| = 1$ and with phases δ_p and δ_s given by

$$\delta_s = 2\arctan\left(\left(\frac{\sin^2\theta_0 - \sin^2\theta_c}{1 - \sin^2\theta_0}\right)^{1/2}\right), \tag{2.19}$$

$$\delta_p = 2\arctan\left[\left(\frac{\sin^2\theta_0 - \sin^2\theta_c}{1 - \sin^2\theta_0}\right)^{1/2}\left(\frac{1}{\sin\theta_c}\right)^2\right]. \tag{2.20}$$

If we look to the variation of ellipsometric parameters Ψ and Δ for the case $\theta_t > \theta_c$ it gives further expressions for $\theta = 45°$

$$\Delta = \delta_p - \delta_s = 2\arcsin\left(\frac{\sqrt{\sin^2\theta_0 - \sin^2\theta_c}}{\sin\theta_0\tan\theta_0}\right), \tag{2.21}$$

a value of $\Psi = 45°$ arises naturally under TIR, since the p- and s-polarized components have equal amplitudes at angles of incidence $\theta_t > \theta_c$. In contrast, the nonzero value of Δ and its angular dependence result from the difference in phase shifts between r_p and r_s [130]. In this regime, the critical angle becomes complex and is associated with the evanescent field propagating along the

interface between two media of differing refractive index. This optical configuration is closely related to those employed for surface plasmon resonance (SPR) excitation; however, by combining ellipsometry with TIR, TIRE provides enhanced capabilities to analyze in detail the polarization properties of reflected, absorbed, and emitted light from plasmon–exciton polaritonic states.

TIRE is particularly advantageous for investigating thin films, surface coatings, and biological layers, offering high sensitivity to subtle changes at interfaces. It has found broad application in biosensing, surface chemistry, and nanotechnology [131, 132]. Compared with conventional spectroscopic ellipsometry, TIRE provides improved sensitivity in measuring the ellipsometric parameters Ψ and Δ [130].

2.6. **Cauchy and effective media Bruggeman models**

Several approaches to determine the relationship between the refractive index and wavelength of the light can be employed. For example, the Sellmeier and Cauchy equations allow to determine the dispersion of light empirically. The most general form of the Sellmeier equation is:

$$n^2(\lambda) = 1 + \sum_i \frac{B_i \lambda^2}{\lambda^2 - C_i}, \tag{2.22}$$

Here n is the refractive index, λ is the wavelength, and B_i and C_i are coefficients determined experimentally. While the Cauchy dispersion relation between refractive index and wavelength of light is determined by:

$$n(\lambda) = A + \frac{B}{\lambda^2} + \frac{C}{\lambda^4} + \cdots . \tag{2.23}$$

Similarly to the Sellmeier equation, A, B, and C coefficients are determined by fitting the equation to a known material $n(\lambda)$ dispersion measured experimentally. Although both of the descriptions provide the $n(\lambda)$ dispersion relations for given A, B, and C coefficients, the Cauchy formula is only valid in the visible region of the normal dispersion regime. The equation becomes inaccurate in the infrared region or when describing anomalous dispersion. Only later was the approach extended by Sellmeier to handle the anomalously dispersive regions, giving a more accurate model in the ultraviolet, visible, and infrared spectra.

Optical constants of mixed materials are usually calculated using EMA (Effective Medium Approximation) models. These models are typically based on mixing the optical constants of several (usually two) materials. Modelling typically includes the percentage of constituent materials, depolarization factor,

and calculation type. The most common mixing methods are linear combination, Maxwell-Garnett EMA, and Bruggemann EMA. A simple interpolation between the constituents of the dielectric function is provided by linear mixing. Maxwell-Garnett EMA is based on spherical incorporation of material No. 2 into existing host material No. 1. Bruggemann's description for the mixture of two materials with permittivities ε_1 and ε_2 and corresponding concentrations c_1 and c_2:

$$\varepsilon_{\text{eff}} = \frac{H_b + \sqrt{H_b^2 + 8\varepsilon_1\varepsilon_2}}{4}, \tag{2.24}$$

With

$$H_b = (3c_2 - 1)\varepsilon_2 + (3c_1 - 1)\varepsilon_1. \tag{2.25}$$

However, Bruggemann EMA makes the choice of the host material. These methods are very useful for describing roughness properties between layers as well as mixing between amorphous and crystalline materials.

2.7. **Sample preparation**

2.7.1. Magnetron sputtering

Metal films, required to sustain surface plasmon excitations, were fabricated using magnetron sputtering (Kurt J. Lesker PVD 225). Magnetron sputtering is a physical vapor deposition (PVD) method in which thin films are formed by ejecting atoms from a solid target material and depositing them onto a substrate. The process takes place in a vacuum chamber filled with a low-pressure inert gas, typically argon. When a negative voltage is applied to the target (the cathode), a plasma is generated: free electrons accelerate toward the target, colliding with argon atoms and ionizing them. The positively charged argon ions are then accelerated toward the negatively charged target, striking it with enough energy to sputter atoms from its surface.

In magnetron sputtering, magnets are placed behind the target to create a magnetic field parallel to the target surface, which traps secondary electrons near the surface. This confinement increases the plasma density and enhances ion bombardment efficiency, allowing higher deposition rates at lower working pressures compared to conventional sputtering. The ejected target atoms travel through the plasma and condense on the substrate, forming a thin, dense, and uniform coating. The process parameters—such as power, gas pressure, substrate temperature, and target-to-substrate distance—can be finely tuned to control film thickness, composition, and microstructure. Variations of the technique, including DC, RF, and reactive magnetron sputtering, enable deposition of both metallic and compound films for applications in microelectronics,

optics, tribology, and energy devices.

Experiments were done with a 45 nm thickness silver (Ag) layer, which was formed by magnetron sputtering technology on a clean glass cover slip (CS). CS thickness was 170 µm.

2.7.2. Spin coating

Spin coating is a simple yet effective technique to produce thin films ranging from a few nanometers to a few microns in thickness. The process consists of depositing a small amount of liquid material onto the center of the substrate, which is rotating at high angular velocity. The process typically consists of four stages:

Deposition

This stage starts by placing the substrate on the spin coater machine, where the coated material is dropped on the substrate surface in a liquid form. The substrate can either be slowly rotating (dynamic deposition) or not rotating (static deposition). The size of the drops of the coating material depends on the size of the substrate and the viscosity of the coating solution. When in the dynamics deposition stage, material is dispersed while the substrate is slowly rotating at around 500 rpm.

Spin Up

During spin up stage, the substrate will begin to increase spin until it reaches speeds of around 3000 rpm. At this stage, centrifugal forces come into play. Initially, the fluid spins at a different rate than the substrate, but the drag will increase the spinning speed of the liquid to match the substrate, leading to the fluid becoming uniform. Film thickness decreases, depending on the speed and rotation time on the spin coater.

Spin Off

After reaching the required rotational speed, the thinning process is dominated by viscous forces. Film thinning process is controlled, however, the thickness is dependent on the surface tension, viscosity, and rotation speed. Due to interference effects in the film, the fluid starts to change colors.

Evaporation

During this stage, the fluid outflow stops, and the thinning is dominated by evaporation of the solvent. However, the rate of evaporation depends on the ambient conditions and solvent volatility. Non-uniformity in the film thickness can arise due to the non-uniform evaporation rate of the solvent.

During the experiments, samples were fabricated using poly(methyl methacrylate) (PMMA) doped with Rhodamine 6G (R6G), by dissolving PMMA (c = 0.1 µM; c_m =0.0367 g/L) and R6G (c = 25 mM) separately in ethanol. Coating solution was obtained by mixing the PMMA and R6G solutions at the volume ratio of 2:1. Spin coating at 3000 rpm for 30 seconds was performed after depositing the coating solution onto silver coated substrates. Acceleration was held at a constant value for all samples. Spin coated PMMA-R6G layer formed a uniform thickness of around 20 nm, as measured with a profilometer.

3. SURFACE ADSORBED PROTEIN-DYE COMPLEX OPTICAL BIOSENSING USING PLASMONIC STRONG COUPLING

Various immunosensing applications employ labeled and non-labeled proteins. Techniques such as SPR are highly sensitive to changes in refractive index, thus, SPR is commonly used in commercial optical sensors [133].

Immunosensing based on biomarkers has become a valuable approach in disease research, including cancer [134], cardiovascular disorders [135,136], and other health-related conditions [137]. In particular, proteins tagged with fluorescent biomarkers are widely used in biosensing because of their low detection limits [46, 137, 138] and the broad availability of fluorescent dye molecules. This makes biomarkers a cost-effective and versatile option for immunosensing. However, fluorescent dyes are prone to photobleaching, primarily caused by interactions between the long-lived triplet states of the fluorophore and environmental oxygen [139]. Photobleaching shortens fluorescence lifetimes and diminishes signal intensity. At low analyte concentrations, this effect is more pronounced, further complicating detection. Despite these challenges, fluorescence-based immunosensing remains highly sensitive, affordable, and time-efficient, and numerous signal enhancement strategies have been developed to overcome its limitations [140–143].

A recent strategy for suppressing photobleaching involves the use of metal nanostructures, which enhance the optical properties of fluorophores and improve both fluorescence intensity and quantum yield [144,145], thereby lowering the detection limit of proteins. This enhancement arises from the localized electric fields generated under plasmonic excitation within the metallic nanostructure. Despite the high sensitivity of fluorescent dye–labeled methods, with detection limits on the order of tens of pg/mL [138], their broader applicability remains restricted by photobleaching. Photobleaching lasting up to several minutes—can distort real-time immunosensing kinetics.

To address these limitations, label-free techniques such as SPR have gained prominence [146]. SPR relies on surface plasmon polaritons, which are surface electromagnetic waves excited at the metal–dielectric interface. This light–matter interaction confines light into nanometer scale. SPR occurs at a specific frequency when the incident electromagnetic field couples to the collective oscillations of conduction electrons at the metal surface. Since the in-plane plasmon wave vector exceeds that of light in vacuum, coupling elements such as prisms or gratings are necessary to excite SPR. The method has been widely adopted in biosensing for monitoring protein kinetics [147] and quantifying ad-

sorbed protein mass using Feijter's formula [148]. SPR owes its success to the high spectral sensitivity of its modes; however, its performance is ultimately limited by absorption and scattering losses in the metal layer [13, 149]. Strategies to minimize these losses and enhance sensitivity remain a central research goal [150–152].

A promising direction is the combination of plasmonic resonance with excitons from fluorescent dye–labeled proteins, which mitigates the limitations of both approaches: metallic losses in SPR and photobleaching in fluorescence-based biosensing. When appropriate conditions are established for plasmon–exciton interaction, fluorescence enhancement can be achieved through mode coupling. Depending on structural geometry, excitation distance, and energy alignment, the interaction may occur in either the weak or strong coupling regime. Strong light–matter interactions enable not only electromagnetic modifications [153] but also control over material properties, including the modulation of chemical reactivity [22, 154]. This capability opens new opportunities to mitigate photobleaching in immunosensing.

The effects of plasmon–exciton strong coupling have been extensively studied in metallic nanostructures, and J-aggregate systems [55], but remain less explored in photochemical reactions and biosensing applications. Recent theoretical work has shown that in quantum plasmonic immunoassays, sensor sensitivity can be enhanced via strong coupling between metal nanoparticle plasmons and excitons in fluorescent dye–labeled proteins [155]. Furthermore, strong coupling has been demonstrated to suppress photo-oxidation of organic molecules [63]. Nonetheless, the relationship between strong plasmon–exciton coupling in dye-labelled proteins and the Rabi splitting with respect to adsorbed protein mass remains largely unexplored.

A numerical study of strongly coupled labelled proteins and SPR is performed and presented here. A sensing methodology is proposed and demonstrated that allows the evaluation of the adsorbed protein mass on a metal surface. In particular, the evaluation of adsorbed mass is performed due to the formation of polaritonic modes. This is possible due to Rabi splitting, which depends on the concentration of the particles participating in strong coupling.

The results presented in the following chapter were originally published: Jurkšaitis, P.; Bužavaitė-Vertelienė, E.; Balevičius, Z. Strong Coupling between Surface Plasmon Resonance and Exciton of Labeled Protein–Dye Complex for Immunosensing Applications. Int. J. Mol. Sci. 2023, 24, 2029. https://doi.org/10.3390/ijms24032029.

The author modeled the absorption spectrum and refractive index of the HSA protein-dye complex. He performed numerical simulations of coupled HSA protein molecules and evaluated the dependence of the Rabi splitting on the molecular concentration. The author prepared the initial manuscript in collaboration with the supervisor and co-author.

3.1.1. Numerical analysis: uncoupled case

The optical response of a multilayered structure was investigated in the TIR configuration. The sample consisted of a uniform gold film (45 nm) with a labeled or non-labeled protein layer (HSA) on bottom. The structure was in direct contact with water (Fig.3.1). Reflectance of p-polarized light from two samples involving labeled HSA protein and non-labeled HSA protein was compared. *Alexa Fluor*^{TM} 633 (further A633) was used for labeling of HSA protein, with excitation at 633 nm. Typical thicknesses of metal layer, required

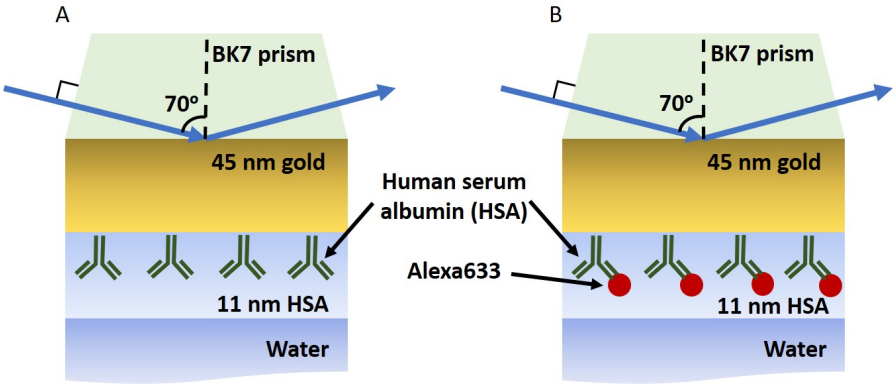

3.1 Fig. Schematic representation of modelled systems: (A) BK7/Au (45nm)/HSA in direct contact with water; (B) BK7/Au (45nm)/ HSA-A633 in direct contact with water.

to excite surface plasmon mode must be of the order of 10s of nanometers therefore, a thickness of 45 nm was chosen for the gold layer. The dispersion of an uncoupled SPP is represented by a single line that depends on the angle of incidence (Fig. 3.3a). Upon modelling with label-free HSA layer, a shift in the spectrum of the reflected p-polarized light occurs, which is around 135 meV at 70° AOI.

Absorption spectrum of A633 was modelled as two Lorentzian oscillators (Fig. 3.2A). Numerical calculations of the refractive index of the HSA protein molecule in the visible frequency spectrum were performed using the Cauchy function with coefficients A = 1.567, B = 0.0022 and C = 0 at normal dispersion regime (Fig. 3.2B). HSA molecule has a thickness which is dependent on the orientation of the structure [156], however, on average, the value can be estimated to be around 11 nm, assuming a random distribution of HSA molecules on the gold surface. Modelling has been performed at a spectral range between 400 nm to 1000 nm, for incident angles between 60° to 90°. Label-free gold nanolayer was investigated and used as a reference signal for comparison

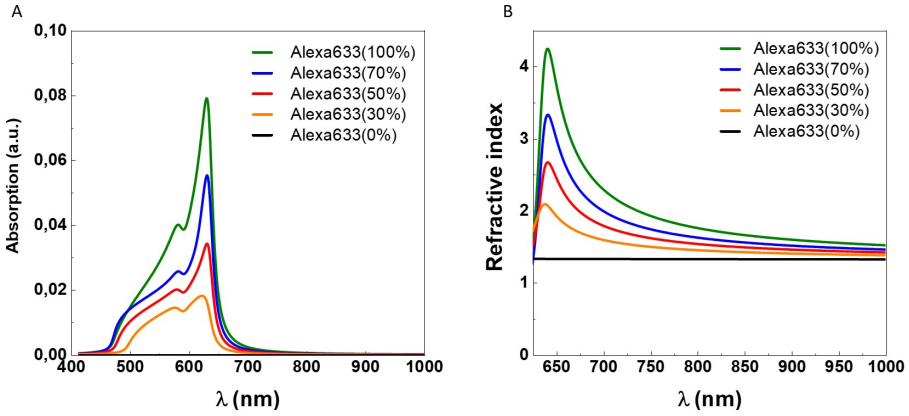

3.2 Fig. Modelled absorption (A) and refractive index (B) of HSA protein-dye complex at different concentrations of A633 molecular dye. Cauchy coefficients A = 1.567, B = 0.0022, C = 0.

with the labeled sample, indicating an adsorbed surface mass of protein molecules. Laber-free HSA protein layer was replaced by the dye-labeled protein HSA-A633 dye complex, which was characterized by a Cauchy function describing refractive index of HSA-A633. Dye absorption spectrum of A633 was modeled using two Lorentzian oscillators, with energies of 1.96 eV and 2.13 eV. Absorption spectrum of A633 dye complex was simulated to match experimentally available data [157]. In contrast with typical SPP dispersion, A633

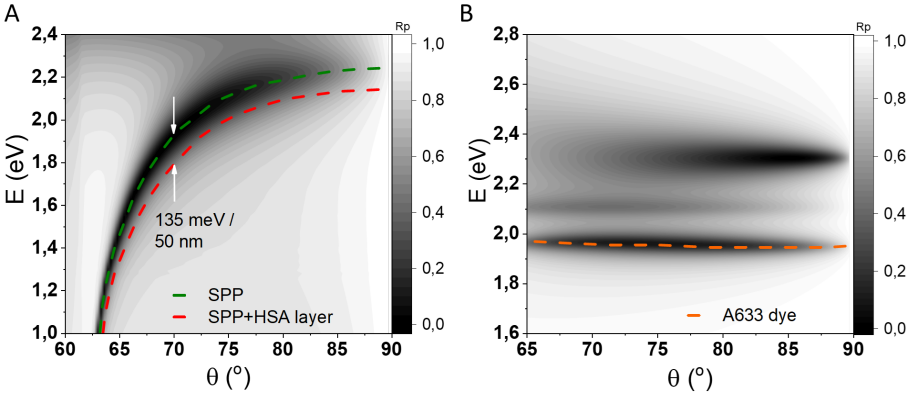

3.3 Fig. Dispersion relations of calculated p-polarized reflection intensity maps: (a) SPP dispersion relation. The orange dashed line indicates dispersion of a single SPP, and the red dashed line indicates dispersion with a non-labeled HSA layer on top. White arrows indicate about 50 nm shift at 70° AOI; (b) Dispersion of A633 molecular dye with absorption peak indicated by orange dashed line.

molecular dye is non-dispersive, thus the absorption and emission properties

do not depend on AOI (Fig. 3.3B). Single molecular exciton dispersion can be seen in Fig. 3.3B. The optical response of the A633 molecular exciton of 100% concentration was modelled for different angles of incidence, showing no dependence. Different molecular absorption peaks correspond to several dispersion lines appearing in Fig. 3.3B, with maximum absorption at 1.96 eV.

3.1.2. Numerical analysis: strongly coupled case

Combining the two excitations in a way that dispersions of the SPP and A633 cross, new polaritonic states are created, which shift the energies in the dispersion map. This happens if the electric field of the plasmon resonance significantly overlaps with the dipole moment of the A633 exciton. Changes in spectral response become experimentally detectable whenever the shift in energies is greater than the linewidth of individual resonances, and the system transitions to the strong coupling regime [27]. These states become inextricably linked, thus modifying reflectance spectra, which can be measured using spectroscopic ellipsometry. New hybrid modes emerge due to the coupling of SPP and A633 labeled protein layer (Fig. 3.4). A study of strong coupling dependence on the fluorescent dye concentration was performed for BK7/Au(45nm)/HSA(11nm)-A633/water structure. The dye-labeled HSA–A633 protein complex was modeled as a thin (11 nm) layer composed of A633 dye, HSA protein and deionized water in varying mixing ratios. The composition was expressed as the percentage of protein–dye within the layer, ranging from 100% pure protein–dye to 0% (pure deionized water). Mixing two optical dispersions of the deionized water and the HSA-A633 complex results in changes in refractive indices and extinction coefficients for different concentrations therefore, the relative concentrations of the materials are taken into account. EMA Bruggeman's model was used to model the optical response of ellipsometric parameters describing the effective dielectric function. Absorption spectra and refractive index for different mixing ratios (relative concentrations) are depicted in Fig. 3.2. Two absorption peaks of A633 can be seen at 583 nm and 633 nm. Absorption and refractive index of A633 molecular dye are depicted as a green line. As the number of HSA–A633 complex molecules decreases, the absorption and refractive index coefficients approach the values of deionized water.

The magnitude of the p-polarized wavevector $k_{||}$ component changes at the BK7 prism/gold layer boundary, due to different incident angles on the sample. This allows us to evaluate the dispersion relation of SPP, since the excitation is dependent on the wavevector $k_{||}$ magnitude. To evaluate the coupling strength as a function of concentration of labeled protein particles, simulations using SPP and exciton dispersions were performed. Concentration was varied be-

tween 100% and 0%. Dispersion of hybrid modes at the strong coupling regime for different A633 concentrations is shown in Fig. 3.4. Uncoupled SPP and A633 exciton dispersion relations correspond to red dashed lines.

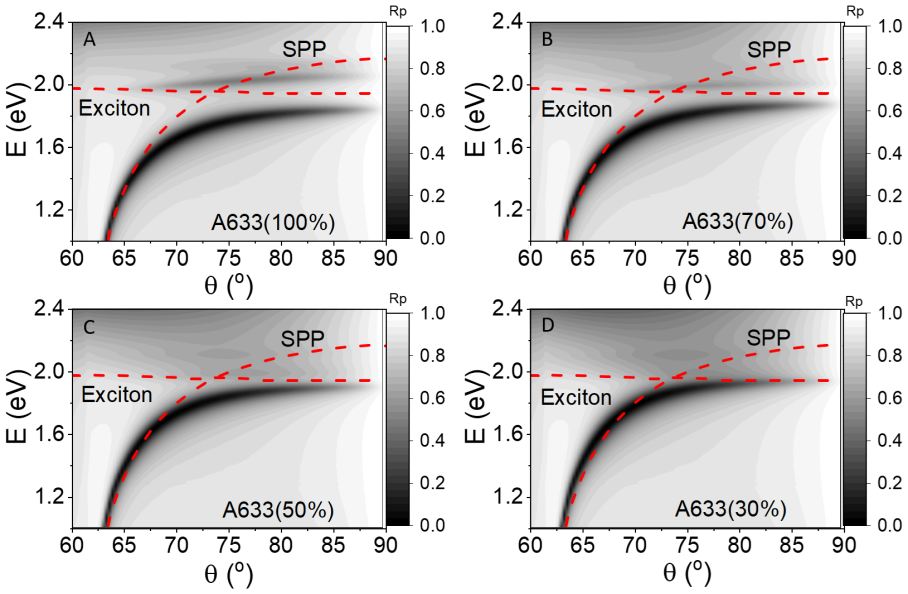

3.4 Fig. Numerically modelled hybrid SPP-exciton polariton dispersion maps at different A633 concentrations: (**a**) 100%, (**b**) 70%, (**c**) 50% and (**d**) 30%.

A strong coupling regime is apparent from numerical simulations, which show that SPP and A633 dispersion relations are modified from initial optical dispersions. Upper and lower polariton branches are formed. With a concentration of 100%, Rabi energy splitting is 264 meV at 74° AOI (Fig. 3.4a). Moreover, Rabi splitting decreases with the decreasing HSA-A633 concentration. For 70% interaction strength decreases to 198 meV, and for 30% the strength is 161 meV. For 30% strong coupling regime is absent due to a low number of interacting molecular excitations. Using the equation, which directly relates Rabi frequency (Ω_R) to the number of particles (Eq. 1.13). We can directly evaluate the number of proteins adsorbed by the gold surface from dispersion data:

$$\frac{N}{V} = \frac{\Omega_R^2 \varepsilon_0 m_e}{e^2} \tag{3.1}$$

Where ε_0 is vacuum dielectric constant ($8.85 * 10^{-12} Fm^{-1}$), e is the electron charge ($1.602 * 10^{-19} C$) and electron mass m_e is ($9.109 * 10^{-31} kg$). Analysis of the Rabi gap between polaritonic states was performed as a function of incident in-plane wavevector k. The Rabi energy gap varied from 88 meV to 140 meV, increasing with higher concentrations of labeled protein (55% to 100%). Moreover, further enhancement of the coupling strength was only achievable by

introducing a larger number of participating particles, such as pure fluorescent molecules without protein.

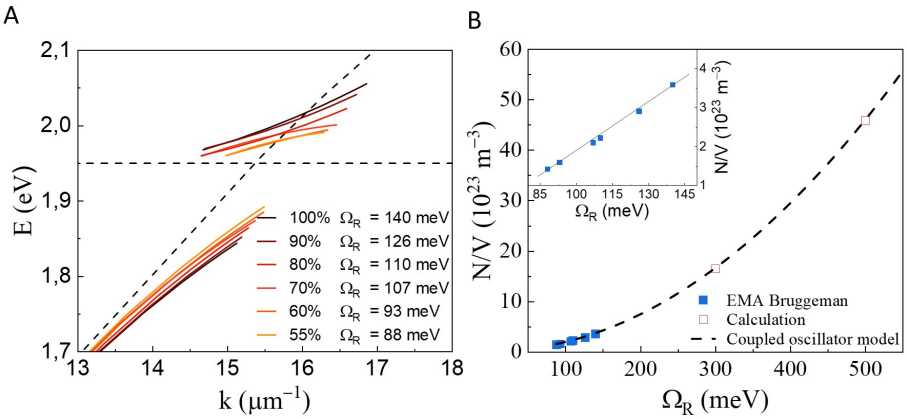

3.5 Fig. Dispersion of strongly coupled SPP-exciton in wavevector domain at different concentrations (55-100%) of protein-dye complex (left) and protein molecule concentration adsorbed on the surface as a function of modelled Rabi energy gap (right).

The concentration of proteins adsorbed onto the surface can be determined from the Rabi gap using Equation 3.1. Based on the wave vector dispersion results (Fig. 3.5b), the concentration of adsorbed HSA–A633 complex molecules was calculated. To simulate complete gold surface coverage, the total number of HSA–A633 complexes in the volume (N_{total}) must exceed the number of molecules bound to the gold surface (N). Because the electromagnetic field of the SPP mode is confined to the gold/water interface, strong SPP–exciton coupling occurs only at small separations (on the order of tens of nanometers), where the electric fields of both modes overlap significantly. The thickness of the adsorbed dye-labeled protein layer is comparable to this interaction distance, making the number of labeled molecules directly proportional to the adsorbed protein mass.

In the present model, the HSA–A633/water layer was 11 nm thick, meaning that the molecular concentration (N/V) is proportional to the number of molecules adsorbed onto the surface. For the full coverage case, the fill factor (N_{vol}/N) must equal 1; therefore, the fill factor of the HSA–A633 complex was set to 100%. Under these conditions, the Rabi energy gap was $\Omega_R = 140$ meV ($3.385 * 10^{13} s^{-1}$). From Equation 3.1, the corresponding number of molecules adsorbed on the gold surface (density of states) was determined to be $N/V = 3.595 * 10^{23} m^{-1}$.

Since the concentration of molecules (N/V) is proportional to Ω^2, the dependence of the HSA–A633 complex concentration on the Rabi gap was evaluated for the water/HSA–A633/Au/BK7 structure (Fig. 3.5b). The calculated

values (red squares) exhibit a parabolic relationship, as shown by the fitted curve. However, because the Rabi gap in simulated plasmon-based nanophotonic structures spans only a narrow range, the variation of Ω with concentration can be reasonably approximated by a linear function. This optical response modelling highlights the impact of strong coupling on dye molecules adsorbed at the sensor surface and suggests that variations in the vacuum Rabi gap can serve as a reliable indicator of changes in the number of attached HSA–dye protein complexes.

3.2. **Summary**

In this study, we demonstrate a hybrid approach that combines a label-free method with labeled proteins by exploiting the strong coupling effect between plasmonic resonances and the dye excitons of target proteins. This strategy provides an alternative pathway for detecting and monitoring protein interactions at the transducer surface by tracking variations in coupling strength between plasmonic modes and molecular emitters. Our results show that the Rabi oscillations exhibit a parabolic dependence on the number of labeled proteins adsorbed onto the sensor surface. However, under realistic experimental conditions in photonic–plasmonic systems, the Rabi energy spans only a narrow range and can therefore be approximated linearly. Utilizing strong light–matter coupling in immunocomplexes offers the potential to modify chemical reactivity, alter excited-state relaxation pathways, regulate charge conductivity, and influence protein binding kinetics. Furthermore, the formation of bio-polaritonic states involving proteins opens opportunities beyond biosensing, including their application in quantum information processing. The realization of strongly coupled states between plasmonic resonances and protein–dye complexes introduces new biosensing concepts, where the integration of label-free and labeled approaches enables tuning of protein interaction kinetics via coupling strength. This may further lead to innovations such as bio-nanolasers and new avenues in polaritonic biochemistry.

4. POLARITONIC EMISSION DYNAMICS UNDER RESONANT AND NON-RESONANT EXCITATION

Plasmonic materials are gaining a lot of attention for the development of coherent light sources at the nanometre scale. Surface plasmons are described as coherent oscillations of free electron plasma, which can directly interact with light under appropriate conditions. Under these conditions, SPPs emerge at the boundary between dielectric and metal. A high field confinement and field enhancement make these states attractive for sensing applications. Moreover, emerging manufacturing technologies have allowed to precisely control the geometry of nanophotonic devices, directly effecting the resonance conditions and improving optical sensing capabilities [26]. Electric field confinement below the diffraction limit is attractive for near field coupling [16, 158], superresolution [159, 160]. Field enhancement allows to observe plasmonic lasing [161, 162]. Under weak coupling conditions, Purcell effect emerges, further increasing or decreasing the fluorescence rates [92, 94]. In the strong coupling regime, interactions become stronger than the damping rates of SPP and molecular dye [68]. This enables coherent energy exchange between the excitation modes at femtosecond timescales [23, 58]. Semiclassical and quantum descriptions of the phenomena give additional insight into the emerging effects, such as vacuum Rabi oscillations [58, 163], Bose-Einstein condensation [75]. At the strong coupling limit, Hopfield coefficients, describing the polaritonic states, predict highly dispersive behaviours, which open new possibilities to tune optical and material properties [61, 62, 164]. Currently, a lot of attention has been dedicated to polaritonic states and their interactions. For example, polariton-polariton interactions result in coherent phase transition effects, which is used in emerging quantum technologies. The polariton bottleneck effect is another type of polaritonic interaction, which has received much attention lately. This effect occurs due to the interaction with the exciton reservoir (ER) state in the system and hinders the properties of polaritons [81, 82]. Observing interactions with ER states can be complicated when employing only spectroscopic measurement techniques [165]. However, in order to gain additional insight about the transition dynamics of polaritonic states, time-resolved experiments must be performed. Experiments such as time-resolved pump-probe have shown that, in addition to the expected coherent states within the system, some part of excitons remains in an incoherent state when resonantly pumping a polaritonic state [166].

Here, we investigate polariton dynamics within a strongly coupled R6G and SPP system by implementing spectroscopic and temporal measurement

techniques. Strong coupling is achieved in the structure, consisting of a metallic(Ag) thin film deposited on a glass substrate and a PMMA-R6G layer on top. The characteristic dispersion is demonstrated by TIRE and emission from the LP branch. Temporal measurements show that the observed lifetime is dependent on the excitation conditions. We therefore present a model describing interactions between polaritonic states and the exciton reservoir.

The results presented in the following chapter were originally published: Jurkšaitis, Povilas, Anulytė, Justina, Spalinskaitė, Evita, Bužavaitė-Vertelienė, Ernesta, Žičkus, Vytautas, Banevičius, Dovydas, Kazlauskas, Karolis, and Balevičius, Zigmas. "Plasmon–exciton polaritonic emission lifetime dynamics under strong coupling" Nanophotonics, vol. 14, no. 14, 2025, pp. 2485-2493. https://doi.org/10.1515/nanoph-2025-0129.

The author performed experiments using BFP microscopy and TCSPC. This included system design, alignment, data acquisition, and evaluation of the experimental results. Three-level system was suggested and numerically calculated by the author, providing the concept for the whole study. The author participated in a photoluminescence experiment. The author, together with the supervisor and co-authors, wrote the manuscript and made a significant contribution to the reviewer comments.

4.1. **Results**

4.1.1. Spectral characteristics of polaritonic states

Structure under consideration consisted of thin metal (Ag) deposited on a glass substrate (CS) with PMMA-R6G layer on top of Ag and investigated using: (i) TIRE; (ii) angle-dependent fluorescence and (iii) fluorescence lifetime microscopy methods. Measurements were performed using index-matching immersion oil (Cargille, n = 1.515) to connect CS with either the BK7 prism in (i) and (ii) or the objective lens in (iii). Structure consisting of CS/Ag/PMMA-R6G was measured using TIRE, and dispersion relations were obtained of the hybrid SPP-R6G system (Fig. 4.1, inset describes TIRE measurement configuration). Similarly, the dispersion relation of R6G exciton was evaluated using a structure consisting of CS/PMMA-R6G (Fig. 4.1, cyan dashed line) and the CS/Ag/PMMA sample was also measured under the same conditions (Fig. 4.1, white dashed line). Angle-dependent reflection intensity maps of p-polarized incident light exhibited modified dispersion characteristics as compared to single SPP (CS/Ag/PMMA) and molecular dye (CS/PMMA-R6G) dispersion curves. The splitting observed in plasmon-exciton dispersion is proportional to coupling strength g and can be evaluated from Rabi gap (Ω_R) at the anti-crossing point as $g = \Omega_R/2$. Obtaining angle dependent dispersion $E(\theta)$ directly from the

measurement does not correspond to the $E(k)$ dispersion usually discussed in strongly interacting light-matter systems, therefore converting to wavevector dependent dispersion relation shifts the original the anti-crossing point to k = 12.8 μm^{-1}, where Rabi splitting was observed around 400 meV, giving $g = 200$ meV. The observed relation at the anti-crossing point is the main signature of a strong coupling regime [16, 37, 153, 163, 167].

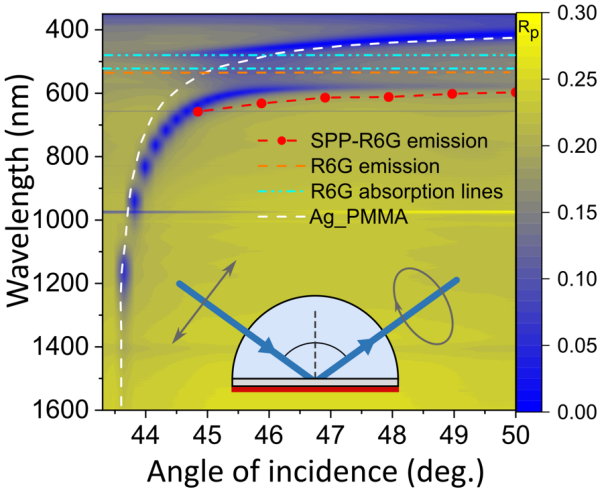

4.1 Fig. Dispersion map of molecular R6G dye and SPP in strong coupling regime measured in TIRE setup. White and cyan dashed lines follow the uncoupled dispersion relations of SPP and R6G, respectively. Coupled and uncoupled R6G emission is indicated by the red dot-dashed line and the orange dashed line, respectively. The Inset represents the experimental TIRE detection scheme.

Evaluation of angle-dependent emission has been performed during photoluminescence measurements of bare CS/PMMA-R6G (Fig. 4.2) and strongly coupled CS/Ag/PMMA-R6G (Fig. 4.3). Both samples were connected to a cylindrical BK7 glass prism using index-matching immersion oil, and the emitted light was collected from the prism side. Samples were excited in reverse Kretschmann configuration with pulsed laser (480 nm) light at 0° incident angle (normal to the surface), shown in Fig. 4.3 inset. Emitted light was collected at angles ranging from 40° to 50°. The measured absorption and emission spectra of uncoupled R6G molecules show that Stokes shift is around 17 nm (Fig. 4.2). As expected, the CS/PMMA-R6G sample did not show angular emission dependence, and the main emission peak was observed at 537 nm, indicative of R6G exciton transition to the ground state. However, when in the strong coupling regime (CS/Ag/PMMA-R6G), angular emission dependence changes radically with the emergence of secondary angle dependent emission peak, which shifts from 670 nm at 44° to 600 nm at 50° emission angles (Fig. 4.3). The

emergence of regular R6G emission peak at 537 nm of the strong coupled sample indicates that a fraction of R6G molecules do not participate in the strong coupling regime. Also, the emission from the secondary peak follows the behaviour of the LP branch observed when performing reflectivity measurements in TIRE configuration (Fig. 4.1, red dot-dashed line), therefore emission from LP is observed. Emission from UP is absent due to rapid non-radiative decay, which is typically observed in molecular exciton systems [168, 169].

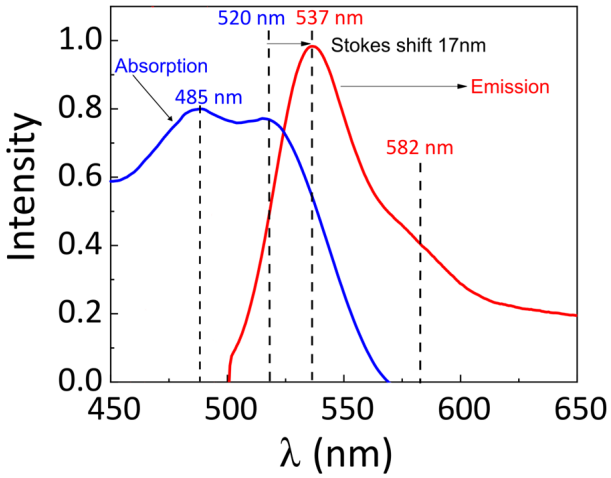

4.2 Fig. Regular R6G molecular dye emission (red line) with emission peaks at 537 nm and 582 nm. Measured absorption spectrum (blue line) has peaks at 485 nm and 520 nm. Stoke shift of around 17 nm. Absorption spectrum was measured using TIRE.

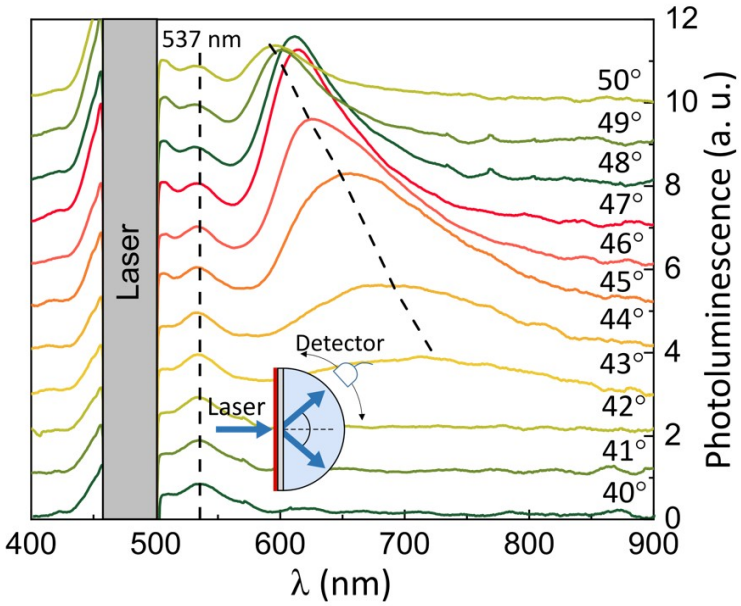

4.3 Fig. Measured emission spectrum of SPP strongly coupled with R6G molecular exciton. Emission of SPP-R6G for angles from 40° to 50°. Dashed lines follow the emission peaks. The inset represents the experimental detection configuration.

Observation of the UP state emission would be challenging using the current experimental setup, due to significant spectral overlap of the excitation laser and UP emission, which is expected at around 480 nm. Due to Rabi splitting (Ω_R) dependence on the concentration of particles participating in the strong coupling regime, a relative contribution from coupled and uncoupled states can be estimated. Calculating the ratio of integrals between coupled and bare R6G dye absorption spectra, taken from TIRE measurements, shows that only around 61% participate in strong coupling, while the rest 39% remain uncoupled. However, in order to describe the influence of the uncoupled states on the polariton decay properties, additional experiments, such as fluorescence lifetime measurements, are performed.

4.1.2. Spatial and temporal measurements

Measurement setup for the detection and analysis of SPCE is shown in (Fig. 4.4). Excitation was performed using a variable incident angle configuration, however, after the critical angle, TIRF is achieved. Index-matching oil (immersion oil) was used between the microscope objective and the sample to

collect the emission from SPP-R6G. Excitation was performed by focusing a picosecond laser (473 nm) onto the BFP of the high numerical aperture (NA = 1.49) objective. Precise control of the beam propagation direction, emanating from the objective lens, was achieved using a translation stage. Fluorescent light was collected by the same objective lens and reimaged onto the CMOS detector to retrieve angular information from the BFP. In conjunction, part of the fluorescence light was also sent to SPAD for investigation of lifetime dynamics. By varying the incident beam angle, a transition between non-resonant and resonant excitation was achieved. Additionally, a dichroic mirror and long-pass filter (FELH0550) at 550 nm were used to block scattered laser light. Polarization analysis was performed by inserting a polarizer in the $4f$ imaging setup.

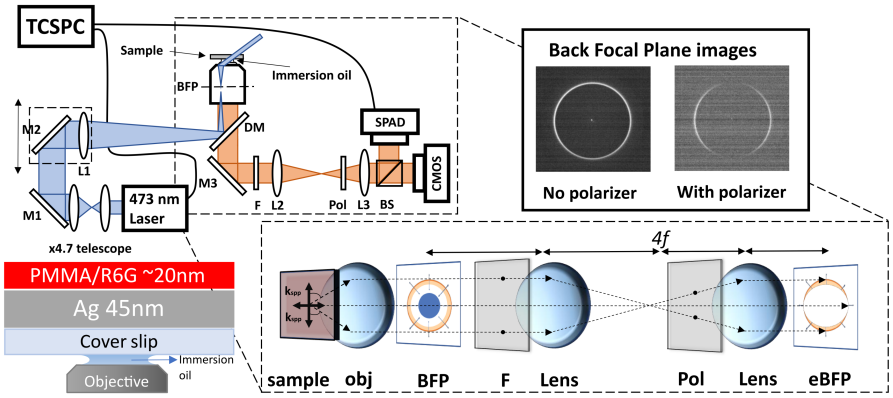

4.4 Fig. Schematic representation of back focal plane imaging setup using variable angle excitation configuration. Image formation at the back focal plane is represented in the inset. Sample structure consisting of CS/Ag/PMMA-R6G is shown at the bottom left.

The far field emission was investigated for different laser excitation angles from 0° to 62.8°. The emission intensity profile recorded by the CMOS detector is shown in (Fig. 4.4 top right), both with and without a polarizer. Position of the emission peaks observed on the detector can be related to emission angles using $\sin(\theta) = NA/n$. Horizontal cross sections along the centre were taken for coupled and uncoupled samples. In case of strongly coupled CS/Ag/PMMA-R6G (Fig. 4.5A) emission peak was found to be at 44.1°. Furthermore, as the laser excitation angles approach resonant conditions, the polariton emission intensity increases accordingly, with the highest intensity observed when exciting at 45.2°. For small incident angles (12.9° - 38.4°), weak polaritonic emission can still be observed due to the non-resonant polaritonic excitation. Comparing with the uncoupled case (Fig. 4.5B) it is evident that the CS/PMMA-R6G sample emits in a wider range of angles with FWHM of 21.3°, while fluores-

cence using plasmonic structure exhibits a much narrower angular emission pattern with FWHM of 4.3°. Plasmonic samples enable to enhancement of the collection efficiency of the fluorescent light, which is crucial when studying molecular interactions [48]. Sharp peak at 0° (Fig. 4.5B) is due to leakage of laser excitation through the filters.

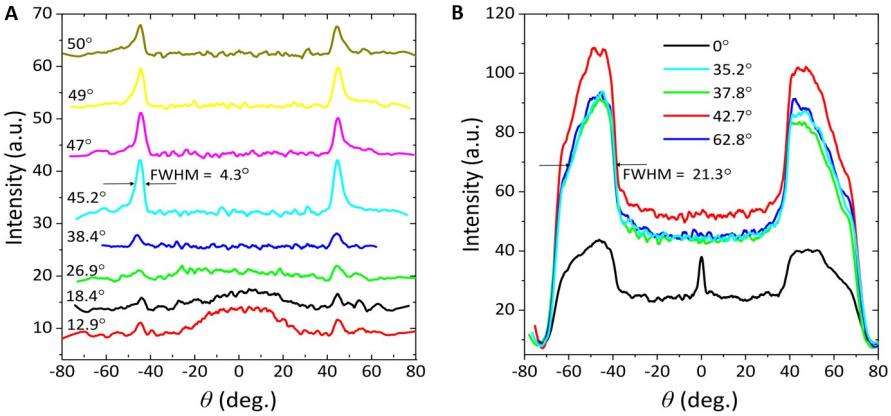

4.5 Fig. Cross-section of BFP images with variable angle excitation configuration: (A) R6G-SPP sample in strong coupling regime; (B) regular fluorescence from R6G molecular dye

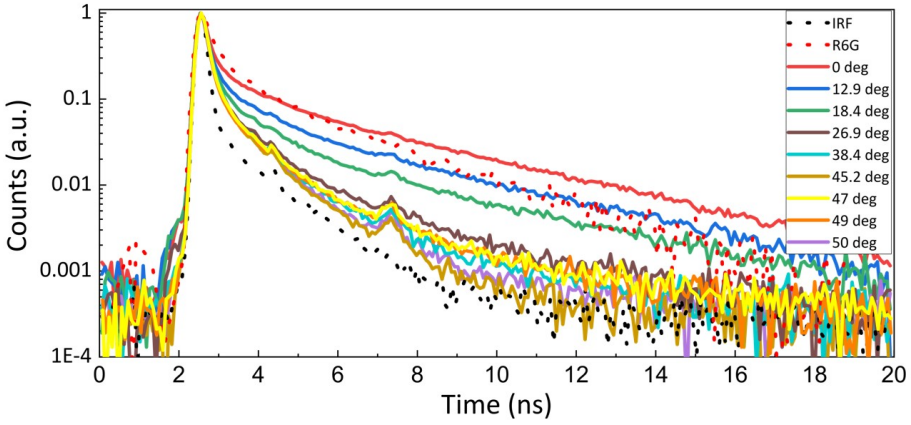

4.6 Fig. Measured fluorescence decay of strongly coupled SPP-R6G structure. Fluorescence decay of regular R6G in PMMA (red dotted curve) and in strong coupling regime with SPP at different excitation angles (solid curves).

Fluorescence lifetime analysis was performed using a TCSPC setup, with different excitation angles. Fluorescence decay was measured for both coupled (CS/Ag/PMMA-R6G) and uncoupled (CS/PMMA-R6G) samples (Fig. 4.6). A convolution between the instrument response function (IRF) and biexpo-

nential function $I(t) = A_1 e^{-t/\tau_1} + (1 - A_1) e^{-t/\tau_2}$ was used and fitted by the least squares method to the measured fluorescence decay data. Closeness of fit was $R^2 = 0.96$. Coefficients A_1 and $(1 - A_1)$ correspond to relative populations of different decay channels within the samples, while τ_1 and τ_2 represent corresponding lifetime values. The fitted model for the uncoupled CS/PMMA-R6G structure showed fluorescence decay lifetime of 0.27 ns. This value is shorter than the expected value of 3-4 ns in water solution, due to interactions with the PMMA matrix [170]. In the strong coupling regime, the lifetime values τ_1 were found to be around 0.16 - 0.17 ns, however the emergence of an additional decay channel τ_2 was around 3.2 - 3.5 ns, which indicated about the presence of a 'slow' decay channel within the structure for excitation angle between 0° and 18.2° (Fig. 4.7). For excitation above 18.4°, the decay occurs mostly through a single decay channel with lifetime τ_1 around 0.14 - 0.16 ns. Moreover, polariton decay at higher excitation angles leads to higher emission intensity, which can be observed in BFP measurements shown in Fig. 4.5A.

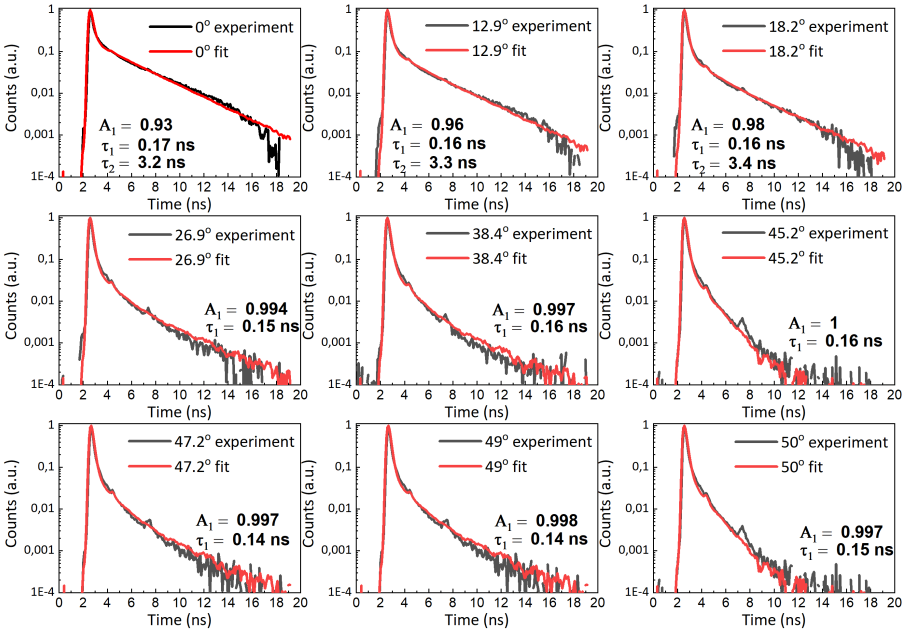

4.7 Fig. Measured fluorescence decay of strongly coupled SPP-R6G structure (black line) and corresponding fitted fluorescence decay profiles (red line) for different excitation angles.

After excitation of plasmon-exciton polariton quasiparticles in a strongly coupled sample, several decay mechanisms to the ground state are at play (Fig. 4.8). It must be noted that during strong coupling, a direct population of the UP state occurs, which is followed by rapid (∼50 fs) non-radiative decay to the LP state [168, 171], therefore, this transition can not be properly observed

using TCSPC technique. Emission from the LP branch can be detected whenever the LP states decay to the ground state (G), depending on the detuning of the cavity mode. Direct population of the ER state is dominant whenever excitation at low AOI is applied, therefore, the non-radiative transition to the LP state is much slower, as compared to UP $\rightarrow$ LP, and is around several hundreds of picoseconds [81]. By changing the excitation angle during the experiments, the excitation conditions of the sample are varied, which results in increased emission intensity as well as changes in polaritonic decay, which can be studied in terms of populations of the excited states and will be discussed in the following section.

4.1.3. Polariton dynamics

Dynamics of the polariton decay are dominated by the transition to the ground state. Depending on the initial population of ER and UP states, the emission can be dominated by the transitions from the ER state to the LP state, rather than from the LP state to the G state, resulting in modified emission characteristics.

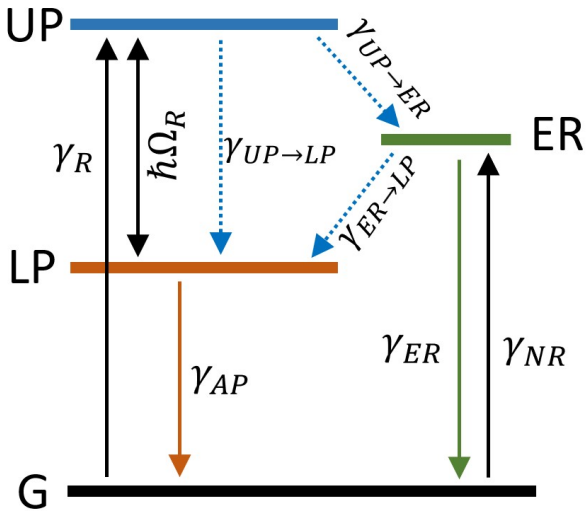

4.8 Fig. Decay of strongly coupled SPP-R6G structure. Energy levels, describing polariton emission and fluorescence decay pathways from upper polariton (UP) and exciton reservoir (ER) states upon resonant and non-resonant excitation.

Internal non-radiative transitions from ER to LP state are depicted as $\gamma_{\mathrm{ER}\rightarrow\mathrm{LP}}$ and from UP to LP as $\gamma_{\mathrm{UP}\rightarrow\mathrm{LP}}$, $\gamma_{\mathrm{UP}\rightarrow\mathrm{ER}}$ correspond to transition

from UP state to ER and the resonant and non-resonant excitation are depicted as γ_R and γ_{NR}, respectively. Analysis of ER contributions to the polariton decay was performed using a rate equation model for different initial populations of ER states. The differential rate equations model can be described as:

$$\frac{dP}{dt} = -\left(\gamma_{\mathrm{UP}\to\mathrm{LP}} + \gamma_{\mathrm{LP}\to\mathrm{G}}\right) P - \gamma_{\mathrm{UP}\to\mathrm{ER}} P, \tag{4.1}$$

$$\frac{dE}{dt} = \gamma_{\mathrm{UP}\to\mathrm{ER}} P - \gamma_{\mathrm{ER}\to\mathrm{G}} E - \left(\gamma_{\mathrm{ER}\to\mathrm{LP}} + \gamma_{\mathrm{LP}\to\mathrm{G}}\right) E, \tag{4.2}$$

where the initial population of the upper polariton state and exciton reservoir is indicated by P and E, respectively. Solution to the equations describes decay to the ground state and gives total emission:

$$I(t) = \left(\gamma_{\mathrm{UP}\to\mathrm{LP}} + \gamma_{\mathrm{LP}\to\mathrm{G}}\right) P(t) + \left(\gamma_{\mathrm{ER}\to\mathrm{LP}} + \gamma_{\mathrm{LP}\to\mathrm{G}}\right) E(t). \tag{4.3}$$

Emission from UP→LP→G transition is described by $\left(\gamma_{\mathrm{UP}\to\mathrm{LP}} + \gamma_{\mathrm{LP}\to\mathrm{G}}\right) P(t)$ and emission from ER→LP→G is described by $\left(\gamma_{\mathrm{ER}\to\mathrm{LP}} + \gamma_{\mathrm{LP}\to\mathrm{G}}\right) E(t)$. Transition ER→G is not considered due to optical filtering of the main R6G emission peak.

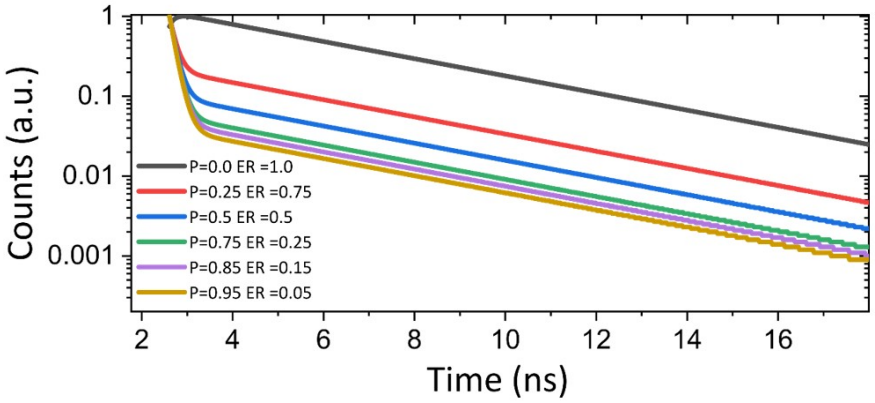

4.9 Fig. Time-dependent emission intensity profile modelled for different initial populations of the excited UP and ER states in the strong coupling regime.

Modelled results show the emission intensity and the fluorescence decay dependence on the initial population of UP and ER state (Fig. 4.9). Initial exciton reservoir population was varied from ER=1 to ER=0.05, showing that longer polariton decay lifetime results from 'slow' transition via ER→LP→G path and is known as polariton bottleneck. Decreasing the ER population results in faster decay, which was observed experimentally, indicating that interactions with the exciton reservoir should be considered even in a strongly

coupled regime.

4.2. **Summary**

Investigation of the dynamical properties of the strongly coupled surface plasmon polariton - molecular exciton state was done using several experimental techniques. Rabi splitting was evaluated using spectroscopic ellipsometry in TIRE configuration, with coupling strength g reaching 200 meV and thus confirming the presence of strong coupling. Photoluminescence measurements detected emission from the lower polariton state in addition to regular R6G molecular dye emission. Moreover, an additional angle-dependent emission peak was observed and attributed to the emission from the LP state in a strongly coupled system. Investigation of photoluminescence properties indicated that a significant part of Rhodamine 6G molecules did not participate in a strong coupling regime with the surface plasmon mode. Fluorescence lifetime measurements showed that as the excitation angle increases toward resonant conditions, the impact of the exciton reservoir on the dynamics of the coupled systems becomes minimal. This suggests that the typical description of plasmonic strong coupling, characterized by the coupled oscillator model, does not capture the full picture, additional decay mechanisms need to be taken into account in order to fully describe systems. Fluorescence lifetime values were observed in the range of hundreds of picoseconds, with the dependence on the excitation conditions. Observed fluorescence decay values were considerably longer than the expected lifetime values for plasmonic excitations, which are on the order of femtoseconds. Therefore, observed values can not be explained without contributions from additional energy levels, such as incoherent transitions from the exciton reservoir state. A solid understanding of the energy exchange processes governing strongly interacting plasmonic systems is important for the development of nanophotonic devices and polaritonic lasers.

5. SPATIOTEMPORAL POLARITON LIFETIME IN BFP MICROSCOPY

Advances in nanophotonics have enabled the development of a wide range of nanoscale optical devices with applications ranging from spectroscopy, imaging, nanolasers to quantum optics and sensing [7, 8, 172–174]. Continuous improvements in optical characterization techniques followed, among which BFP imaging has emerged as a widely used approach. BFP imaging provides a simple and efficient way to obtain the full angular distribution of scattered or emitted light without the need for mechanical goniometers [175] or prism-based setups [176], enabling real-time observation of nanophotonic processes [119]. This capability allows researchers to engineer radiation patterns with high precision, facilitating the design of advanced optical antennas and emitters. This technique is especially valuable when studying plasmonic nanostructures, where light–matter interactions can occur in both weak and strong coupling regimes. However, a key limitation of standard BFP imaging is that it measures only the intensity of light. To address this, several extensions have been developed, incorporating spectral [177, 178], polarization-resolved [177, 179], and phase-resolved detection [123, 180], leading to advanced multidimensional BFP configurations [123, 178, 181, 182]. Among the parameters governing light–matter interactions in nanophotonic systems, the fluorescence lifetime remains one of the most fundamental. Numerous studies have shown that coupling emitters to plasmonic nanostructures can strongly modify their emission rates and spectra [32, 92, 93, 183–185], which is particularly relevant for single-photon sources. These hybrid light–matter states open new opportunities in quantum nanophotonics [10, 20] and molecular photochemistry [22, 53, 186]. Strong coupling occurs when the coupling strength g greatly exceeds the decay rates of the excitonic and plasmonic modes. The resulting polaritonic states represent coherent superpositions of exciton and plasmon modes with distinct dispersive properties [187]. Experimentally, this manifests as a spectral splitting into UP and LP branches [27], separated by the Rabi energy. During strong coupling, coherent energy exchange between exciton and plasmon modes occurs at the Rabi frequency, drastically modifying the effective fluorescence lifetime [58, 188]. The polariton eigenmodes then represent collective excitations that can decay cooperatively (superradiant, shorter lifetime) or destructively (subradiant, longer lifetime), depending on the phase relationship among the coupled emitters. The coherent and collective nature of these states inherently introduces spatial coherence in the emitted light, which directly shapes the angular emission patterns captured in BFP imaging [79, 189]. By extending BFP

imaging to include fluorescence lifetime measurements, one can access a new dimension of information enabling angle-resolved lifetime mapping that reveals the decay dynamics of collective plasmon–exciton polaritons.

In this work, we introduce a modified BFP configuration that combines spatially filtered BFP imaging with time-resolved fluorescence detection. This approach allows selective lifetime measurements from distinct regions of the BFP corresponding to different coupling conditions, thereby constructing a comprehensive angular–lifetime map of the system. We demonstrate the potential of this method using R6G molecules strongly coupled to SPPs, achieving coupling strengths up to 160 meV, and show how this configuration enables wide-field, Fourier-plane lifetime imaging in strongly coupled nanophotonic systems.

The results presented in the following chapter were originally published: Jurkšaitis, P.; Anulytė, J.; Spalinskaitė, E.; Bužavaitė-Vertelienė, E.; Žičkus, V.; Plikusienė, I.; Balevičius, Z. Spatially Filtered Back Focal Plane Imaging for Directional Fluorescence Lifetime Study of Polaritonic States. Photonics 2025, 12, 1165. https://doi.org/10.3390/photonics12121165

The author performed experiments using BFP microscopy and TCSPC. This included system design, alignment, data acquisition, and evaluation of the experimental results. The author suggested and performed new modifications to the existing BFP microscopy setup by the addition of a spatial filtering technique. The author introduced a coupled oscillator model and calculated the coupling strength of the dispersion data. The author wrote the manuscript and made significant contributions to the reviewer comments.

5.1. **Results**

5.1.1. Coupled oscillator model

Excited states dynamics have been observed to be modified in various nanophotonic systems due to coupling to plasmonic modes [190, 191]. However, directly observing Rabi oscillations has been challenging due to transition times of the order of femtoseconds in plasmonic systems and has only been achieved using complicated pump-probe methods [58]. Multilayered nanophotonic structure, consisting of CS/Ag/PMMA-R6G, was experimentally investigated using TIRE setup (Fig. 5.1A). Measured angle θ dependent reflection of p-polarized light from the samples was converted into wavevector k space using the relation $k_{\parallel} = \frac{2\pi}{\lambda} \sin\theta$ and depicted using red squares (Fig. 5.1B). Coupled oscillator model was used to describe strong coupling between SPP and R6G molecular

excitation with Hamiltonian [7]:

$$H(k) = \begin{pmatrix} E_{\mathrm{spp}}(k) & g \\ g & E_{\mathrm{ex}}(k) \end{pmatrix}, \tag{5.1}$$

here $E_{spp}(k)$ and $E_{ex}(k)$ are original uncoupled eigenvalues of SPP and R6G excitations, and g is the coupling strength. New eigenvalues of the coupled state are expressed as:

$$E_{\pm}(k) = \frac{E_{\mathrm{spp}}(k) + E_{\mathrm{ex}}(k)}{2} \pm \frac{1}{2}\sqrt{\left(E_{\mathrm{spp}}(k) - E_{\mathrm{ex}}(k)\right)^2 + 4g^2}. \tag{5.2}$$

Comparison with the uncoupled case showed that a significant modification of the dispersion relations has been achieved, with coupling strength $g = 160$ meV (Fig. 5.1B). Measured dispersion relation of the SPP-R6G sample follows the predicted strongly coupled dispersion with anticrossing at $k_{\|} = 12.5\,\mu\mathrm{m}^{-1}$.

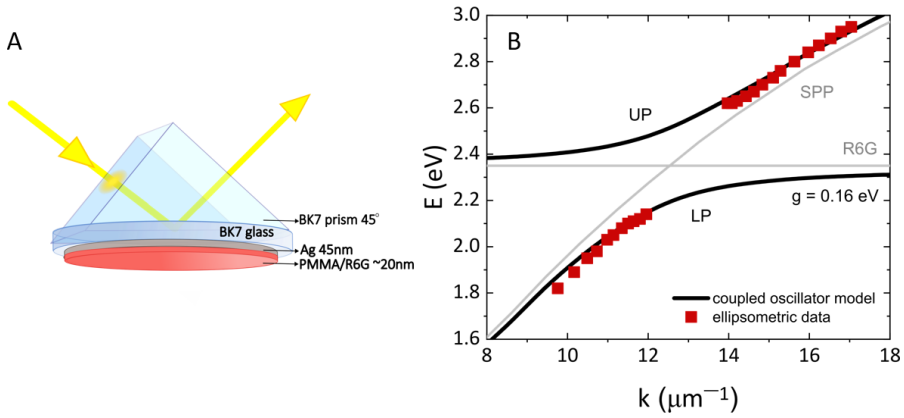

5.1 Fig. Total internal reflection ellipsometry: A) Representation of the measurement setup in TIRE configuration using 45° prism; B) Energy - wavevector dispersion of strongly coupled SPP-R6G. Experimentally measured ellipsometric data is indicated by red squares. Coupled oscillator model with $g = 160$ meV at anticrossing point ($k_{\|} = 12.5\,\mu\mathrm{m}^{-1}$) is shown. Grey lines represent uncoupled SPP and R6G dispersions.

5.1.2. Spatial filtering in BFP

In-house BFP setup was built for investigation of polaritonic emission when excited by laser light (Fig. 5.2). Excitation of the SPP-R6G samples was performed with illumination angle at 0° to observe a significant fraction of uncoupled exciton emission from the ER state. Detuning the laser from the polaritonic re-

sonance state allows population of polaritonic states indirectly through ER and is opposite to the resonant excitation, where polaritonic states are populated directly. The exciton reservoir consists of weakly coupled excitons that remain after laser excitation. Therefore, non-resonant excitation conditions must be met in order to observe weakly and strongly coupled emission simultaneously. Moreover, weakly coupled emission does not exhibit angle-dependent emission properties as does polaritonic emission, therefore, under an appropriate measurement setup, these modes can be angularly resolved.

Photons emitted from the SPP-R6G structure were collected and sent through the first $4f$ imaging system. Images formed at the first Fourier plane (FP1) after L3 were spatially filtered by placing a variable aperture (Thorlabs SM1D12). Placing the aperture on the translation stage, which moves perpendicular to the optical axis, allowed to spatially filter different sections of the BFP images. Wavevector components of the original intensity distribution can be filtered selectively, based on the position and size of the aperture function. Filter signal was then send through a second $4f$ system for fluorescence lifetime and intensity distribution analysis (Fig. 5.2)

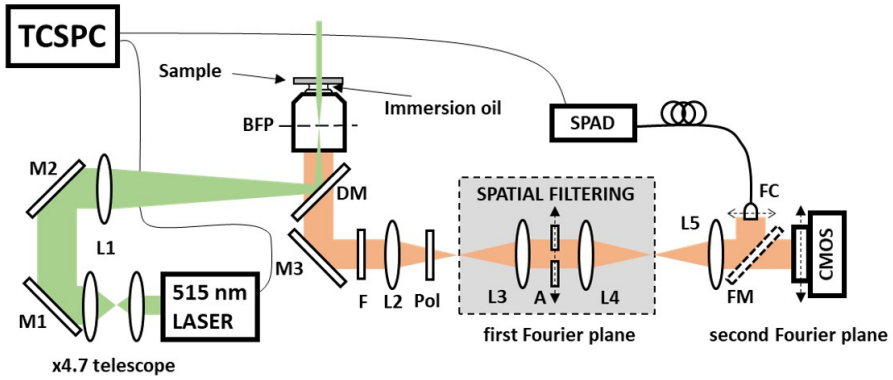

5.2 Fig. Experimental layout of the angle-dependent lifetime measurement setup using spatially filtered back focal plane (BFP) microscopy: mirror (M1-M3), lens (L1-L5), dichroic mirror (DM), long pass filter (F), polarizer (Pol), aperture (A), flip mirror (FM), fiber coupler (FC).

Angle-dependent emission intensity of the R6G fluorescence dye strongly coupled with SPP (Fig. 5.3). Images were taken with polarizer set at two mutually orthogonal directions and the cross-section was taken along the yellow dashed line (Fig. 5.3C). Two main contributors to the emission can be identified as weakly coupled fluorescence and strongly coupled polaritonic emission. Even though the structure permits the excitation of hybrid states, weakly coupled emission is still present due to a significant number of uncoupled excitons remaining in the sample. This weakly coupled emission from the R6G-SPP sample can be identified as a Gaussian distribution in BFP with FHWM of

33.2° (Fig. 5.3C). Sharp peak around 0° in BFP corresponds to laser leakage through the optical filters. Emission observed at angles ±43° with an exponential tail is attributed to polaritonic emission from the hybrid SPP-R6G state. Additionally, confirmation of emission from a polaritonic state is performed by introducing polarizing optics. By changing the polarization direction signal is completely reduced to zero, indicating about linearly polarized light, instead of the random polarization observed from regular R6G fluorescence. This shows that the center part of BFP has a random polarization direction, whereas the outer ring is linearly polarized due to coupling to the SPP mode. Polaritonic states inherit the properties of the radiative mode, which in this case corresponds to a linearly polarized SPP mode.

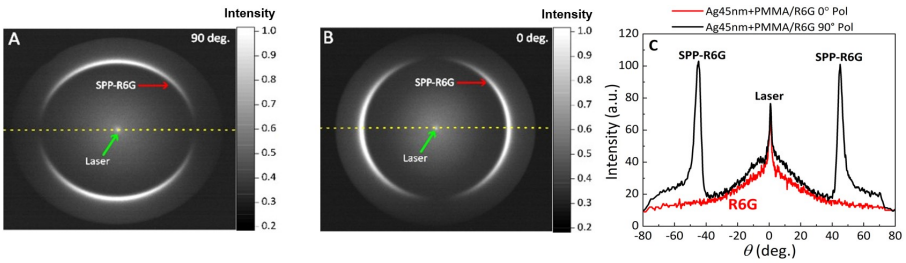

5.3 Fig. Angular emission intensity at the BFP for two orthogonal polarization directions (A, B); C) Cross-sectional view of BFP along the center (yellow dashed line). Laser leakage through the filters corresponds to the sharp peak around 0°.

The intensity ratio between the sharp R6G-SPP peak and the Gaussian curve in the middle indicates about the relative distribution of weakly and strongly coupled states which radiate into the far field. Around 71% of detected fluorescence is due to strong coupling, therefore, different fluorescence dynamics can be expected from different parts of BFP. NA of the microscope objective limits the acceptance angle to 157°. Measurements of filtered BFP were performed by introducing a variable aperture at the 1^{st} Fourier plane (FP1). Aperture allows passing through all wavevectors when open, allowing us to observe the full BFP. However, when partially closed, the aperture acts as a spatial filter in wavevector space, wavevectors falling outside the aperture are attenuated, thus allowing to filter BFP. Aperture set at minimal permittable size with radius of 0.5 mm transmits only 24° of angles. This allows to distinguish BFP into five separate sections by varying the position of the aperture along the axis perpendicular to the optical axis. Resolution is limited by the relatively large size of the aperture, however, more information can be gained by introducing additional scanning direction, such as shifting the aperture vertically as well as laterally along the BFP. This would allow to obtain an array of $n * m$ BFP sections, where n is the number of lateral sections and m is the number of

vertical positions. It should be noted that due to the relatively large size of aperture (0.5 mm), features narrower than 24° can not be distinguished, from a fluorescence lifetime point of view. This is due to the fact that the collected light from within this range is collected simultaneously and the response of the detected signal is a mixture. However, intensity profiles corresponding to the SPP-R6G emission ring exhibit narrow angular emission (4.8°) and indicate that the measured signal at positions (1) and (5) is from emission angles narrower than the FWHM of the aperture.

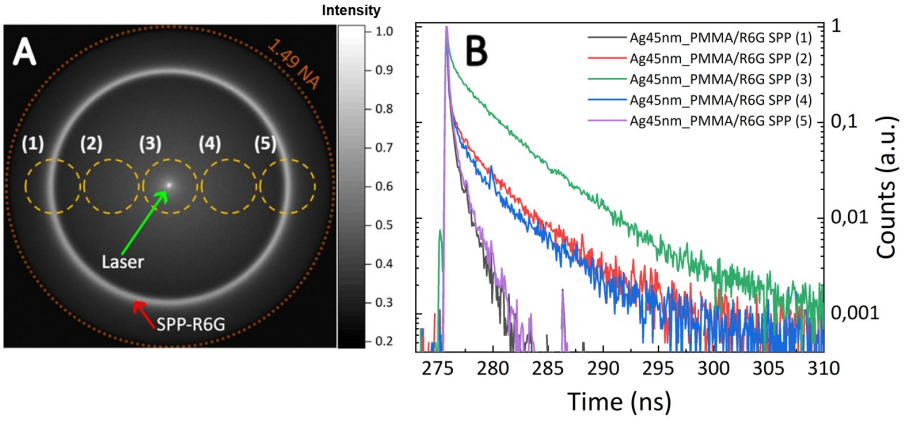

5.4 Fig. Fluorescence lifetime investigation of spatially filtered BFP: A) BFP image of strongly coupled SPP-R6G. Five sections were filtered with spatial filter (yellow dashed circles). Maximum acceptance angle of the microscope objective was limited by NA = 1.49 (red dashed circle); B) Fluorescence lifetime measurements were performed for each section of the spatially filtered BFP image.

Distinct fluorescence lifetimes can be observed from different sections (1) to (5) of BFP (Fig. 5.13). Exact evaluation of fluorescence lifetime is performed by convolving a biexponential function:

$$I(t) = A_1 e^{-(t/\tau_1)} + (1 - A_1)\, e^{-(t/\tau_2)} \tag{5.3}$$

with Instrument Response Function (IRF). Here τ_1 and τ_2 correspond to lifetime values of emitter species. Coefficients A_1 and $A_2 = 1 - A_1$ are relative populations of emitters in close proximity to the metallic layer and further away from the layer, respectively. The convolved function was then fitted to the measured signal using the least squares method (Fig. 5.5). Center(3) of the BFP exhibits slowest decay rate with $\tau_1 = (0.183 \pm 0.001)\ ns$ and $\tau_2 = (2.92 \pm 0.068)\ ns$ and relative amplitude $A_1 = 0.786$ and $A_2 = 0.214$. This emission is collected from the whole thickness of the R6G/PMMA layer. Even though the laser leakage through the optical filters is evident at the centre part, the influence on the me-

asured lifetime is negligible. Laser excitation was performed with femtosecond laser pulses (214 fs), whereas the expected IRF is $\sim 100\ ps$. Emission at higher angles, when detecting from positions (2) and (4), exhibited faster radiative decay with lifetime values $\tau_1 = (0.106 \pm 0.001)\ ns$, $\tau_2 = (2.494 \pm 0.081)\ ns$ and coefficients $A_1 = 0.969$, $A_2 = 0.031$. Shorter lifetime values of τ_1 at positions (2) and (4), along with increased A_1 from ~ 0.79 to ~ 0.97 signal about the increased quenching at the surface [14]. Moreover, the observed difference between lifetime values could indicate changes in the emitter's population. Similarly, different emission dynamics from positions (3) and (2),(4) could result from the interference of emitted and reflected light from the interface, even without the presence of SPP mode [7].

The most radical modification to the excited state dynamics is observed at positions (1) and (5). The signal measured from the strongly coupled SPP-R6G sample at positions (1) and (5) is dominated by the IRF, indicating that true lifetime values can not be properly measured. Previous observations have indicated about faster radiative transitions due to interactions with the metal layer [7]. However, the angular intensity pattern at the BFP is highly dependent on the plasmonic structure. The expected lifetime of SPP excitation is in the femtosecond timescale, however polaritonic state can increase the observed lifetime to values closer to typical R6G emission rates. Other mechanisms, such as the polariton bottleneck effect, can increase the observed lifetime values due to slow relaxation from ER states. The observed lifetime at positions (1) and (5) should be taken with care, due to limitations set by the IRF of the measurement system. A more appropriate experimental setup, such as pump-probe, should be used for the investigation of fluorescence on the femtosecond timescale [58].

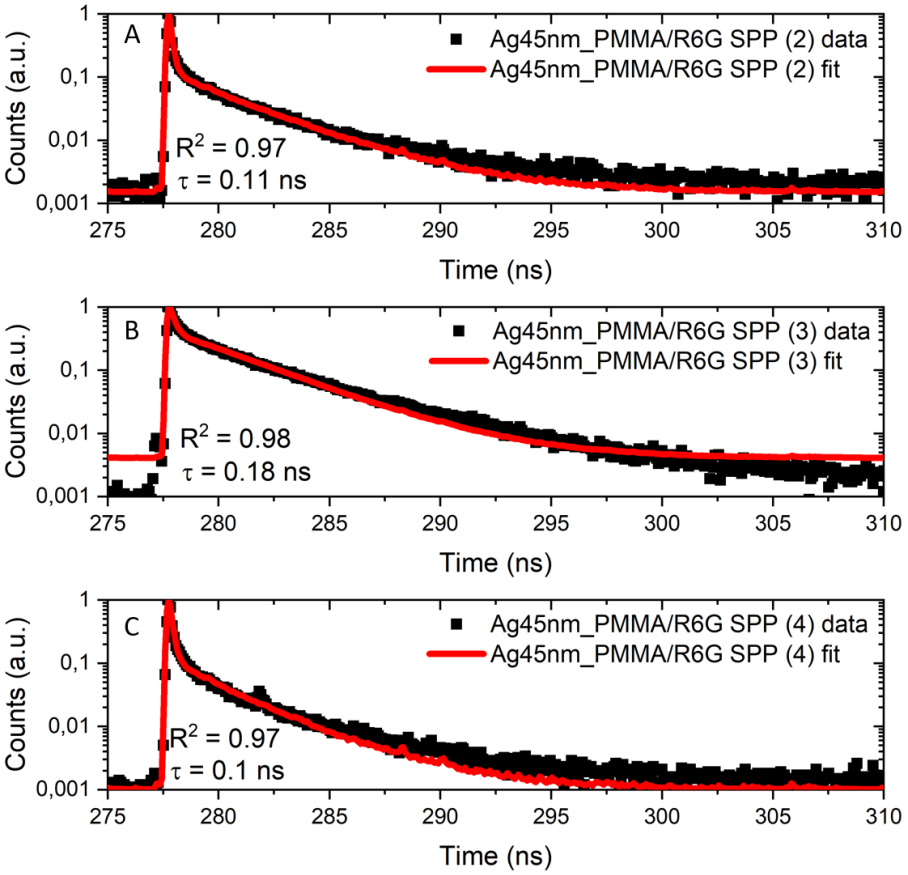

5.5 Fig. Fluorescence lifetime retrieval of measured decay data using deconvolution algorithm for different BFP sections: A) section (2); B) section (3); C) section (4). R^2 around 0.97.

5.2. **Summary**

Angle-dependent fluorescence lifetime measurements have been conducted for SPP-R6G samples under strong coupling. A two-layer structure consisting of a uniform silver layer and R6G molecular dye was examined, and TIRE measurements were performed. Strong coupling was achieved and evaluated using a coupled oscillator model, which showed coupling strength g reaching up to 160 meV. A microscopy setup was used for the investigation of emission properties in BFP. Additionally, spatial filtering was used for angular separation and investigation of fluorescence dynamics in BFP. It was concluded that intensity distribution in BFP originates as a mixture of different fluorescent lifetime values, which indicate about distinct decay pathways for different BFP sections. This is in contrast with typical FLIM experiments performed in real space. The proposed method is verified using SPP-R6G samples. Fast transition rates at

positions (1) and (5) result from strong coupling dynamics, however observed signal is dominated by IRF. Lifetime of 0.1 ns is observed at positions (2) and (4) and 0.18 ns at position (3), indicating about emission angle-dependent fluorescence decay pathways. Fourier plane lifetime measurement techniques could potentially complement existing FLIM techniques. Also, this suggests the possibility to distinguish between weakly and strongly coupled states in nanophotonic devices.

CONCLUSIONS

- The optical response and dispersion relations were investigated using the effective media Bruggemann approximation for non-labeled and labeled protein dye complex coupled with uniform gold film with a thickness of 45 nm. The observed normal mode splitting indicated a strong coupling regime in HSA protein molecules, with Rabi splitting dependent on the initial concentration of A633 molecular dye.

- Analysis of the Rabi splitting in strongly coupled labelled HSA protein complex showed that splitting Ω_R is dependent on the adsorbed protein mass on the gold surface, with average concentration of participating protein molecules in $\sim 10^{23}\ m^{-3}$ range. A parabolic relationship between Rabi splitting and the number of participating particles can be approximated linearly within a narrow coupling range of around 60 meV.

- Reverse-Kretschmann configuration was used to excite and collect the emission of SPP-R6G nanophotonic structure. Emitted light was collected at angles between $40° - 50°$ under non-resonant excitation. Dispersion of the light followed the LP branch measured by TIRE, thus demonstrating emission from strongly coupled polaritonic states.

- Fluorescence lifetime measurements were performed under variable-angle excitation in a BFP microscopy setup. Polaritonic state lifetime was observed to depend on the initial excitation conditions, with the influence from the exciton reservoir observed to be when using $\leq 18.2°$ excitation. Increasing the excitation angle above 18.2° results in the increased population of the UP component of the polaritonic states.

- A simple rate equation model was suggested and calculated to explain the observed lifetime behaviour. Numerical model, which includes additional transitions with exciton reservoir state, showed consistent results with the measured lifetime data, indicating the modified polariton lifetime under non-resonant excitation occurring due to slow internal transitions from the ER to the LP state.

- Coupled oscillator model was used to evaluate coupling strength g from TIRE data. The numerically calculated dispersion relation was consistent with measurements and showed that the coupling strength between SPP and R6G was around 160 meV.

- A method of measuring angle-dependent fluorescence lifetime in BFP microscopy was proposed. A spatial filtering technique was used to selectively filter out different emission angles compatible with the BFP

microscopy setup. This experiment showed that the shortest fluorescent lifetime was observed from the SPP emission ring at $\pm 43^{\circ}$ due to strong coupling dynamics, while the longest lifetime was at around 0° and was attributed to weakly coupled R6G molecules.

SANTRAUKA

Šviesos tyrimai dažniausiai apima tokius reiškinius kaip interferencija, difrakcija, bangų sklidimas ir pan. Šie reiškiniai priskiriami optikos sričiai, kuri nagrinėja šviesą kaip klasikinių elektromagnetinių bangų sklidimą tolimajame lauke ($d >> \lambda$). Praktinis šių optinių reiškinių taikymas leido sukurti tokius įrankius kaip lazeriai, mikroskopai, šviesolaidžiai ir kt. Šie efektai dažniausiai tiriami makroskopinėje skalėje, t. y. kai erdviniai matmenys yra daug didesni už atitinkamos šviesos bangos ilgį [1]. Tai nėra atsitiktinumas, nes tolimojo lauko optika yra apribota difrakcijos, kuri draudžia šviesos lokalizaciją žemiau tam tikros ribos. Ši riba vadinama Abės difrakcijos riba ir aprašoma kaip $\lambda/2NA$ [2]. Matomoje srityje ši riba yra maždaug 200–300 nanometrų. Ilgą laiką Abės kriterijus buvo laikomas fundamentalia riba, tačiau 1970–1980 m. eksperimentiškai buvo parodyta, kad difrakcijos ribą galima apeiti pasinaudojant gestančiomis bangomis, kurios egzistuoja artimojo lauko srityje [3–6]. Atsiradus nanotechnologijoms pradėjo formuotis nauja sritis – nanofotonika, kurios tikslas yra ieškoti naujų būdų valdyti šviesą nanoskalėje. Naujos medžiagos, struktūros ir konfigūracijos suteikė galimybę lokalizuoti elektromagnetinius laukus iki sub-banginių matmenų, atverdamos kelius naujų fizinių reiškinių stebėjimui tiek fundamentiniu, tiek taikomuoju požiūriu [7, 8]. Nanofotoninių įrenginių matmenys paprastai yra nuo 1 iki 1000 nm. Tokiuose masteliuose tolimojo lauko aproksimacijos nebegalioja – kvantiniai ir artimojo lauko efektai tampa itin svarbūs. Populiariausi nanofotonikos prietaisai apima dielektrines nanostruktūras, plazmoniką, fotoninius kristalus ir dvimačius (2D) sluoksnius [9–11]. Dielektriniai ir fotoninių kristalų įrenginiai paprastai pasižymi mažais optiniais nuostoliais ir dideliais kokybės (Q) koeficientais, palyginti su kitomis sistemomis, tačiau jos taip pat pasižymi santykinai silpna sąveika su medžiaga. Plazmoninės nanostruktūros leidžia pasiekti itin didelį elektromagnetinio lauko lokalizavimą ($< \lambda/10$) ir lauko stiprinimą, todėl sąveika su medžiaga tampa labai stipri. Kita vertus, dėl elektronų susidūrimų plazmoninėse struktūrose atsiranda dideli nuostoliai.

Elektromagnetinių laukų lokalizavimas iki sub-banginių matmenų leido stebėti naujus fizinius reiškinius, susijusius su šviesos ir medžiagos sąveika [12,13]. Gerai žinomas šviesos ir medžiagos sąveikos pavyzdys, kai spinduolis – pavyzdžiui, fluorescuojanti dažo molekulė ar kvantinis taškas – yra patalpintas į nanofotoninę aplinką [14]. Tokia spinduolio ir nanofotoninės struktūros sąveika keičia optinių būsenų tankį, todėl gali būti stebimas spontaninės emisijos slopinimas arba sustiprinimas, pirmą kartą prognozuotas Purcell'io dar 1946 m. [15]. Šis reiškinys vadinamas silpnosios sąveikos (angl. weak coupling) režimu. Dar radikalesni būsenos modifikavimai atsiranda, kai sąveikos stipris tarp spinduolio ir nanofotoninės struktūros viršija atskirų sistemų nuostolius

($g >> \kappa, \omega$). Tokiu atveju įvyksta rezonatoriaus ir spinduolio būsenų hibridizacija, kurios metu susidaro naujos poliaritoninės būsenos – tai vadinama stipriosios sąveikos (angl. strong coupling) režimu [13,16]. Apart didelės nanofotoninių struktūrų įvairovės tyrimuose, taip pat yra ir didelis įvairių spinduolių pasirinkimas, apimantis organines dažo molekules, kvantinius taškus, defektus kristalinėse gardelėse, pavienes molekules ir atomus. Šių spinduolių integravimas į nanofotonines sistemas leidžia ieškoti naujų taikymų tokiose srityse kaip ultragreita nanofotonika, vieno fotono šaltiniai ir biologija [17,18,20–24].

Ši disertacija skirta stipriosios sąveikos režimo tyrimams plazmoninėse nanostruktūrose, naudojant fluorescuojančių dažų molekules ir tiriant jų taikymus nanofotoniniuose įrenginiuose bei optiniuose jutikliuose. Poliaritoninių būsenų stipriosios sąveikos režime tyrimai buvo atlikti naudojant nanostruktūras su ištisiniu sidabro arba aukso sluoksniu bei Rodaminas 6G arba Alexa633 molekuliniais dažais.

Disertacijos pirmoje dalyje buvo tiriamos žmogaus serumo albumino (angl. HSA) baltymo molekulės, pažymėtos fluorescuojančiais dažais ir jų sąveika su 45 nm storio ištisiniais aukso sluoksniais. Optinis atsakas stipriosios sąveikos režime buvo modeliuojamas efektyvios Bruggemano aproksimacijos metodu. Modeliavimas parodė, kad sąveikos stiprumas proporcingas molekulių koncentracijai ant aukso paviršiaus, todėl leidžia įvertinti žymėtų baltymų masę, adsorbuotą ant plazmoninio jutiklio, naudojant optinį atsaką TIRE konfigūracijoje.

Kita disertacijos dalis skirta poliaritonų gyvavimo trukmės dinamikos tyrimui. Poliaritonai buvo tiriami naudojant laike koreliuotų pavienių fotonų skaičiavimo metodą (angl. TCSPC). Eksperimentai atliekami naudojant paviršinių plazmonų poliaritonų (angl. SPP) būsenas, susidarančias ištisiniuose sidabro sluoksniuose ant stiklo padėklų, sąveikaujančias su Rodamino 6G dažo molekulėmis. Elipsometrijos matavimai patvirtino stipriosios sąveikos režimą, kurio sąveikos stiprumas siekė apie 200 meV. Visiško vidaus atspindžio fluorescencijos metodas (angl. TIRF) buvo naudojamas eksitonų rezervuaro būsenų sužadinimui galinio židinio plokštumos (angl. BFP) mikroskopijoje, siekiant įvertinti dinaminius mechanizmus, lemiančius poliaritonų sąveikas. Šis tyrimas papildė esamas žinias apie sąveikos dinamiką plazmoninėse–eksitoninėse sistemose.

Paskutinėje disertacijos dalyje nagrinėjamos stipriosios sąveikos SPP–R6G būsenos ir jų fluorescencijos gyvavimo trukmių kampinės charakteristikos. Normaliųjų modų skilimas, stebėtas naudojant visiško vidinio atspindžio elipsometriją, buvo sumodeliuotas naudojant surištų osciliatorių modelį, su sąveikos stiprumu lygiu $g = 160$ meV. Pasiūlytas modifikuotas BFP vaizdinimo metodas, naudojantis erdvinio filtravimo techniką Furjė plokštumoje, leidžia tirti nuo krypties priklausomą poliaritonų gesimo dinamiką. Šiame darbe pristatytas metodas pasiūlė naują būdą kampinei informacijai gauti BFP mikroskopijos sistemoje ir yra itin svarbu nanofotoninių įrenginių charakterizavimui bei kū-

rimui.

Tikslai

- Ištirti SPP ir žymėtų baltymo (HSA) molekulių elgseną stipriosios sąveikos režime, daugiausia dėmesio skiriant modifikuotoms optinėms savybėms ir pritaikymui optiniams biojutikliams.
- Ištirti eksitonų rezervuaro įtaką poliaritonų gesimo dinamikai esant stipriai SPP–Rodamino 6G sąveikai, prie skirtingų žadinimo parametrų.
- Ištirti kampinę poliaritoninę emisiją stipriai susietose SPP–Rodamino 6G būsenose, naudojant erdviškai filtruotą BFP matavimo metodą.

Uždaviniai

- Ištirti žymėtų ir nežymėtų HSA molekulių, patalpintų ant aukso nanodangos artimojo lauko srityje, optinį atsaką, naudojant skaitmeniškai sumodeliuotą dispersiją.
- Išanalizuoti optinę dispersiją bei Rabi tarpą esant stipriosios sąveikos režimui tarp SPP ir HSA molekulių bei ištirti priklausomybę nuo molekulių koncentracijos.
- Įvertinti stipriąją sąveiką tarp SPP ir Rodamino 6G molekulių ir stebėti poliaritoninę emisiją esant nerezonansinėms sužadinimo sąlygoms.
- Ištirti SPP–R6G hibridinių būsenų fluorescencijos gyvavimo trukmės gesimo dinamiką, taikant kintamo kampo žadinimo ir fluorescencijos detekcijos schemas.
- Analizuoti poliaritonų gesimo dinamiką, naudojant matematinius modelius ir ištirti eksitonų rezervuaro būsenų įtaką.
- Ištirti SPP–R6G stipriąją sąveiką naudojant surištų osciliatorių modelį ir įvertinti sąveikos stiprį iš TIRE elipsometrijos duomenų.
- Pritaikyti optinio erdvinio filtravimo metodiką fluorescencinės mikroskopijos sistemai ir gauti nuo emisijos kampo priklausančias poliaritonų gyvavimo trukmės charakteristikas.

Ginamieji teiginiai

- Rabi tarpo atsiradimas stipriosios sąveikos režime tarp žymėtų baltymo eksitonų ir plazmoninio sužadinimo leidžia nustatyti baltymo koncentraciją pagal sąveikos stiprio pokyčius.

- Eksitonų indėlį į koherentinį energijos mainų procesą hibridinėje poliaritoninėje būsenoje galima valdyti keičiant poliaritonų sužadinimo sąlygas.

- Erdvinis filtravimas galinėje židinio plokštumoje suteikia nuo kampo priklausančią laikinę informaciją, leidžiančią išskirti silpnosios ir stipriosios sąveikos režimus plazmonų–eksitonų pagrindu susidarančioms poliaritoninėms būsenoms.

Mokslinis naujumas

Šio tyrimo naujumas slypi kombinuotame fluorescencijos intensyvumo matavime galinėje židinio plokštumoje kartu su fluorescencijos gyvavimo trukmės gesimu esant rezonansinėms ir nerezonansinėms žadinimo sąlygoms. Toks metodas leidžia ištirti eksitonų rezervuaro įtaką poliaritonų gesimo trukmei naudojant Rodamino 6G dažo molekules. Išmatuotos fluorescencijos gyvavimo trukmės, siekiančios šimtus pikosekundžių, yra gerokai ilgesnės nei femtosekundžių trukmės, kurios paprastai tikėtinos plazmoninės stiprios sąveikos režimuose. Šis neatitikimas rodo, kad įprastinis surištų osciliatorių modelis nepilnai aprašo koherentinio energijos mainų dinamiką ir kad būtina įtraukti papildomus nekoherentinius sąveikos mechanizmus, tokius kaip perėjimai iš eksitonų rezervuaro į žemesniąją poliaritono šaką. Ši įžvalga suteikia gilesnį supratimą apie šviesos ir medžiagos sąveiką stipriosios sąveikos režime ir yra svarbi kuriant kvantinės nanoptikos įrenginius, poliaritoninius lazerius bei poliaritonų kondensatus.

Naujausi nanofotonikos pasiekimai sudarė sąlygas proveržiams spektroskopijoje, vaizdinime, kvantinėje optikoje ir jutikliuose. Šiuose tyrimuose itin svarbų vaidmenį atlieka pažangios optinės charakterizavimo technikos, tarp kurių galinio židinio plokštumos vaizdinimas tapo nepakeičiamu įrankiu. Šiame darbe pristatome fluorescencijos gyvavimo trukmei jautrų BFP vaizdinimo metodą, kuris reikšmingai praplečia įprastą Furjė plokštumos metodologiją. Įdiegus erdvinį filtravimą laike koreliuotų pavienių fotonų detekcijos schemoje, galima išanalizuoti nuo kampo priklausančias fluorescencijos gyvavimo trukmes, taip sudarant galimybę susieti kampinę emisiją su poliaritonų gyvavimo trukme mikroskopijos konfigūracijoje. Derinant gyvavimo trukmės ir intensyvumo informaciją, galima tiesiogiai įvertinti spindulinės energijos pernašos priklausomybę nuo emisijos kampo. Šis metodas suteikia naują eksperimentinį metodą BFP vaizdinimui, sujungdamas k-erdvės emisijos analizę su laiko skyros fotofizika ir atverdamas galimybes tirti hibridinių nanofotoninių sistemų laikinę dinamiką bei kolektyvines kvantines būsenas.

Praktinė vertė

Šio darbo praktinė vertė slypi naujų eksperimentinių priemonių ir įžvalgų suteikime, skirtame naujos kartos nanofotoninių ir biosensorinių prietaisų kūrimui. Pademonstravus nuo kampo jautrios fluorescencijos gyvavimo trukmės vaizdinimą Furjė erdvėje, pristatomas galingas metodas emisijos dinamikai tirti su kampine raiška. Tai suteikia tyrėjams galimybę išgauti informaciją apie silpnai ir stipriai susietas būsenas, suderinamas su esamais BFP mikroskopijos metodais, ir pasiūlyti išsamesnį šviesos bei medžiagos sąveikos vaizdą. Tokia galimybė ypač svarbi optimizuojant plazmoninius jutiklius, optinius filtrus ir prietaisus, kuriuose esminį vaidmenį atlieka kryptingumas ir režimų selektyvumas.

Be to, mūsų pastebėtas eksitonų rezervuaro indėlis į poliaritonų gyvavimo trukmes pabrėžia nekoherentinių skilimo kanalų svarbą stipriai sąveikaujančiose sistemose. Šis supratimas turi praktinių pasekmių kuriant ilgesnės gyvavimo trukmės poliaritonines būsenas, galinčias pagerinti stabilumą ir efektyvumą tokių prietaisų kaip: poliaritoniniai lazeriai, kvantinių šviesos šaltiniai ar nanoskalės optiniai jungikliai. Be to, šis darbas gali prisidėti prie pažangių biojutiklių technologijų, kurios remiasi sąveikos stiprio pokyčiais molekuliniams ryšiams aptikti, plėtros. Šios įžvalgos sujungia fundamentinę fiziką su taikomaisiais tyrimais, atverdamos kelią inovatyvioms technologijoms kvantinės nanofotonikos, kvantinės optikos ir pažangių biomedicininių jutiklių srityse.

Autoriaus indėlis

Stipriai sąveikaujančių HSA molekulių optinio atsako skaitmeninę simuliaciją ir duomenų analizę autorius atliko konsultuodamasis su darbo vadovu ir bendraautoriais. Autorius atliko laike koreliuotų pavienių fotonų skaičiavimo ir BFP vaizdinimo eksperimentus, įskaitant optinių sistemos dizainą, surinkimą ir derinimą. Autorius pasiūlė erdvinio filtravimo BFP metodiką, atliko idėjos eksperimentinį įgyvendinimą. Autorius pritaikė surištų osciliatorių modelį sąveikos stiprio nustatymui. Taip pat dalyvavo kampui jautrios poliaritonų emisijos spektrų detekcijoje ir matavimuose. Poliaritono fluorescencijos dinamikos interpretaciją ir matematinę analizę atliko autorius. Visus pirminius publikacijų rankraščius autorius parengė konsultuodamasis su darbo vadovu ir bendraautoriais. Autorius taip pat reikšmingai prisidėjo prie recenzentų pastabų įgyvendinimo.

Literatūros apžvalga

Šis skyrius apims trumpą literatūros apžvalgą, pateiktą 1-ajame disertacijos skyriuje. Bus apibendrinamos temos apie paviršinius plazmonus poliaritonus, plazmoninę emisiją, stipriąją sąveiką bei stipriosios sąveikos laikines charakte-

ristikas.

Nanofotonika tiria elektromagnetinio lauko modų sąveiką su įvairiomis nanostruktūromis. Sritis, nagrinėjanti šviesos sąveiką su metalais, vadinama plazmonika arba nanoplazmonika. Šias sąveikas metaluose daugiausia lemia laisvieji elektronai esantys laidumo juostoje. Drudės modelis, aprašantis elektrines ir šilumines metalo savybes, rodo, kad elektronai metale osciliuoja 180° priešfazėje lyginant su krentančiu elektromagnetiniu lauku. Dėl šios priežasties dauguma metalų pasižymi labai dideliu atspindžiu optinių dažnių diapazone. Laisvieji elektronai metale gali palaikyti krūvio tankio osciliacijas, kurios sukuria rezonansines būsenas optiniuose dažniuose. Šios būsenos paprastai vadinamos plazmonais ir yra apibūdinamos plazmos dažniu. Taurieji metalai, tokie kaip auksas ir sidabras, pasižymi dielektrine funkcija, kuri optiniuose dažniuose yra neigiama ir suteikia jiems savitą išvaizdą. Paviršiniai plazmonai metale atsiranda sužadinus plazmonus išoriniu elektromagnetiniu lauku krentančiu rezonansiniais kampais, vadinamais SPR kampais [25]. Elektromagnetinė banga sąveikauja su laisvųjų krūvininkų osciliacijomis metalo sandūroje, sudarydama paviršinį plazmono poliaritoną optinių arba infraraudonųjų dažnių srityje. Paviršinis plazmonas lokalizuoja krentančią elektromagnetinę bangą iki nanometrinių matmenų, todėl plazmoninės struktūros yra itin svarbios kuriant koherentinius nanometrų dydžio šviesos šaltinius. Skirtingai nei klasikinės optinės bangos, dėl saveikos su elektronais, SPP pasižymi medžiagai būdingomis savybėmis, tokiomis kaip efektyvioji masė ir didelė lokalizacija, leidžiantis šviesą sutelkti bei skleisti nanometrų masteliu ir apeiti Abe difrakcijos ribą. Tai leidžia pasiekti didelį optinio lauko lokalizavimą ir energijos tankį ties metalo paviršiumi [14]. Naudojant įvairias metalines nanostruktūras, tokias kaip reljefiniai paviršiai ar nanodalelės, galima valdyti sužadinimo rezonanso sąlygas, todėl tokios struktūros tampa patrauklios optiniams jutikliams [26]. SPP gebėjimas pasiekti didelį elektromagnetinio lauko tankį yra itin svarbus, nes tai leidžia sudaryti sąlygas stipriai šviesos ir medžiagos sąveikai artimojo lauko srityje [7, 27]. Lokalus lauko sustiprinimas jau buvo naudojamas fluorescencijos sustiprinimui [14, 28], plazmoniniams lazeriams [29, 30] ir Raman'o efekto stiprinimui [31]. Kiti sužadinimo metodai apima Otto konfigūraciją, artimojo lauko zondus [33, 34], pavienius fotonus [35], lokalizuotus optinius artimojo lauko režimus [36], fluorescuojančias molekules [37]. Šių metodų pagalba paviršiaus plazmonai gali būti tiesiogiai sužadinami nenaudojant prizmės. Artimojo lauko sužadinimas, pavyzdžiui, sužadinimas naudojant fluorescencijos dažų molekules, yra ypač svarbus stipriosios sąveikos kontekste, kadangi sąveikos stipris priklauso nuo atstumo tarp šviesą skleidžiančių molekulių ir SPP. Tai daugiausia lemia tai, kad elektrinio lauko amplitudė eksponentiškai slopsta į aplinką, prasiskverbdamos tik apie $\sim$ 30 nm į metalą. Toks erdvinis lokalizavimas metalo paviršiuje sukelia lauko sustiprinimą, kuris padeda pasiekti stipriąją sąveiką net ir stipriai slopinančioje metalinėje aplinkoje. Didžiausias

plazmoninių nanostruktūrų trūkumas yra dideli nuostoliai metaluose, kurie riboja SPP sklidimo ilgį. Apskaičiuota, kad sklidimo ilgis yra maždaug ~ 60 µm sidabrui ir ~ 10 µm auksui [8]. Ilgesni sklidimo atstumai gali būti pasiekti naudojant lokalizuotą paviršiaus plazmono rezonansą, pavyzdžiui metalo nanosalelėse, kuris leidžia pasiekti iki kelių centimetrų atstumus [13]. Dėl vidinių nuostolių SPP metaluose paprastai pasižymi mažu Q faktoriumi, dažniausiai 5 – 100 ribose. Vis dėlto mažas modos tūris ir didelis energijos tankis leidžia efektyviai palaikyti sąveiką su plazmoniniu sužadinimu.

Fluorescencijos detekcijos metodai sparčiai plinta biologijos, biotechnologijų ir medicinos srityse. Fluorescencija leido pasiekti daug reikšmingų proveržių jutikliuose, medicininėje diagnostikoje ir genų tyrimuose [14, 46, 47]. Atsitiktinai pasiskirstę sužadinti fluoroforai paprastai pasižymi beveik izotropine emisija laisvoje erdvėje, todėl signalo surinkimo efektyvumas dažniausiai yra labai mažas (mažiau nei 1%) [32]. Naujausi nanofotonikos pasiekimai leido išplėsti detekcijos efektyvumą iki 50 % naudojant plazmoninius bandinius, taip padidinant jautrumą. Esant stipriajai sąveikai, poliaritoninės būsenos suyra nespindulinės arba spindulinės emisijos būdu. Dėl plazmonams būdingų savybių poliaritoninės būsenos pasižymi SPCE emisijos charakteristikomis, kurios paprastai stebimos naudojant plazmoninėmis medžiagomis pagrįstus mėginius. SPCE emisija yra stipriai poliarizuota ir pasižymi tiksliai apibrėžta spinduliuotės kryptimi. SPCE reiškinys yra glaudžiai susijęs su SPR, tačiau pagrindinis skirtumas slypi dalyvaujančiuose laukose. SPP atsiranda dėl krentančios elektromagnetinės bangos sąveikos su paviršiniu plazmonu, tuo tarpu SPCE atveju sąveika vyksta tarp sužadintų fluoroforų ir paviršinių plazmonų.

Stiprioji sąveika yra reiškinys, kai elektromagnetinis laukas ir medžiagos sužadinta būsena (pvz., eksitonas – sužadinta elektrono ir skylės pora molekulėje ar puslaidininkyje) pradeda koherentiniu būdu keistis energija greičiau, nei ją praranda dėl spinduliavimo ar sugerties procesų. Tokiu atveju šviesa ir medžiaga nustoja būti atskiri reiškiniai – jie susilieja į hibridines šviesos–medžiagos būsenas, vadinamas poliaritonų būsenomis. Šis reiškinys pasireiškia, kai sąveikos stipris g tampa didesnis už abiejų komponentų nuostolius $g << \kappa, \omega$. Spektriniuose matavimuose tai pasireiškia Rabi skilimu (Rabi tarpu) – optinės dispersija skyla į dvi šakas: viršutinę (UP) ir apatinę (LP) poliaritonų būsenas. Stiprioji sąveika gali būti stebima, pavyzdžiui, kai organiniai dažai, puslaidininkiniai kvantiniai taškai ar 2D medžiagos sąveikauja su optiniais rezonatoriais, mikroertmėmis ar paviršiaus plazmonais. Dėl šių hibridinių būsenų susiformavimo keičiasi spinduliavimo savybės, fluorescencijos trukmė, energijos pernaša ir net cheminių reakcijų kinetika. Todėl stiprioji sąveika tampa itin svarbiu reiškiniu kvantinės optikos, nanofotonikos ir molekulinės kvantinės chemijos tyrimuose, atveriančiu kelią šviesos valdymui kvantiniu lygmeniu. Didelė dalis šiuolaikinių plazmoninių stipriosios sąveikos tyrimų daugiausia dėmesio skiria išspinduliuotos šviesos koherentinėms savybėms [57, 88, 89] arba pakitu-

siai cheminiai dinamikai [22,63]. Tačiau svarbi savybė atsiranda ir dėl spektrinių linijų modifikacijos, kuri atitinka pakitusią laikinę emisijos dinamiką [58]. Įprastai sužadinta būsena molekulėje ar atome atiduoda savo energiją spontantinės emisijos būdu, kuris aprašo perėjimą iš sužadintos būsenos į žemesnės energijos būseną. Kai molekulė ar atomas sužadinamas sugeriant spinduliuotę, spontaninė emisija vadinama fluorescencija. Šviesos sąveika su molekulėmis paprastai apima eksitonines būsenas, kurios aprašomos kaip surištos elektrono ir elektrono skylės būsenos, tarpusavyje veikiančios elektrostatine Kulono trauka. Eksitonas yra neutrali kvazidalelė, laikoma elementariaja sužadinimo forma kietojo kūno fizikoje. Molekuliniai eksitonai fluorescencijos dažuose gali būti vertinami kaip molekulių sužadintos būsenos. Kai molekulė pagrindinėje būsenoje sugeria fotoną, kurio energija lygi ar didesnė už aukštesniųjų sužadintų būsenų energijas (S_1, S_2, … S_n), elektronas sužadinamas į aukštesnį energijos lygį. Elektroninis perėjimas į pagrindinę būseną gali vykti pagal įvairius molekulinėms sistemoms būdingus energijos perdavimo mechanizmus [90]. Dėl vibroninės relaksacijos elektronai gali nevykstant spinduliavimui pereiti iš aukštesnio vibracinio lygmens sužadintoje būsenoje į žemiausią tos pačios sužadintos būsenos vibracinį lygmenį. Šis procesas vadinamas vidine konversija. Netrukus po to vyksta spinduliniai arba nespinduliniai elektroniniai perėjimai į pagrindinę būseną.

Spindulinis procesas, kurio metu molekulė sugrįžta į pagrindinę būseną išspinduliuodama fotoną, vadinamas fluorescencija. Organiniams dažams šis procesas dažniausiai trunka apie 10^{-9} ns. Fluorescuojančio fotono energija yra mažesnė nei sužadinimui reikalinga energija, todėl emisija paprastai stebima ilgesnių bangų ilgių srityje. Šis energijos (bangos ilgio) poslinkis, kylantis dėl vidinės konversijos procesų, vadinamas Stokso poslinkiu.

Šis procesas vyksta be išorinės paskatos ir apibūdinamas fluorescencijos gyvavimo trukme (angl. fluorescence lifetime), kuri nusako vidutinį laiką, per kurį sužadinta būsena išspinduliuoja fotoną ir grįžta į pagrindinę būseną. Fluorescencijos intensyvumo mažėjimas laike dažniausiai aprašomas eksponentine priklausomybe, o gyvavimo trukmė priklauso nuo spontaninės emisijos greičio, kurį savo ruožtu lemia lokalus fotonų tankis ir aplinkos optinės savybės.

Kai šviesos šaltinis (pvz., fluoroforas ar eksitonas) patenka į rezonansinę optinę aplinką, pvz. rezonatorius ar plazmoninė struktūra, jo spinduliavimo savybės gali reikšmingai keistis – tai vadinama Purcello efektu. Šis efektas leidžia padidinti arba sumažinti spontaninės emisijos greitį, priklausomai nuo optinės aplinkos modų tankio.

Stiprosios sąveikos atveju laikinė dinamika tampa dar sudėtingesnė. Čia elektromagnetinis laukas ir sužadinta būsena nuolat koherentiškai keičiasi energija su dažniu, vadinamu Rabi dažniu. Tokiu atveju energijos mainai tarp fotonų ir eksitonų vyksta periodiškai – susidaro Rabi virpesiai. Šiuos koherentinius svyravimus galima stebėti laike atliekant žadinimo-zondavimos eks-

perimentus. Dėl šių virpesių fluorescencijos intensyvumo kitimas nebeatitinka paprastos eksponentinės kreivės – atsiranda osciliacinės komponentės, atspindinčios kvantinę energijos mainų dinamiką tarp šviesos ir materijos.

Šie laikiniai reiškiniai leidžia tiesiogiai tirti koherencijos trukmę, sąveikos stiprį ir dekoherencijos mechanizmus, todėl yra ypač svarbūs kvantinės optikos, nanofotonikos ir kvantinės informacijos srityse, kur siekiama valdyti šviesos–medžiagos sąveiką.

Metodai

Metodikos naudotos tyrimo metu yra apibendrintos ir trumpai pristatytos šiame skyriuje. Šios metodikos apima BFP vaizdinimą, laike koreliuotų pavienių fotonų skaičiavimą (angl. TCSPC), elipsometriją, bandinio gamybos metodikas, o taip pat ir fotoliuminescencijos bei visiško vidaus atspindžio fluorescencijos metodikas.

TCSPC pagrįstas tiksliai išmatuotų pavienių fluorescuojančių fotonų registravimu, naudojant sužadinimo impulsą kaip atskaitos tašką (Pav. 5.6). Sužadinus šviesą emituojančias medžiagas, tokias kaip kvantiniai taškai ar organiniai dažai, įvyksta spontaninė emisija. Kaip jau minėta 1.5 skyriuje, sužadintos molekulės turi atitinkamą gyvavimo trukmę τ_0, apibūdinančią vidutinį laiką, kurį molekulė praleidžia sužadintoje būsenoje. Pavienio fotono detekcija nepateikia visos informacijos apie emisijos intensyvumo laikinę priklausomybę. Todėl TCSPC naudojama, kad pilnai ištirti laikinį intensivymo kitimą.

Ši technika susideda iš mėginio sužadinimo itin trumpais lazerio impulsais, po kurių kiekvieno sužadinimo spontaniškai išspinduliuojami fotonai (Pav. 5.6). Išspinduliuota šviesa yra spektriškai filtruojama, surenkama ir nukreipiama į SPAD detektorių, kuris pavienius fotonus paverčia elektroniniais impulsais. Kiekvienas lazerio optinis impulsas taip pat užduota ir elektrinį impulsą kuris yra siunčiamas į TCSPC plokštę ir veikia kaip START signalas. STOP signalas yra fiksuojamas iš detektuoto fluorescencijos signalo. Laiko skirtumas tarp START ir STOP leidžia ištirti fluorescencijos gyvavimo trukmes.

BFP yra optinė technika, leidžianti analizuoti šviesos kampinį pasiskirstymą ir tirti emisijos bei sklaidos savybes nanofotoninėse struktūrose (Pav. 5.7). Šis metodas pagrįstas Fourier optikos principais, pagal kuriuos lęšis transformuoja erdvinį vaizdo pasiskirstymą į kampinį. Kitaip tariant, šviesos intensyvumo pasiskirstymas galinėje židinio plokštumoje atitinka spinduliuotės arba sklaidos kampų pasiskirstymą, o kampinio spektro $E(u, v)$ ir erdvinio pasiskirstymo $E(x, y)$ ryšys aprašomas Furjė transformacija [1, 116]. Naudojant BFP vaizdinimą galima tiesiogiai gauti informaciją apie emiterių kryptingumą, dipolių orientaciją, sklaidos anisotropiją ir t.t. Ši technika ypač naudinga tiriant plazmoninius reiškinius, metapaviršius, nanodaleles ir pavienių fotonų šaltinius, kur emisijos kampinė priklausomybė yra glaudžiai susijusi su šviesos–medžiagos są-

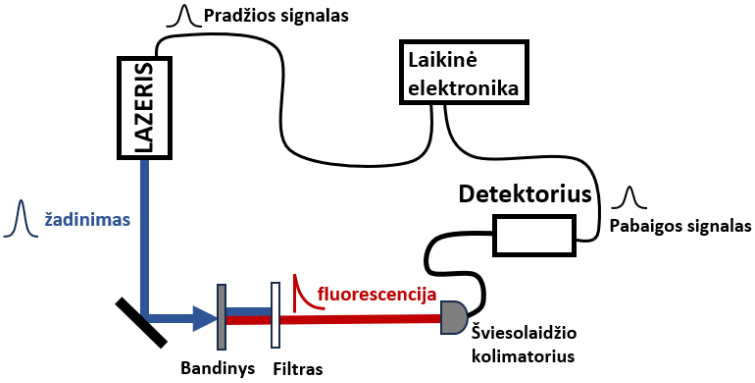

5.6 Pav. Tipinė TCSPC fluorescencijos gyvavimo trukmės matavimo schema žadinant pavieniais lazerio impulsais.

veika.

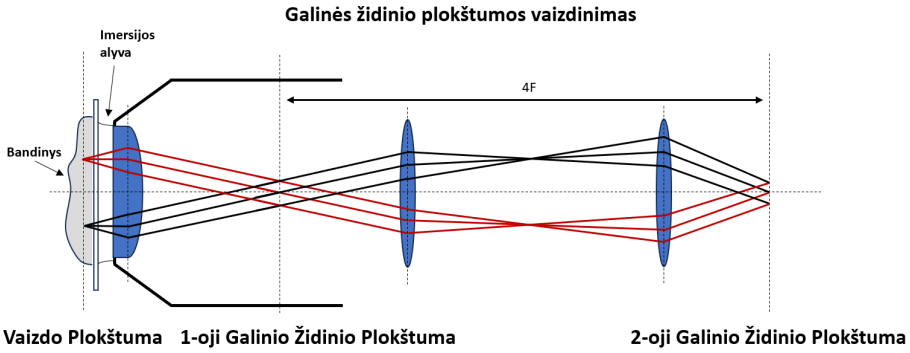

5.7 Pav. Principinė BFP vaizdinimo konfigūracija. Šviesos spinduliai, sklindantys iš dviejų erdvėje atskirtų taškų, fokusuoja pagal spinduliuotės kampą į pirmąją Furjė plokštumą. Pirmojoje Furjė plokštumoje susiformavę vaizdai dvigubos lęšių sistemos pagalba pervaizduojami į antrąją Furjė plokštumą.

Elipsometrija yra optinis matavimo metodas, naudojamas plonų sluoksnių storio, lūžio rodiklio ir optinių savybių nustatymui. Ji pagrįsta poliarizuotos šviesos atspindžio ar pralaidumos pokyčių analize, kai šviesa sąveikauja su tiriamu paviršiumi. Matavimo metu nustatomi du parametrai – amplitudės santykis (Ψ) ir fazės skirtumas (Δ) tarp p- ir s-poliarizacijos komponentų (Pav. 5.8). Šie dydžiai leidžia tiksliai modeliuoti sluoksnio struktūrą ir optinius parametrus. Dėl savo aukšto jautrumo, elipsometrija plačiai taikoma puslaidininkių, plonų plėvelių, nanostruktūrų ir optinių dangų charakterizavimui.

Fotoliumenescencijos ir visiško vidaus atspindžio fluorescencijos metodikos buvo naudojamos tyrimų metu. Fotoliumenescencijos metu išspinduliuota šviesa buvo surenkama šviesolaidžio pagalba ir nukreipta į spektrometrą. Tai leido tiksliai išmatuoti emituotos spinduliuotės spektrines charateristikas spindu-

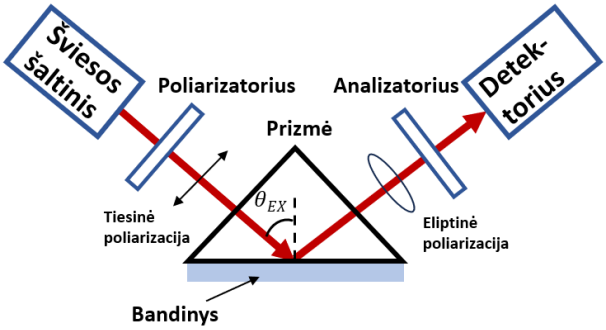

5.8 Pav. Tipinė spektroskopinės elipsometrijos sistema susideda iš balto šviesos šaltinio mėginiui apšviesti, poliarizatoriaus, kompensatoriaus (esančio krintančios arba atspindėtos šviesos kelyje), analizatoriaus (antrojo poliarizatoriaus) ir detektoriaus.

liuojant skirtingai kampais iš suformuotos struktūros. Visiško vidaus atspindžio fluorescencijos metodika buvo taikoma rezonansiškai žadinti poliaritonines SPP-R6G būsenas. Šis metodas, paremtas visiško vidaus atspindžio metu susidarusia gęstančia elektromagnetine banga, kuri buvo naudojama bandinių žadinimui.

Bandinių gamybai buvo naudojami magnetroninio dulkinimo ir sluoksnio liejimo centrifūguojant metodai. Magnetroninio dulkinimo technologija leido suformuoti 45 nm storio Ag dangas ant stiklo padėklų. Magnetroninis dulkinimas yra paremtas tiesioginiu garų nusodinimu naudojant magnetinį lauką technologija. Bandinio formavimas centrifūguojant vyksta bandiniui besisukant didelio greičiu (2000-3000 aps./min) apie savo ašį. Atsiradusi išcentrinė jėga suformuoja ploną tolygų sluoksnį ant paviršiaus, kai medžiaga yra užlašinama ant besisukančio padėklo.

Rezultatai

Atlikti ir 3 skyriuje pristatyti tyrimai daug dėmesio skiria optiniams poliaritoniniams biojutikliams. Šiame tyrime pristatome hibridinį metodą su HSA baltymais, išnaudojant stipriosios sąveikos efektą tarp plazmoninių rezonansų ir baltymo dažo eksitonų. Tyrimo metu buvo modeliuotas optinis atsakas struktūrų padengtų 45 nm ištisine aukso danga ir 11 nm HSA baltymo sluoksniu. Skirtingas optinis atsakas yra analizuojamas keičiant Alexa633 fluorescuojančio molekulinio dažo koncentraciją HSA baltyme nuo 0% (nežymėtas HSA baltymas) iki 100% (pilnai žymėtas HSA baltymas). Esant skirtingos dažo koncentracijoms, susidaręs Rabi tarpas optinėje dispersijoje siekė nuo 88 iki 140 meV (55% - 100%).

Mūsų rezultatai rodo, kad Rabi energija turi parabolinę priklausomybę nuo ant jutiklio paviršiaus adsorbuotų pažymėtų baltymų kiekio. Vis dėlto realio-

mis fotoninių–plazmoninių sistemų eksperimentinėmis sąlygomis Rabi energija kinta siaurame intervale, todėl šią priklausomybę galima artimai aproksimuoti tiesine funkcija (Pav. 5.9B intarpas). Stiprios šviesos ir medžiagos sąveikos panaudojimas imunokompleksuose suteikia galimybių keisti cheminį reaktyvumą, modifikuoti sužadintos būsenos relaksacijos kelius, reguliuoti krūvio laidumą ir daryti įtaką baltymų prisijungimo kinetikai.

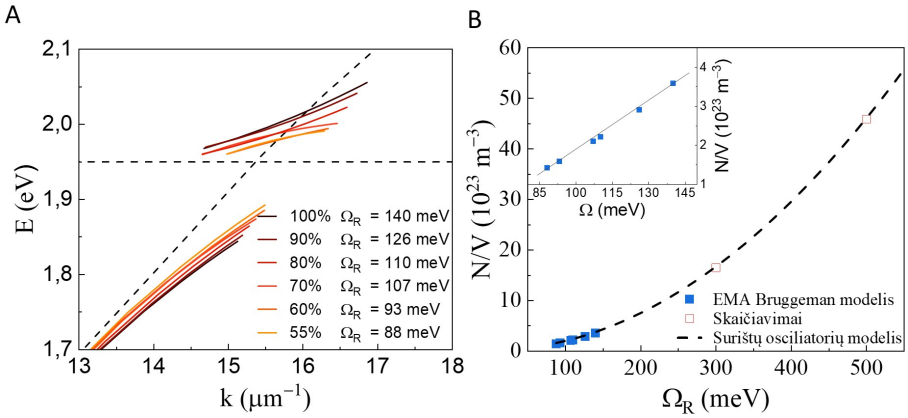

5.9 Pav. Stipriojoje sąveikoje esančių hibridinių SPP - eksitono būsenų dispersijos banginių vektorių (k) erdvėje ir šių dispersijų priklausomybė nuo skirtingų pradinių koncentracijų (55-100 %) žymėtame proteine (A); ant paviršiaus adsorbuotų proteino molekulių koncentracijos priklausomybė nuo sumodeliuoto Rabi energijos tarpo (B).

Be to, bio-poliaritoninių būsenų, formuojamų dalyvaujant baltymams, atsiradimas atveria galimybes ne tik biojutikliuose, bet ir kvantinės informacijos apdorojime. Stipriai sąveikaujančių būsenų susidarymas tarp plazmoninių rezonansų ir baltymų–dažų kompleksų atveria naujas galimybes biojutikliuose, kuriose nežymėti ir žymėti metodai gali būti integruojami, siekiant valdyti baltymų sąveikos kinetiką per sąveikos stiprį. Tai gali paskatinti inovacijas, tokias kaip bio-nanolazeriai, ir atverti naujas kryptis poliaritoninėje biochemijoje.

4 Skyriuje pristatyti stipriai sąveikaujančių plazmoninio rezonanso 45 nm sidabro sluoksnyje ir R6G molekulinio eksitono būsenų dinaminių savybių tyrimai. Tyrimu metu buvo taikytos kelios eksperimentinės technikos. Rabi energija buvo įvertinta naudojant spektroskopinę elipsometriją TIRE konfigūracijoje ir gautas sąveikos stipris g siekė 200 meV, taip patvirtinant stipriąją sąveiką. Fotoliuminescencijos matavimai parodė emisiją ne tik nuo kampo priklausančią emisiją iš žemutinės poliaritono būsenos (LP), bet ir įprastą nuo kampo nepriklausančią R6G molekulinio dažo emisiją.

Fotoliuminescencijos savybių analizė parodė, kad reikšminga R6G molekulių dalis nedalyvavo stipriosios sąveikos režime sudarydama eksitonų rezervuarą. Fluorescencijos gyvavimo trukmės matavimai parodė, kad didėjant sužadinimo

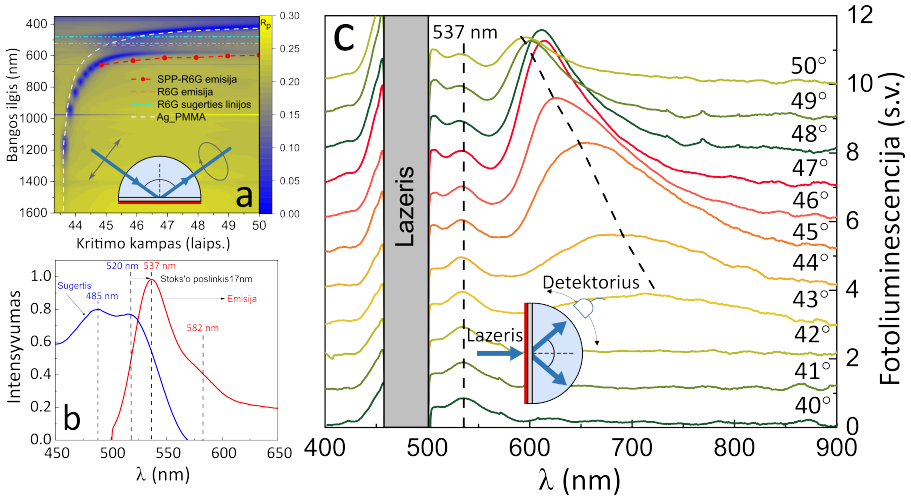

5.10 Pav. SPP - R6G molekulės eksitono emisijos ir atspindžio matavimų konfigūracijos ir išmatuoti spektrai stipriosios sąveikos režime: (a) R6G molekulės eksitono ir SPP dispersiniai žemėlapiai stipriosios sąveikos režime matuojant visiško vidaus atspindžio elipsometrija; (b) R6G molekulės sugerties ir emisijos spektrai. Stokto poslinktis apie 17nm; (c) SPP-R6G emisijos spektrai prie skirtingų kampų (40° - 50°). Emisijos maksimumų poslinktis nuo kampo pažymėtas punktyrine linija. Principinė matavimų schema pavaizduota intarpe.

kampui link rezonansinių sąlygų, eksitoninio rezervuaro įtaka stipriai surištų sistemų dinamikai tampa minimali. Pamatuotos fluorescencijos gyvavimo trukmės buvo šimtų pikosekundžių intervale ir priklausė nuo sužadinimo sąlygų. Stebėtos fluorescencijos gesimo trukmės buvo gerokai ilgesnės nei tikėtinos plazmoninėms sužadintoms būsenoms, kurių gyvavimo trukmė yra femtosekundžių eilės. Todėl gauti rezultatai negali būti paaiškinami be papildomo indėlio iš kitų energijos lygmenų, tokių kaip nekoherentiniai perėjimai iš eksitoninio rezervuaro būsenos.

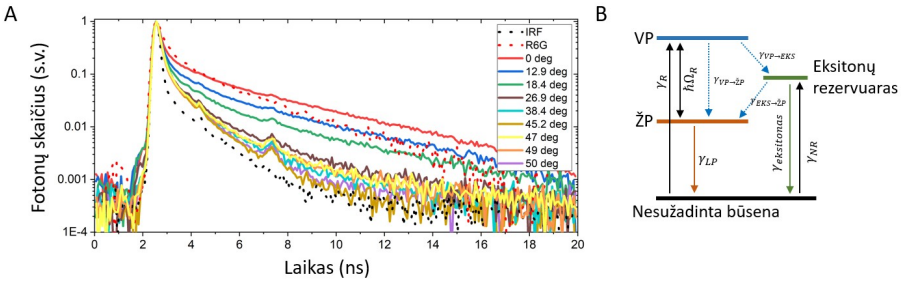

5.11 Pav. Stipriai sąveikaujančio SPP-R6G bandinio fluorescencija: (A) laikinė fluorescencijos priklausomybė nesąveikajančių R6G molekulių PMMA matricoje (raudona punktyrinė linija) ir stipriai sąveikaujančių su SPP prie skirtingų žadinimo kampų (ištisinės linijos); (B) Energetinių lygmenų sistema, abibūdinanti energetinius mainus tarp UP, LP, ER ir G būsenų rezonansinio ir nerezonansinio žadinimo metu.

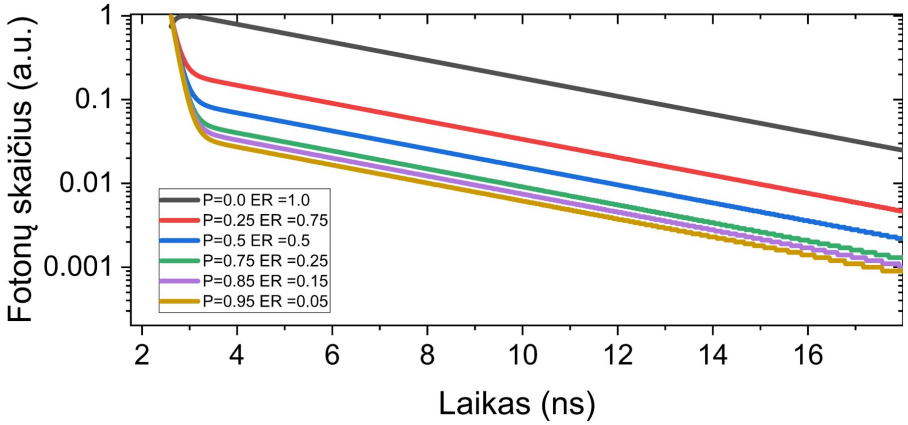

5.12 Pav. Emisijos intensyvumo laikinė priklausomybė sumodeliuota esant skirtingoms pradinėms UP ir ER būsenų koncentracijoms stipriosios sąveikos režime.

Trijų lygmenų sistema leido kokybiškai įvertinti fluorescencijos gyvavimo trukmės priklausomybę nuo bandinio žadinimo sąlygų ir parodė, kad poliaritoninė emisija yra priklausoma nuo tiesiogiai stipriojoje sąveikoje nedalyvaujančių Rodamino molekulių. Šis tyrimas suteikė papildomų įžvalgų apie energijos mainų procesus poliaritoninėse sistemoje ir yra būtina nanofotoninių prietaisų, ir poliaritoninių lazerių kūrimui.

5 Skyriuje buvo atlikti poliaritoninės fluorescencijos gyvavimo trukmės matavimai skirtinguose emisijos kampuose SPP–R6G mėginiams. Ištirta dviejų sluoksnių struktūra, sudaryta iš tolygaus sidabro sluoksnio (45 nm) ir R6G molekulinio dažo, bei atlikti TIRE matavimai. Optinis atsakas buvo įvertintas naudojant surištų osciliatorių modelį, kuris parodė, kad sąveikos stipris g siekia

iki 160 meV. Emisijos savybėms tirti buvo naudota BFP mikroskopijos sistema. Optinio erdvinio filtravimo metodika buvo pritaikyti emisijos kampams atskirti ir fluorescencijos dinamikai ištirti.

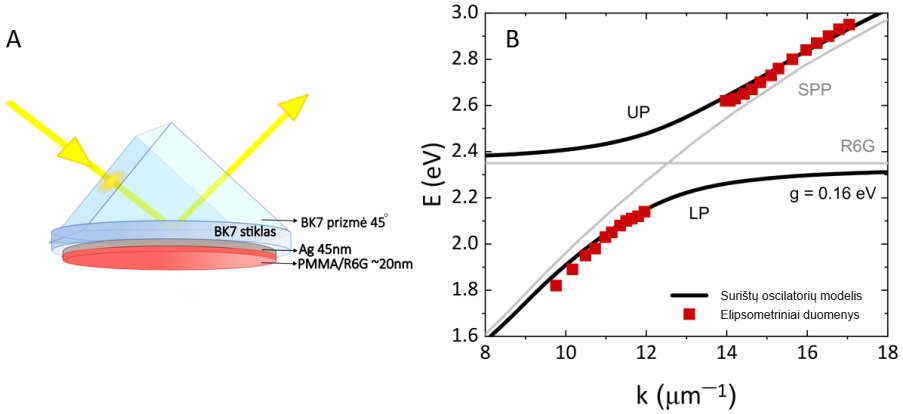

5.13 Pav. Visiško vidaus atspindžio elipsometrija: a) Principinė TIRE matavimo schema naudojant 45° prizmę; b) SPP-R6G energijos - banginio vektoriaus dispersiniai sąryšiai stipriosios sąveikos režime, kai $g = 160$ meV ties susikirtimo tašku ($k_{||} = 12.5\ \mu m^{-1}$).

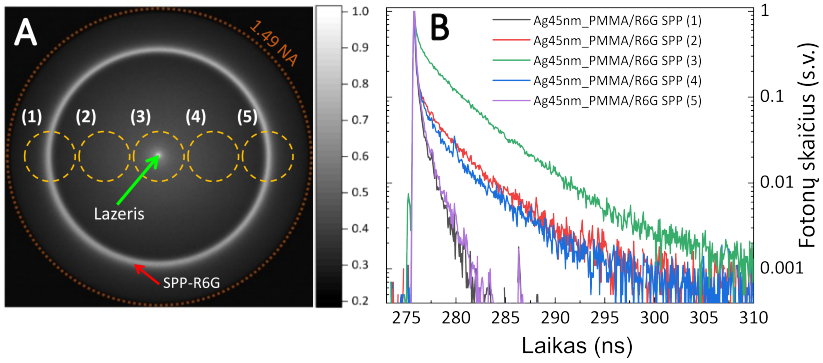

5.14 Pav. Fluorescencijos gyvavimo trukmės tyrimas naudojant erdviškai filtruota galinės židinio plokštumos vaizdinimą: a) SPP-R6G bandinio stipriojoje sąveikoje BFP vaizdinimas. Gyvavimo trukmės matavimai buvo atlikti erdviškai išfiltuojant skirtingas BFP vietas. Didžiausias mikroskopo objektyvo šviesos surinkimo kampas pažymėtas raudona punktyrine linija (NA = 1.49).

Rezultatai parodė, kad intensyvumo pasiskirstymas BFP atsiranda kaip skirtingų fluorescencijos gyvavimo trukmių mišinys, kuris atskleidžia skirtingas emisijos kryptis nanofotoninėje struktūroje. Pasiūlytas erdvinio filtravimo metodas buvo patvirtintas naudojant SPP–R6G mėginius. Greitesnis emisijos procesai pozicijose (1) ir (5) (Pav. 5.14) buvo stebėti dėl stipriosios sąveikos

būdingos $\pm 43^\circ$ kampams, tačiau stebimas signalas šiuose kampuose yra dominuojamas IRF. Pozicijose (2) ir (4) buvo užfiksuota 0.1 ns laikai, o pozicijoje (3) $\rightarrow$ 0.18 ns gyvavimo trukmė, kas rodo, jog fluorescencijos trukmė priklauso nuo emisijos kampo. Šie rezultatai suteikia galimybę atskirti silpnai ir stipriai susietas būsenas nanofotoniniuose įrenginiuose.

Išvados

- Optinis atsakas ir dispersiniai sąryšiai buvo tiriami naudojant efektyvios terpės Bruggemanno aproksimaciją nežymėtų ir žymėtų baltymų–dažų kompleksams, susietiems su ištisiniu 45 nm storio aukso sluoksniu. Stebėtas Rabi tarpas atskleidė stipriosios sąveikos režimą HSA baltymo molekulėse, o Rabi energija priklausė nuo pradinės A633 dažiklio koncentracijos.

- Stipriai surištų pažymėtų HSA baltymo kompleksų Rabi energijos analizė parodė, kad Ω_R priklauso nuo ant aukso paviršiaus adsorbuotos baltymo koncentracijos, o dalyvaujančių baltymo molekulių vidutinė koncentracija siekė $\sim 10^{23}\ m^{-3}$. Parabolinį Rabi energijos ir dalyvaujančių dalelių skaičiaus ryšį galima aproksimuoti tiesiškai, kai sąveikos intervalas yra apie 60 meV.

- Atvirkštinė Kretschmanno konfigūracija buvo naudojama SPP–R6G nanofotoninės struktūros sužadinimui ir emisijai registruoti. Fotoliuminescencija buvo renkama kampų intervale nuo 40° iki 50° esant nerezonansiniam sužadinimui. Stebėta šviesos dispersija sekė apatiniosios (LP) poliaritonų šakos elgseną, išmatuotą TIRE metodu, taip patvirtinant emisiją iš stipriai surištų poliaritoninių būsenų.

- Fluorescencijos gyvavimo trukmės matavimai buvo atlikti keičiant sužadinimo kampą BFP mikroskopijos sistemoje. Nustatyta, kad poliaritoninės būsenos gyvavimo trukmė priklauso nuo pradinių sužadinimo sąlygų – eksitonų rezervuaro įtaka buvo stebima esant $\leq 18.2°$ sužadinimo kampui. Padidinus sužadinimo kampą virš 18.2°, didėja viršutinio poliaritono populiacijos dalis poliaritoninėse būsenose.

- Stebėtai gyvavimo trukmės elgsenai paaiškinti pasiūlytas paprastas trejų lygmenų modelis. Skaitmeninis modelis, įtraukiantis papildomus perėjimus per eksitonų rezervuaro būseną, parodė atitikimą su išmatuotais duomenimis ir patvirtino, kad pailgėjusi poliaritonų gyvavimo trukmė esant nerezonansiniam sužadinimui kyla dėl lėtų vidinių perėjimų iš eksitoninio rezervuaro į apatinę poliaritoninę būseną.

- Surištų osciliatorių modelis buvo naudojamas įvertinti sąveikos stipriui g bandiniuose pamatuotose TIRE metodu. Apskaičiuota dispersijos kreivė sutapo su matavimais ir parodė, kad SPP ir R6G sąveikos stipris siekė apie 160 meV.

- Naudojant erdvinio filtravimo techniką, buvo selektyviai filtruojami skirtingi emisijos kampai, BFP mikroskopijos konfigūracijoje. Eksperimentas parodė, kad trumpiausia fluorescencijos gyvavimo trukmė buvo stebima

iš SPP emisijos žiedo ties $\pm 43^\circ$ dėl stipriosios sąveikos, o ilgiausia – ties 0° ir buvo priskirta silpnai susietoms R6G molekulėms.

PADĖKA

Visų pirma norėčiau išreikšti savo dėkingumą darbo vadovui Prof. dr. Zigmui Balevičiui už suteiktą galimybę dirbti su šios disertacijos tema. Esu dėkingas už galimybę dalyvauti mokslinėse diskusijose, taip pat už stiprią paramą ir pagalbą visus šiuos metus.

Taip pat noriu padėkoti dr. Vytautui Žičkui. Jo entuziazmas ir suteiktos galimybės, tarp jų galimybė lankytis ir dirbti Glazgo universitete, turėjo itin didelę reikšmę studijų metu.

Nuoširdžiai dėkoju dr. Ernestai Bužavaitei-Vertelienei už prasmingas diskusijas ir pagalbą rengiant publikacijas, dr. Justinai Anulytei už mėginių paruošimą ir elipsometrinius matavimus, bei Evitai Spalinskaitei iš pagalbą laboratorijoje.

Galiausiai norėčiau padėkoti savo šeimai už palaikymą studijų metu, o ypač Dainorai už jos kantrybę ir nuolatinį palaikymą.

PUBLIKACIJŲ SARAŠAS

P1 **P. Jurkšaitis**, J. Anulytė, E. Spalinskaitė, E. Bužavaitė-Vertelienė, V. Žičkus, I. Plikusienė Z. Balevičius, Spatially filtered back focal plane imaging for directional fluorescence lifetime study of polaritonic states, *Photonics* , 12, 1165, (2025), doi: 10.3390/photonics12121165.

P2 **P. Jurkšaitis**, J. Anulytė, E. Spalinskaitė, E. Bužavaitė-Vertelienė, V. Žičkus, D. Banevičius, K. Kazlauskas, Z. Balevičius, Plasmon-exciton polaritonic emission lifetime dynamics under strong coupling, *Nanophotonics*, 14, 14, 2485-2493, (2025), doi: 10.1515/nanoph-2025-0129.

P3 **P. Jurkšaitis**, E. Bužavaitė-Vertelienė, Z. Balevičius, Strong coupling between surface plasmon resonance and exciton of labeled protein-dye complex for immunosensing applications, *Int. J. Mol. Sci.*, 24, 3, 2009, (2023), doi: 10.3390/ijms24032029.

Konferencijos

C1 **P. Jurkšaitis**, J. Anulytė, D. Banevičius, E. Bužavaitė-Vertelienė, Z. Balevičius. Paviršinio plazmono ir R6G eksitono emisija stipriosios sąveikos režime, Fiztech, Vilnius, Lietuva, Spalio 15-17 d. 2024 m., (žodinis)

C2 **P. Jurkšaitis**, V. Žičkus, A. Lyons, R. Alvarez-Mendoza, Z. Balevičius, D. Faccio. Hong-Ou-Mandel enhanced fluorescence interferometry. International conference on quantum optics and quantum information, Insbrukas, Austrija, Rugsėjis 16-20 d. 2024 m., (stendinis)

C3 **P. Jurkšaitis**, V. Žičkus, J. Anulytė, E. Bužavaitė-Vertelienė, Z. Balevičius. Surface plasmon coupled emission of Rhodamine 6G dye in strong coupling regime, Photon, Svonsis, Jungtinė Karalystė, September 2-6 d. 2024 m., (stendinis)

C4 **P. Jurkšaitis**, J. Anulytė, Z. Balevičius. Stipriosios sąveikos režimas tarp paviršinių plazmonų ir Rodamino 6G molekulių, Fiztech, Vilnius, Lietuva, Spalio 18-19 d. 2023 m., (žodinis)

C5 **P. Jurkšaitis**, J. Anulytė, Z. Balevičius. Light-matter coupling between surface plasmon polaritons and Rhodamine 6G dye, Hybrid quantum systems, Viena, Austrija, Rugpjūtis 28 – Rugsėjis 1 d. 2023 m., (stendinis)

C6 **P. Jurkšaitis**, Z. Balevičius. Strong Light-matter coupling between surface plasmon polaritons and Rhodamine 6G dye, Advanced Materials and Technologies, Palanga, Lietuva, Rugpjūtis 21 – 25 d. 2023 m., (stendinis)

C7 **P. Jurkšaiti**s, E. Bužavaitė-Vertelienė, Z. Balevičius. Strong coupling between surface plasmon resonance and exciton labeled protein-dye complex for immunosensing applications. 64th International conference for students of physics and natural sciences Open Readings, Vilnius, Lietuva, Balandis 17-21 d. 2023 m.,(stendinis)

C8 **P. Jurkšaiti**s, Z. Balevičius. Modelling of strong coupling between surface plasmon polaritons and protein-dye complex exciton of HSA antibody labeled with Rhodamine101 dye, Fiztech, Vilnius, Lietuva, Spalio 19-20 d. 2022 m., (žodinis)

BIBLIOGRAPHY

[1] C. S. Adams, I. G. Hughes, *Optics f2f: From Fourier to Fresnel* (Oxford University PressOxford, 2018), 1 edition.

[2] E. Abbe, Beiträge zur Theorie des Mikroskops und der mikroskopischen Wahrnehmung, Archiv für Mikroskopische Anatomie **9**(1), 413–468 (1873), https://doi.org/10.1007/BF02956173.

[3] E. A. Ash, G. Nicholls, Super-resolution Aperture Scanning Microscope, Nature **237**(5357), 510–512 (1972), https://doi.org/10.1038/237510a0.

[4] D. W. Pohl, W. Denk, M. Lanz, Optical stethoscopy: Image recording with resolution λ/20, Applied Physics Letters **44**(7), 651–653 (1984), https://doi.org/10.1063/1.94865.

[5] A. Lewis, M. Isaacson, A. Harootunian, A. Muray, Development of a 500 Å spatial resolution light microscope, Ultramicroscopy **13**(3), 227–231 (1984), https://doi.org/10.1016/0304-3991(84)90201-8.

[6] U. C. Fischer, Optical characteristics of 0.1 µm circular apertures in a metal film as light sources for scanning ultramicroscopy, Journal of Vacuum Science & Technology B: Microelectronics Processing and Phenomena **3**(1), 386–390 (1985), https://doi.org/10.1116/1.583269.

[7] H. Wei, X. Yan, Y. Niu, Q. Li, Z. Jia, H. Xu, Plasmon–Exciton Interactions: Spontaneous Emission and Strong Coupling, Advanced Functional Materials **31**(51), 2100889, number: 51 (2021), https://doi.org/10.1002/adfm.202100889.

[8] L. Novotny, B. Hecht, *Principles of Nano-Optics* (Cambridge University Press, 2012), 2 edition.

[9] A. González-Tudela, A. Reiserer, J. J. García-Ripoll, F. J. García-Vidal, Light–matter interactions in quantum nanophotonic devices, Nature Reviews Physics **6**(3), 166–179, number: 3 (2024), https://doi.org/10.1038/s42254-023-00681-1.

[10] Y. Kim, A. Barulin, S. Kim, L. P. Lee, I. Kim, Recent advances in quantum nanophotonics: plexcitonic and vibro-polaritonic strong coupling and its biomedical and chemical applications, Nanophotonics **12**(3), 413–439, number: 3 (2023), https://doi.org/10.1515/nanoph-2022-0542.

[11] N. Rivera, I. Kaminer, Light–matter interactions with photonic quasiparticles, Nature Reviews Physics **2**(10), 538–561, number: 10 (2020), https://doi.org/10.1038/s42254-020-0224-2.

[12] S. I. Azzam, A. V. Kildishev, R.-M. Ma, C.-Z. Ning, R. Oulton, V. M. Shalaev, M. I. Stockman, J.-L. Xu, X. Zhang, Ten years of spasers and plasmonic nanolasers, Light: Science & Applications **9**(1), 90 (2020), https://doi.org/10.1038/s41377-020-0319-7.

[13] W. L. Barnes, Surface plasmon–polariton length scales: a route to sub-wavelength optics, Journal of Optics A: Pure and Applied Optics **8**(4), S87–S93, number: 4 (2006), https://doi.org/10.1088/1464-4258/8/4/S06.

[14] P. Anger, P. Bharadwaj, L. Novotny, Enhancement and Quenching of Single-Molecule Fluorescence, Physical Review Letters **96**(11), 113002, number: 11 (2006), https://doi.org/10.1103/PhysRevLett.96.113002.

[15] E. M. Purcell, Spontaneous Emission Probabilities at Radio Frequencies, Physical Review **69**, 681 (1946), https://doi.org/10.1103/PhysRev.69.674.2.

[16] R. Chikkaraddy, B. De Nijs, F. Benz, S. J. Barrow, O. A. Scherman, E. Rosta, A. Demetriadou, P. Fox, O. Hess, J. J. Baumberg, Single-molecule strong coupling at room temperature in plasmonic nanocavities, Nature **535**(7610), 127–130, number: 7610 (2016), https://doi.org/10.1038/nature17974.

[17] J. Bellessa, C. Bonnand, J. C. Plenet, J. Mugnier, Strong Coupling between Surface Plasmons and Excitons in an Organic Semiconductor, Physical Review Letters **93**(3), 036404, number: 3 (2004), https://doi.org/10.1103/PhysRevLett.93.036404.

[18] S. Hu, J. Huang, R. Arul, A. Sánchez-Iglesias, Y. Xiong, L. M. Liz-Marzán, J. J. Baumberg, Robust consistent single quantum dot strong coupling in plasmonic nanocavities, Nature Communications **15**(1), 6835, number: 1 (2024), https://doi.org/10.1038/s41467-024-51170-7.

[19] T. Aoki, B. Dayan, E. Wilcut, W. P. Bowen, A. S. Parkins, T. J. Kippenberg, K. J. Vahala, H. J. Kimble, Observation of strong coupling between one atom and a monolithic microresonator, Nature **443**(7112), 671–674 (2006), https://doi.org/10.1038/nature05147.

[20] J. Flick, N. Rivera, P. Narang, Strong light-matter coupling in quantum chemistry and quantum photonics, Nanophotonics **7**(9), 1479–1501, number: 9 (2018), https://doi.org/10.1515/nanoph-2018-0067.

[21] A. F. Koenderink, A. Alù, A. Polman, Nanophotonics: Shrinking light-based technology, Science **348**(6234), 516–521 (2015), https://doi.org/10.1126/science.1261243.

[22] F. Herrera, F. C. Spano, Cavity-Controlled Chemistry in Molecular Ensembles, Physical Review Letters **116**(23), 238301, number: 23 (2016), https://doi.org/10.1103/PhysRevLett.116.238301.

[23] R. F. Ribeiro, L. A. Martínez-Martínez, M. Du, J. Campos-Gonzalez-Angulo, J. Yuen-Zhou, Polariton chemistry: controlling molecular dynamics with optical cavities, Chemical Science **9**(30), 6325–6339, number: 30 (2018), https://doi.org/10.1039/C8SC01043A.

[24] A. Lishchuk, C. Vasilev, M. P. Johnson, C. N. Hunter, P. Törmä, G. J. Leggett, Turning the challenge of quantum biology on its head: biological control of quantum optical systems, Faraday Discussions **216**, 57–71 (2019), https://doi.org/10.1039/C8FD00241J.

[25] A. P. Vinogradov, A. V. Dorofeenko, A. A. Pukhov, A. A. Lisyansky, Exciting surface plasmon polaritons in the Kretschmann configuration by a light beam, Physical Review B **97**(23), 235407 (2018), https://doi.org/10.1103/PhysRevB.97.235407.

[26] K. M. Mayer, J. H. Hafner, Localized Surface Plasmon Resonance Sensors, Chemical Reviews **111**(6), 3828–3857 (2011), https://doi.org/10.1021/cr100313v.

[27] P. Törmä, W. L. Barnes, Strong coupling between surface plasmon polaritons and emitters: a review, Reports on Progress in Physics **78**(1), 013901, number: 1 (2015), https://doi.org/10.1088/0034-4885/78/1/013901.

[28] S. Kühn, U. Håkanson, L. Rogobete, V. Sandoghdar, Enhancement of Single-Molecule Fluorescence Using a Gold Nanoparticle as an Optical Nanoantenna, Physical Review Letters **97**(1), 017402, number: 1 (2006), https://doi.org/10.1103/PhysRevLett.97.017402.

[29] J. Seidel, S. Grafström, L. Eng, Stimulated Emission of Surface Plasmons at the Interface between a Silver Film and an Optically Pumped Dye Solution, Physical Review Letters **94**(17), 177401 (2005), https://doi.org/10.1103/PhysRevLett.94.177401.

[30] M. Ramezani, A. Halpin, A. I. Fernández-Domínguez, J. Feist, S. R.-K. Rodriguez, F. J. Garcia-Vidal, J. Gómez Rivas, Plasmon-exciton-polariton lasing, Optica **4**(1), 31 (2017), https://doi.org/10.1364/OPTICA.4.000031.

[31] H. Wei, H. Xu, Hot spots in different metal nanostructures for plasmon-enhanced Raman spectroscopy, Nanoscale **5**(22), 10794, number: 22 (2013), https://doi.org/10.1039/c3nr02924g.

[32] J. R. Lakowicz, J. Malicka, I. Gryczynski, Z. Gryczynski, Directional surface plasmon-coupled emission: a new method for high sensitivity detection, Biochemical and Biophysical Research Communications **307**(3), 435–439, number: 3 (2003), https://doi.org/10.1016/S0006-291X(03)01214-2.

[33] P. Bharadwaj, A. Bouhelier, L. Novotny, Electrical Excitation of Surface Plasmons, Physical Review Letters **106**(22), 226802 (2011), https://doi.org/10.1103/PhysRevLett.106.226802.

[34] C. Zhang, J.-P. Hugonin, A.-L. Coutrot, C. Sauvan, F. Marquier, J.-J. Greffet, Antenna surface plasmon emission by inelastic tunneling, Nature Communications **10**(1), 4949, number: 1 (2019), https://doi.org/10.1038/s41467-019-12866-3.

[35] A. V. Akimov, A. Mukherjee, C. L. Yu, D. E. Chang, A. S. Zibrov, P. R. Hemmer, H. Park, M. D. Lukin, Generation of single optical plasmons in metallic nanowires coupled to quantum dots, Nature **450**(7168), 402–406 (2007), https://doi.org/10.1038/nature06230.

[36] J. Heckmann, K. Pufahl, P. Franz, N. B. Grosse, X. Li, U. Woggon, Plasmon-enhanced nonlinear yield in the Otto and Kretschmann configurations, Physical Review B **98**(11), 115415 (2018), https://doi.org/10.1103/PhysRevB.98.115415.

[37] T. U. Tumkur, G. Zhu, M. A. Noginov, Strong coupling of surface plasmon polaritons and ensembles of dye molecules, Optics Express **24**(4), 3921 (2016), https://doi.org/10.1364/OE.24.003921.

[38] J. Homola, Surface Plasmon Resonance Sensors for Detection of Chemical and Biological Species, Chemical Reviews **108**(2), 462–493 (2008), https://doi.org/10.1021/cr068107d.

[39] M. Hojjat Jodaylami, A. Djaïleb, P. Ricard, Lavallée, S. Cellier-Goetghebeur, M.-F. Parker, J. Coutu, M. Stuible, C. Gervais, Y. Durocher, F. Desautels, M.-P. Cayer, M. J. De Grandmont, S. Rochette, D. Brouard, S. Trottier, D. Boudreau, J. N. Pelletier, J.-F. Masson, Cross-reactivity of antibodies from non-hospitalized COVID-19 positive individuals against the native, B.1.351, B.1.617.2, and P.1 SARS-CoV-2 spike proteins, Scientific Reports **11**(1), 21601 (2021), https://doi.org/10.1038/s41598-021-00844-z.

[40] D. Aspnes, Spectroscopic ellipsometry — Past, present, and future, Thin Solid Films **571**, 334–344 (2014), https://doi.org/10.1016/j.tsf.2014.03.056.

[41] J. Spinke, M. Liley, H. J. Guder, L. Angermaier, W. Knoll, Molecular recognition at self-assembled monolayers: the construction of multicomponent multilayers, Langmuir **9**(7), 1821–1825 (1993), https://doi.org/10.1021/la00031a033.

[42] S. Löfås, B. Johnsson, A novel hydrogel matrix on gold surfaces in surface plasmon resonance sensors for fast and efficient covalent immobilization of ligands, J. Chem. Soc., Chem. Commun. (21), 1526–1528 (1990), https://doi.org/10.1039/C39900001526.

[43] P. P. Austin Suthanthiraraj, A. K. Sen, Localized surface plasmon resonance (LSPR) biosensor based on thermally annealed silver nanostructures with on-chip blood-plasma separation for the detection of dengue non-structural protein NS1 antigen, Biosensors and Bioelectronics **132**, 38–46 (2019), https://doi.org/10.1016/j.bios.2019.02.036.

[44] V. Singh, Ultrasensitive quantum dot-coupled-surface plasmon microfluidic aptasensor array for serum insulin detection, Talanta **219**, 121314 (2020), https://doi.org/10.1016/j.talanta.2020.121314.

[45] A. A. Yanik, M. Huang, O. Kamohara, A. Artar, T. W. Geisbert, J. H. Connor, H. Altug, An Optofluidic Nanoplasmonic Biosensor for Direct Detection of Live Viruses from Biological Media, Nano Letters **10**(12), 4962–4969 (2010), https://doi.org/10.1021/nl103025u.

[46] Q. Wei, M. Lee, X. Yu, E. K. Lee, G. H. Seong, J. Choo, Y. W. Cho, Development of an open sandwich fluoroimmunoassay based on fluorescence resonance energy transfer, Analytical Biochemistry **358**(1), 31–37, number: 1 (2006), https://doi.org/10.1016/j.ab.2006.08.019.

[47] X. Liu, D. Lin, W. Becker, J. Niu, B. Yu, L. Liu, J. Qu, Fast fluorescence lifetime imaging techniques: A review on challenge and development, Journal of Innovative Optical Health Sciences **12**(05), 1930003 (2019), https://doi.org/10.1142/S1793545819300039.

[48] Z. Gryczynski, I. Gryczynski, E. Matveeva, J. Malicka, K. Nowaczyk, J. R. Lakowicz, Surface-Plasmon–Coupled Emission: New Technology for Studying Molecular Processes, in *Methods in Cell Biology* (Elsevier, 2004), volume 75, 73–104.

[49] J. R. Lakowicz, Radiative decay engineering 3. Surface plasmon-coupled directional emission, Analytical Biochemistry **324**(2), 153–169, number: 2 (2004), https://doi.org/10.1016/j.ab.2003.09.039.

[50] M. Bayer, P. Hawrylak, K. Hinzer, S. Fafard, M. Korkusinski, Z. R. Wasilewski, O. Stern, A. Forchel, Coupling and Entangling of Quantum States in Quantum Dot Molecules, Science **291**(5503), 451–453 (2001), https://doi.org/10.1126/science.291.5503.451.

[51] T. J. Kippenberg, K. J. Vahala, Cavity Optomechanics: Back-Action at the Mesoscale, Science **321**(5893), 1172–1176 (2008), https://doi.org/10.1126/science.1156032.

[52] M. L. Zimmerman, M. G. Littman, M. M. Kash, D. Kleppner, Stark structure of the Rydberg states of alkali-metal atoms, Physical Review A **20**(6), 2251–2275 (1979), https://doi.org/10.1103/PhysRevA.20.2251.

[53] J. Anulytė, V. Žičkus, E. Bužavaitė-Vertelienė, D. Faccio, Z. Balevičius, Strongly coupled plasmon-exciton polaritons for photobleaching suppression, Nanophotonics **13**(22), 4091–4099 (2024), https://doi.org/10.1515/nanoph-2024-0259.

[54] J. Kasprzak, M. Richard, S. Kundermann, A. Baas, P. Jeambrun, J. M. J. Keeling, F. M. Marchetti, M. H. Szymańska, R. André, J. L. Staehli, V. Savona, P. B. Littlewood, B. Deveaud, L. S. Dang, Bose–Einstein condensation of exciton polaritons, Nature **443**(7110), 409–414, number: 7110 (2006), https://doi.org/10.1038/nature05131.

[55] M. Pelton, S. D. Storm, H. Leng, Strong coupling of emitters to single plasmonic nanoparticles: exciton-induced transparency and Rabi splitting, Nanoscale **11**(31), 14540–14552, number: 31 (2019), https://doi.org/10.1039/C9NR05044B.

[56] P. Vasa, Exciton-surface plasmon polariton interactions, Advances in Physics: X **5**(1), 1749884 (2020), https://doi.org/10.1080/23746149.2020.1749884.

[57] S. Aberra Guebrou, C. Symonds, E. Homeyer, J. C. Plenet, Y. N. Gartstein, V. M. Agranovich, J. Bellessa, Coherent Emission from a Disordered Organic Semiconductor Induced by Strong Coupling with Surface Plasmons, Physical Review Letters **108**(6), 066401, number: 6 (2012), https://doi.org/10.1103/PhysRevLett.108.066401.

[58] P. Vasa, W. Wang, R. Pomraenke, M. Lammers, M. Maiuri, C. Manzoni, G. Cerullo, C. Lienau, Real-time observation of ultrafast Rabi oscillations between excitons and plasmons in metal nanostructures with J-aggregates, Nature Photonics **7**(2), 128–132, number: 2 (2013), https://doi.org/10.1038/nphoton.2012.340.

[59] J. Keeling, S. Kéna-Cohen, Bose–Einstein Condensation of Exciton-Polaritons in Organic Microcavities, Annual Review of Physical Chemistry **71**(1), 435–459, number: 1 (2020), https://doi.org/10.1146/annurev-physchem-010920-102509.

[60] A. Amo, J. Lefrère, S. Pigeon, C. Adrados, C. Ciuti, I. Carusotto, R. Houdré, E. Giacobino, A. Bramati, Superfluidity of polaritons in semiconductor microcavities, Nature Physics **5**(11), 805–810 (2009), https://doi.org/10.1038/nphys1364.

[61] K. Georgiou, R. Jayaprakash, A. Askitopoulos, D. M. Coles, P. G. Lagoudakis, D. G. Lidzey, Generation of Anti-Stokes Fluorescence in a Strongly Coupled Organic Semiconductor Microcavity, ACS Photonics **5**(11), 4343–4351, number: 11 (2018), https://doi.org/10.1021/acsphotonics.8b00552.

[62] D. M. Coles, N. Somaschi, P. Michetti, C. Clark, P. G. Lagoudakis, P. G. Savvidis, D. G. Lidzey, Polariton-mediated energy transfer between organic dyes in a strongly coupled optical microcavity, Nature Materials **13**(7), 712–719 (2014), https://doi.org/10.1038/nmat3950.

[63] B. Munkhbat, M. Wersäll, D. G. Baranov, T. J. Antosiewicz, T. Shegai, Suppression of photo-oxidation of organic chromophores by strong coupling to plasmonic nanoantennas, Science Advances **4**(7), eaas9552, number: 7 (2018), https://doi.org/10.1126/sciadv.aas9552.

[64] W. Ni, Z. Yang, H. Chen, L. Li, J. Wang, Coupling between Molecular and Plasmonic Resonances in Freestanding DyeGold Nanorod Hybrid Nanostructures, Journal of the American Chemical Society **130**(21), 6692–6693 (2008), https://doi.org/10.1021/ja8012374.

[65] I. Pockrand, A. Brillante, D. Möbius, Exciton–surface plasmon coupling: An experimental investigation, The Journal of Chemical Physics **77**(12), 6289–6295 (1982), https://doi.org/10.1063/1.443834.

[66] G. Zengin, M. Wersäll, S. Nilsson, T. J. Antosiewicz, M. Käll, T. Shegai, Realizing Strong Light-Matter Interactions between Single-Nanoparticle Plasmons and Molecular Excitons at Ambient Conditions, Physical Review Letters **114**(15), 157401 (2015), https://doi.org/10.1103/PhysRevLett.114.157401.

[67] A. I. Väkeväinen, R. J. Moerland, H. T. Rekola, A.-P. Eskelinen, J.-P. Martikainen, D.-H. Kim, P. Törmä, Plasmonic Surface Lattice Resonances at the Strong Coupling Regime, Nano Letters **14**(4), 1721–1727 (2014), https://doi.org/10.1021/nl4035219.

[68] G. Khitrova, H. M. Gibbs, M. Kira, S. W. Koch, A. Scherer, Vacuum Rabi splitting in semiconductors, Nature Physics **2**(2), 81–90 (2006), https://doi.org/10.1038/nphys227.

[69] X. Yu, Y. Yuan, J. Xu, K. Yong, J. Qu, J. Song, Strong Coupling in Microcavity Structures: Principle, Design, and Practical Application, Laser & Photonics Reviews **13**(1), 1800219 (2019), https://doi.org/10.1002/lpor.201800219.

[70] A. Reiserer, G. Rempe, Cavity-based quantum networks with single atoms and optical photons, Reviews of Modern Physics **87**(4), 1379–1418 (2015), https://doi.org/10.1103/RevModPhys.87.1379.

[71] R. Ameling, H. Giessen, Microcavity plasmonics: strong coupling of photonic cavities and plasmons, Laser & Photonics Reviews **7**(2), 141–169 (2013), https://doi.org/10.1002/lpor.201100041.

[72] A. Ghoshal, P. G. Kik, Theory and simulation of surface plasmon excitation using resonant metal nanoparticle arrays, Journal of Applied Physics **103**(11), 113111 (2008), https://doi.org/10.1063/1.2936971.

[73] X. Xu, S. Jin, Strong coupling of single quantum dots with low-refractive-index/high-refractive-index materials at room temperature, Science Advances **6**(47), eabb3095 (2020), https://doi.org/10.1126/sciadv.abb3095.

[74] H. Leng, B. Szychowski, M.-C. Daniel, M. Pelton, Strong coupling and induced transparency at room temperature with single quantum dots and gap plasmons, Nature Communications **9**(1), 4012, number: 1 (2018), https://doi.org/10.1038/s41467-018-06450-4.

[75] T. K. Hakala, A. J. Moilanen, A. I. Väkeväinen, R. Guo, J.-P. Martikainen, K. S. Daskalakis, H. T. Rekola, A. Julku, P. Törmä, Bose–Einstein condensation in a plasmonic lattice, Nature Physics **14**(7), 739–744 (2018), https://doi.org/10.1038/s41567-018-0109-9.

[76] R. Su, C. Diederichs, J. Wang, T. C. H. Liew, J. Zhao, S. Liu, W. Xu, Z. Chen, Q. Xiong, Room-Temperature Polariton Lasing in All-Inorganic Perovskite Nanoplatelets, Nano Letters **17**(6), 3982–3988 (2017), https://doi.org/10.1021/acs.nanolett.7b01956.

[77] P. R. Rice, H. J. Carmichael, Photon statistics of a cavity-QED laser: A comment on the laser–phase-transition analogy, Physical Review A **50**(5), 4318–4329 (1994), https://doi.org/10.1103/PhysRevA.50.4318.

[78] S. Ghosh, R. Su, J. Zhao, A. Fieramosca, J. Wu, T. Li, Q. Zhang, F. Li, Z. Chen, T. Liew, D. Sanvitto, Q. Xiong, Microcavity exciton polaritons at room temperature, Photonics Insights **1**(1), R04, number: 1 (2022), https://doi.org/10.3788/PI.2022.R04.

[79] R. H. Dicke, Coherence in Spontaneous Radiation Processes, Physical Review **93**(1), 99–110 (1954), https://doi.org/10.1103/PhysRev.93.99.

[80] J. J. Hopfield, Theory of the Contribution of Excitons to the Complex Dielectric Constant of Crystals, Physical Review **112**(5), 1555–1567 (1958), https://doi.org/10.1103/PhysRev.112.1555.

[81] J. Mony, M. Hertzog, K. Kushwaha, K. Börjesson, Angle-Independent Polariton Emission Lifetime Shown by Perylene Hybridized to the Vacuum Field Inside a Fabry–Pérot Cavity, The Journal of Physical Chemistry C **122**(43), 24917–24923, number: 43 (2018), https://doi.org/10.1021/acs.jpcc.8b07283.

[82] D. G. Lidzey, A. M. Fox, M. D. Rahn, M. S. Skolnick, V. M. Agranovich, S. Walker, Experimental study of light emission from strongly coupled organic semiconductor microcavities following nonresonant laser excitation, Physical Review B **65**(19), 195312, number: 19 (2002), https://doi.org/10.1103/PhysRevB.65.195312.

[83] H. Chen, J. Ai, X. Bai, S. Hou, S. R. Forrest, J. P. Ogilvie, Y. Song, Tracking relaxation dynamics of polaritons and reservoir states in organic exciton-polaritons, The Journal of Physical Chemistry Letters **16**(21), 5265–5271, pMID: 40387196 (2025), https://doi.org/10.1021/acs.jpclett.5c00666.

[84] R. Bhuyan, M. Lednev, J. Feist, K. Börjesson, The effect of the relative size of the exciton reservoir on polariton photophysics, Advanced Optical Materials **12**(2), 2301383 (2024), https://doi.org/https://doi.org/10.1002/adom.202301383.

[85] I. Sokolovskii, R. H. Tichauer, D. Morozov, J. Feist, G. Groenhof, Multiscale molecular dynamics simulations of enhanced energy transfer in organic molecules under strong coupling, Nature Communications **14**(1), 6613 (2023), https://doi.org/10.1038/s41467-023-42067-y.

[86] D. Dovzhenko, M. Lednev, K. Mochalov, I. Vaskan, Y. Rakovich, A. Karaulov, I. Nabiev, Polariton-assisted manipulation of energy relaxation pathways: donor–acceptor role reversal in a tuneable microcavity, Chemical Science **12**(38), 12794–12805 (2021), https://doi.org/10.1039/D1SC02026A.

[87] M. Park, S. Koniakhin, S. Choi, D. Choi, S. I. Park, S. Y. L. Park, J. D. Song, Y.-H. Cho, H. Choi, Exciton reservoir-induced destabilization and

reformation of polariton condensate, Opt. Express **33**(8), 18530–18539 (2025), https://doi.org/10.1364/OE.553836.

[88] A. González-Tudela, P. A. Huidobro, L. Martín-Moreno, C. Tejedor, F. J. García-Vidal, Theory of Strong Coupling between Quantum Emitters and Propagating Surface Plasmons, Physical Review Letters **110**(12), 126801, number: 12 (2013), https://doi.org/10.1103/PhysRevLett.110.126801.

[89] M. S. Tame, K. R. McEnery, K. Özdemir, J. Lee, S. A. Maier, M. S. Kim, Quantum plasmonics, Nature Physics **9**(6), 329–340, number: 6 (2013), https://doi.org/10.1038/nphys2615.

[90] R. Datta, T. M. Heaster, J. T. Sharick, A. A. Gillette, M. C. Skala, Fluorescence lifetime imaging microscopy: fundamentals and advances in instrumentation, analysis, and applications, Journal of Biomedical Optics **25**(07), 1 (2020), https://doi.org/10.1117/1.JBO.25.7.071203.

[91] D. J. Griffiths, D. F. Schroeter, *Introduction to Quantum Mechanics* (Cambridge University Press, 2018), 3 edition.

[92] G. M. Akselrod, C. Argyropoulos, T. B. Hoang, C. Ciracì, C. Fang, J. Huang, D. R. Smith, M. H. Mikkelsen, Probing the mechanisms of large Purcell enhancement in plasmonic nanoantennas, Nature Photonics **8**(11), 835–840, number: 11 (2014), https://doi.org/10.1038/nphoton.2014.228.

[93] W. Zhou, J. Liu, J. Zhu, D. Gromyko, C. Qiu, L. Wu, Exceptional points unveiling quantum limit of fluorescence rates in non-Hermitian plexcitonic single-photon sources, APL Quantum **1**(1), 016110, number: 1 (2024), https://doi.org/10.1063/5.0191494.

[94] P. Vasa, C. Lienau, Strong Light–Matter Interaction in Quantum Emitter/Metal Hybrid Nanostructures, ACS Photonics **5**(1), 2–23 (2018), https://doi.org/10.1021/acsphotonics.7b00650.

[95] K. H. Drexhage, IV Interaction of Light with Monomolecular Dye Layers, in *Progress in Optics* (Elsevier, 1974), volume 12, 163–232.

[96] W. Becker, A. Bergmann, G. L. Biscotti, A. Rueck, Advanced time-correlated single photon counting techniques for spectroscopy and imaging in biomedical systems (San Jose, Ca, 2004), 104.

[97] P. Wang, J. Liang, L. V. Wang, Single-shot ultrafast imaging attaining 70 trillion frames per second, Nature Communications **11**(1), 2091 (2020), https://doi.org/10.1038/s41467-020-15745-4.

[98] L. Scipioni, A. Rossetta, G. Tedeschi, E. Gratton, Phasor S-FLIM: a new paradigm for fast and robust spectral fluorescence lifetime imaging, Nature Methods **18**(5), 542–550 (2021), https://doi.org/10.1038/s41592-021-01108-4.

[99] H. C. Gerritsen, M. A. H. Asselbergs, A. V. Agronskaia, W. G. J. H. M. Van Sark, Fluorescence lifetime imaging in scanning microscopes: acquisition speed, photon economy and lifetime resolution, Journal of Microscopy **206**(3), 218–224 (2002), https://doi.org/10.1046/j.1365-2818.2002.01031.x.

[100] A. Lyons, V. Zickus, R. Álvarez Mendoza, D. Triggiani, V. Tamma, N. Westerberg, M. Tassieri, D. Faccio, Fluorescence lifetime Hong-Ou-Mandel sensing, Nature Communications **14**(1), 8005, number: 1 (2023), https://doi.org/10.1038/s41467-023-43868-x.

[101] B. Torrado, B. Pannunzio, L. Malacrida, M. A. Digman, Fluorescence lifetime imaging microscopy, Nature Reviews Methods Primers **4**(1), 80 (2024), https://doi.org/10.1038/s43586-024-00358-8.

[102] V. I. Shcheslavskiy, M. V. Shirmanova, K. S. Yashin, A. C. Rück, M. C. Skala, W. Becker, Fluorescence Lifetime Imaging Techniques—A Review on Principles, Applications and Clinical Relevance, Journal of Biophotonics e202400450 (2025), https://doi.org/10.1002/jbio.202400450.

[103] V. Zickus, M.-L. Wu, K. Morimoto, V. Kapitany, A. Fatima, A. Turpin, R. Insall, J. Whitelaw, L. Machesky, C. Bruschini, D. Faccio, E. Charbon, Fluorescence lifetime imaging with a megapixel SPAD camera and neural network lifetime estimation, Scientific Reports **10**(1), 20986 (2020), https://doi.org/10.1038/s41598-020-77737-0.

[104] M. W. Davidson, M. Abramowitz, Optical Microscopy, in J. P. Hornak (ed.), *Encyclopedia of Imaging Science and Technology* (Wiley, 2002), 1 edition.

[105] S. W. Hell, J. Wichmann, Breaking the diffraction resolution limit by stimulated emission: stimulated-emission-depletion fluorescence microscopy, Optics Letters **19**(11), 780 (1994), https://doi.org/10.1364/OL.19.000780.

[106] E. Betzig, G. H. Patterson, R. Sougrat, O. W. Lindwasser, S. Olenych, J. S. Bonifacino, M. W. Davidson, J. Lippincott-Schwartz, H. F. Hess, Imaging Intracellular Fluorescent Proteins at Nanometer Resolution, Science **313**(5793), 1642–1645 (2006), https://doi.org/10.1126/science.1127344.

[107] Y. M. Sigal, R. Zhou, X. Zhuang, Visualizing and discovering cellular structures with super-resolution microscopy, Science **361**(6405), 880–887 (2018), https://doi.org/10.1126/science.aau1044.

[108] P. F. Gao, G. Lei, C. Z. Huang, Dark-Field Microscopy: Recent Advances in Accurate Analysis and Emerging Applications, Analytical Chemistry **93**(11), 4707–4726 (2021), https://doi.org/10.1021/acs.analchem.0c04390.

[109] A. Ji, J.-H. Song, Q. Li, F. Xu, C.-T. Tsai, R. C. Tiberio, B. Cui, P. Lalanne, P. G. Kik, D. A. B. Miller, M. L.

Brongersma, Quantitative phase contrast imaging with a nonlocal angle-selective metasurface, Nature Communications **13**(1), 7848 (2022), https://doi.org/10.1038/s41467-022-34197-6.

[110] J. Jonkman, C. M. Brown, G. D. Wright, K. I. Anderson, A. J. North, Tutorial: guidance for quantitative confocal microscopy, Nature Protocols **15**(5), 1585–1611 (2020), https://doi.org/10.1038/s41596-020-0313-9.

[111] A. D. Elliott, Confocal Microscopy: Principles and Modern Practices, Current Protocols in Cytometry **92**(1), e68 (2020), https://doi.org/10.1002/cpcy.68.

[112] R. M. Power, J. Huisken, A guide to light-sheet fluorescence microscopy for multiscale imaging, Nature Methods **14**(4), 360–373 (2017), https://doi.org/10.1038/nmeth.4224.

[113] W. R. Zipfel, R. M. Williams, W. W. Webb, Nonlinear magic: multiphoton microscopy in the biosciences, Nature Biotechnology **21**(11), 1369–1377 (2003), https://doi.org/10.1038/nbt899.

[114] A. M. Larson, Multiphoton microscopy, Nature Photonics **5**(1), 1–1 (2011), https://doi.org/10.1038/nphoton.an.2010.2.

[115] G. Pariente, V. Gallet, A. Borot, O. Gobert, F. Quéré, Space–time characterization of ultra-intense femtosecond laser beams, Nature Photonics **10**(8), 547–553 (2016), https://doi.org/10.1038/nphoton.2016.140.

[116] S. Cueff, L. Berguiga, H. S. Nguyen, Fourier imaging for nanophotonics, Nanophotonics **13**(6), 841–858 (2024), https://doi.org/10.1515/nanoph-2023-0887.

[117] J. W. Lichtman, J.-A. Conchello, Fluorescence microscopy, Nature Methods **2**(12), 910–919 (2005), https://doi.org/10.1038/nmeth817.

[118] Y. Chen, D. Zhang, D. Qiu, L. Zhu, S. Yu, P. Yao, P. Wang, H. Ming, R. Badugu, J. R. Lakowicz, Back focal plane imaging of Tamm plasmons and their coupled emission, Laser & Photonics Reviews **8**(6), 933–940, number: 6 _eprint: https://onlinelibrary.wiley.com/doi/pdf/10.1002/lpor.201400117 (2014), https://doi.org/10.1002/lpor.201400117.

[119] A. S. Backer, W. E. Moerner, Extending Single-Molecule Microscopy Using Optical Fourier Processing, The Journal of Physical Chemistry B **118**(28), 8313–8329 (2014), https://doi.org/10.1021/jp501778z.

[120] R. Scott, J. Heckmann, A. V. Prudnikau, A. Antanovich, A. Mikhailov, N. Owschimikow, M. Artemyev, J. I. Climente, U. Woggon, N. B. Grosse, A. W. Achtstein, Directed emission of CdSe nanoplatelets originating from strongly anisotropic 2D electronic structure, Nature Nanotechnology **12**(12), 1155–1160 (2017), https://doi.org/10.1038/nnano.2017.177.

[121] L. Sigl, M. Troue, M. Katzer, M. Selig, F. Sigger, J. Kiemle, M. Brotons-Gisbert, K. Watanabe, T. Taniguchi, B. D. Gerardot, A. Knorr, U. Wurstbauer, A. W. Holleitner, Optical dipole orientation of interlayer excitons in MoSe 2 WSe 2 heterostacks, Physical Review B **105**(3), 035417 (2022), https://doi.org/10.1103/PhysRevB.105.035417.

[122] C. F. Bohren, D. R. Huffman, *Absorption and scattering of light by small particles* (Wiley, New York, 1983).

[123] A. Genco, C. Cruciano, M. Corti, K. E. McGhee, B. Ardini, L. Sortino, L. Hüttenhofer, T. Virgili, D. G. Lidzey, S. A. Maier, A. Bassi, G. Valentini, G. Cerullo, C. Manzoni, k -Space Hyperspectral Imaging by a Birefringent Common-Path Interferometer, ACS Photonics **9**(11), 3563–3572 (2022), https://doi.org/10.1021/acsphotonics.2c00959.

[124] D. Axelrod, Total Internal Reflection Fluorescence Microscopy in Cell Biology, Traffic **2**(11), 764–774 (2001), https://doi.org/10.1034/j.1600-0854.2001.21104.x.

[125] R. M. A. Azzam, N. M. Bashara, *Ellipsometry and polarized ligth* (North-Holland, 1989).

[126] B. Gao, J. P. George, J. Beeckman, K. Neyts, Design, fabrication and characterization of a distributed Bragg reflector for reducing the étendue of a wavelength converting system, Optics Express **28**(9), 12837 (2020), https://doi.org/10.1364/OE.391080.

[127] J. Xie, D. Zhang, X.-Q. Yan, M. Ren, X. Zhao, F. Liu, R. Sun, X. Li, Z. Li, S. Chen, Z.-B. Liu, J.-G. Tian, Optical properties of chemical vapor deposition-grown $PtSe_2$ characterized by spectroscopic ellipsometry, 2D Materials **6**(3), 035011 (2019), https://doi.org/10.1088/2053-1583/ab1490.

[128] H. G. Tompkins, E. A. Irene (eds.), *Handbook of ellipsometry* (William Andrew Pub. ; Springer, Norwich, NY : Heidelberg, Germany, 2005).

[129] J. A. Woollam, P. G. Snyder, *Variable Angle Spectroscopic Ellipsometry* (Boston: Buttrerworth-Heinemann, 1992).

[130] H. Arwin, M. Poksinski, K. Johansen, Total internal reflection ellipsometry: principles and applications, Applied Optics **43**(15), 3028 (2004), https://doi.org/10.1364/AO.43.003028.

[131] A. Nabok, A. Tsargorodskaya, The method of total internal reflection ellipsometry for thin film characterisation and sensing, Thin Solid Films **516**(24), 8993–9001 (2008), https://doi.org/10.1016/j.tsf.2007.11.077.

[132] V. M. Agranovich, D. L. Mills, *Surface polaritons: electromagnetic waves at surfaces and interfaces. in Modern problems in condensed matter sciences* (Elsevier Science Pub. Co, 1982).

[133] A. Nooke, U. Beck, A. Hertwig, A. Krause, H. Krüger, V. Lohse, D. Negendank, J. Steinbach, On the application of gold based SPR sensors for the detection of hazardous gases, Sensors and Actuators B: Chemical **149**(1), 194–198, number: 1 (2010), https://doi.org/10.1016/j.snb.2010.05.061.

[134] K. R. Spencer, J. Wang, A. W. Silk, S. Ganesan, H. L. Kaufman, J. M. Mehnert, Biomarkers for Immunotherapy: Current Developments and Challenges, American Society of Clinical Oncology Educational Book (36), e493–e503, number: 36 (2016), https://doi.org/10.1200/EDBK$_1$60766.

[135] S. Guo, Y. Li, R. Li, P. Zhang, Y. Wang, S. C. Gopinath, K. Gong, P. Wan, High-performance detection of an abdominal aortic aneurysm biomarker by immunosensing, Biotechnology and Applied Biochemistry bab.1877 (2020), https://doi.org/10.1002/bab.1877.

[136] M.-I. Mohammed, M. P. Y. Desmulliez, Lab-on-a-chip based immunosensor principles and technologies for the detection of cardiac biomarkers: a review, Lab Chip **11**(4), 569–595, number: 4 (2011), https://doi.org/10.1039/C0LC00204F.

[137] B. Li, H. Tan, D. Jenkins, V. Srinivasa Raghavan, B. G. Rosa, F. Güder, G. Pan, E. Yeatman, D. J. Sharp, Clinical detection of neurodegenerative blood biomarkers using graphene immunosensor, Carbon **168**, 144–162 (2020), https://doi.org/10.1016/j.carbon.2020.06.048.

[138] G. Sabatté, R. Keir, M. Lawlor, M. Black, D. Graham, W. E. Smith, Comparison of Surface-Enhanced Resonance Raman Scattering and Fluorescence for Detection of a Labeled Antibody, Analytical Chemistry **80**(7), 2351–2356, number: 7 (2008), https://doi.org/10.1021/ac071343j.

[139] A. Diaspro, G. Chirico, C. Usai, P. Ramoino, J. Dobrucki, Photobleaching, in J. B. Pawley (ed.), *Handbook Of Biological Confocal Microscopy* (Springer US, Boston, MA, 2006), 690–702.

[140] M. Soler, M.-C. Estevez, M. Alvarez, M. Otte, B. Sepulveda, L. Lechuga, Direct Detection of Protein Biomarkers in Human Fluids Using Site-Specific Antibody Immobilization Strategies, Sensors **14**(2), 2239–2258, number: 2 (2014), https://doi.org/10.3390/s140202239.

[141] J. Pultar, U. Sauer, P. Domnanich, C. Preininger, Aptamer–antibody on-chip sandwich immunoassay for detection of CRP in spiked serum, Biosensors and Bioelectronics **24**(5), 1456–1461, number: 5 (2009), https://doi.org/10.1016/j.bios.2008.08.052.

[142] J. V. Jun, D. M. Chenoweth, E. J. Petersson, Rational design of small molecule fluorescent probes for biological applications, Organic & Biomolecular Chemistry **18**(30), 5747–5763, number: 30 (2020), https://doi.org/10.1039/D0OB01131B.

[143] I. Rasnik, S. A. McKinney, T. Ha, Nonblinking and long-lasting single-molecule fluorescence imaging, Nature Methods **3**(11), 891–893, number: 11 (2006), https://doi.org/10.1038/nmeth934.

[144] B. Liu, Y. Li, H. Wan, L. Wang, W. Xu, S. Zhu, Y. Liang, B. Zhang, J. Lou, H. Dai, K. Qian, High Performance, Multiplexed Lung Cancer Biomarker Detection on a Plasmonic Gold Chip, Advanced Functional Materials **26**(44), 7994–8002, number: 44 (2016), https://doi.org/10.1002/adfm.201603547.

[145] S. Kéna-Cohen, A. Wiener, Y. Sivan, P. N. Stavrinou, D. D. C. Bradley, A. Horsfield, S. A. Maier, Plasmonic Sinks for the Selective Removal of Long-Lived States, ACS Nano **5**(12), 9958–9965, number: 12 (2011), https://doi.org/10.1021/nn203754v.

[146] H. Nguyen, J. Park, S. Kang, M. Kim, Surface Plasmon Resonance: A Versatile Technique for Biosensor Applications, Sensors **15**(5), 10481–10510, number: 5 (2015), https://doi.org/10.3390/s150510481.

[147] I. Plikusiene, Z. Balevicius, A. Ramanaviciene, J. Talbot, G. Mickiene, S. Balevicius, A. Stirke, A. Tereshchenko, L. Tamosaitis, G. Zvirblis, A. Ramanavicius, Evaluation of affinity sensor response kinetics towards dimeric ligands linked with spacers of different rigidity: Immobilized recombinant granulocyte colony-stimulating factor based synthetic receptor binding with genetically engineered dimeric analyte derivatives, Biosensors and Bioelectronics **156**, 112112 (2020), https://doi.org/10.1016/j.bios.2020.112112.

[148] J. A. De Feijter, J. Benjamins, F. A. Veer, Ellipsometry as a tool to study the adsorption behavior of synthetic and biopolymers at the air-water interface, Biopolymers **17**(7), 1759–1772, number: 7 (1978), https://doi.org/10.1002/bip.1978.360170711.

[149] J. Anulytė, E. Bužavaitė-Vertelienė, V. Vertelis, E. Stankevičius, K. Vilkevičius, Z. Balevičius, Influence of a gold nano-bumps surface lattice array on the propagation length of strongly coupled Tamm and surface plasmon polaritons, Journal of Materials Chemistry C **10**(36), 13234–13241, number: 36 (2022), https://doi.org/10.1039/D2TC02174A.

[150] E. Buzavaite-Verteliene, I. Plikusiene, T. Tolenis, A. Valavicius, J. Anulyte, A. Ramanavicius, Z. Balevicius, Hybrid Tamm-surface plasmon polariton mode for highly sensitive detection of protein interactions, Optics Express **28**(20), 29033, number: 20 (2020), https://doi.org/10.1364/OE.401802.

[151] A. Paulauskas, S. Tumenas, A. Selskis, T. Tolenis, A. Valavicius, Z. Balevicius, Hybrid Tamm-surface plasmon polaritons mode for detection of mercury adsorption on 1D photonic crystal/gold nanostructures by total internal reflection ellipsometry, Optics Express **26**(23), 30400, number: 23 (2018), https://doi.org/10.1364/OE.26.030400.

[152] J. Anulytė, E. Bužavaitė-Vertelienė, E. Stankevičius, K. Vilkevičius, Z. Balevičius, High Spectral Sensitivity of Strongly Coupled Hybrid Tamm-Plasmonic Resonances for Biosensing Application, Sensors **22**(23), 9453, number: 23 (2022), https://doi.org/10.3390/s22239453.

[153] E. Bužavaitė-Vertelienė, V. Vertelis, Z. Balevičius, The experimental evidence of a strong coupling regime in the hybrid Tamm plasmon-surface plasmon polariton mode, Nanophotonics **10**(5), 1565–1571, number: 5 (2021), https://doi.org/10.1515/nanoph-2020-0660.

[154] J. Galego, F. J. Garcia-Vidal, J. Feist, Suppressing photochemical reactions with quantized light fields, Nature Communications **7**(1), 13841, number: 1 (2016), https://doi.org/10.1038/ncomms13841.

[155] N. Kongsuwan, X. Xiong, P. Bai, J.-B. You, C. E. Png, L. Wu, O. Hess, Quantum Plasmonic Immunoassay Sensing, Nano Letters **19**(9), 5853–5861, number: 9 (2019), https://doi.org/10.1021/acs.nanolett.9b01137.

[156] Z. Balevicius, A. Makaraviciute, G.-J. Babonas, S. Tumenas, V. Bukauskas, A. Ramanaviciene, A. Ramanavicius, Study of optical anisotropy in thin molecular layers by total internal reflection ellipsometry, Sensors and Actuators B: Chemical **181**, 119–124 (2013), https://doi.org/10.1016/j.snb.2013.01.059.

[157] Thermo fisher scientific alexa fluor® 633 (catalog num. a20005), https://www.thermofisher.com/order/catalog/product/A20005, accessed: 20 December 2022 (2022).

[158] S. Tan, A. Argondizzo, J. Ren, L. Liu, J. Zhao, H. Petek, Plasmonic coupling at a metal/semiconductor interface, Nature Photonics **11**(12), 806–812 (2017), https://doi.org/10.1038/s41566-017-0049-4.

[159] K. A. Willets, A. J. Wilson, V. Sundaresan, P. B. Joshi, Super-Resolution Imaging and Plasmonics, Chemical Reviews **117**(11), 7538–7582 (2017), https://doi.org/10.1021/acs.chemrev.6b00547.

[160] F. Wei, D. Lu, H. Shen, W. Wan, J. L. Ponsetto, E. Huang, Z. Liu, Wide Field Super-Resolution Surface Imaging through Plasmonic Structured Illumination Microscopy, Nano Letters **14**(8), 4634–4639, number: 8 Publisher: American Chemical Society (2014), https://doi.org/10.1021/nl501695c.

[161] F. Freire-Fernández, S.-M. Park, M. J. H. Tan, T. W. Odom, Plasmonic lattice lasers, Nature Reviews Materials **10**(8), 604–616 (2025), https://doi.org/10.1038/s41578-025-00803-4.

[162] T. K. Hakala, H. T. Rekola, A. I. Väkeväinen, J.-P. Martikainen, M. Nečada, A. J. Moilanen, P. Törmä, Lasing in dark and bright modes of a finite-sized plasmonic lattice, Nature Communications **8**(1), 13687 (2017), https://doi.org/10.1038/ncomms13687.

[163] T. K. Hakala, J. J. Toppari, A. Kuzyk, M. Pettersson, H. Tikkanen, H. Kunttu, P. Törmä, Vacuum Rabi Splitting and Strong-Coupling Dynamics for Surface-Plasmon Polaritons and Rhodamine 6G Molecules, Physical Review Letters **103**(5), 053602 (2009), https://doi.org/10.1103/PhysRevLett.103.053602.

[164] P. Jurkšaitis, E. Bužavaitė-Vertelienė, Z. Balevičius, Strong Coupling between Surface Plasmon Resonance and Exciton of Labeled Protein–Dye Complex for Immunosensing Applications, International Journal of Molecular Sciences **24**(3), 2029, number: 3 (2023), https://doi.org/10.3390/ijms24032029.

[165] S. Kéna-Cohen, S. A. Maier, D. D. C. Bradley, Ultrastrongly Coupled Exciton–Polaritons in Metal-Clad Organic Semiconductor Microcavities, Advanced Optical Materials **1**(11), 827–833 (2013), https://doi.org/10.1002/adom.201300256.

[166] W. Wang, P. Vasa, R. Pomraenke, R. Vogelgesang, A. De Sio, E. Sommer, M. Maiuri, C. Manzoni, G. Cerullo, C. Lienau, Interplay between Strong Coupling and Radiative Damping of Excitons and Surface Plasmon Polaritons in Hybrid Nanostructures, ACS Nano **8**(1), 1056–1064 (2014), https://doi.org/10.1021/nn405981k.

[167] P. A. Hobson, W. L. Barnes, D. G. Lidzey, G. A. Gehring, D. M. Whittaker, M. S. Skolnick, S. Walker, Strong exciton–photon coupling in a low-Q all-metal mirror microcavity, Applied Physics Letters **81**(19), 3519–3521, number: 19 (2002), https://doi.org/10.1063/1.1517714.

[168] T. Schwartz, J. A. Hutchison, J. Léonard, C. Genet, S. Haacke, T. W. Ebbesen, Polariton Dynamics under Strong Light–Molecule Coupling, ChemPhysChem **14**(1), 125–131 (2013), https://doi.org/10.1002/cphc.201200734.

[169] S. V. Baieva, T. K. Hakala, J. J. Toppari, Strong coupling between surface plasmon polaritons and Sulforhodamine 101 dye, Nanoscale Research Letters **7**(1), 191 (2012), https://doi.org/10.1186/1556-276X-7-191.

[170] R. Alfano, S. Shapiro, W. Yu, Effect of soap on the fluorescent lifetime and quantum yield of rhodamine 6G in water, Optics Communications **7**(3), 191–192 (1973), https://doi.org/10.1016/0030-4018(73)90007-2.

[171] Y. Nishijima, S. Morimoto, A. Balčytis, T. Hashizume, R. Matsubara, A. Kubono, N. To, M. Ryu, J. Morikawa, S. Juodkazis, Coupling of molecular vibration and metasurface modes for efficient mid-infrared emission, Journal of Materials Chemistry C **10**(2), 451–462 (2022), https://doi.org/10.1039/D1TC04519A.

[172] G. Di Martino, Y. Sonnefraud, M. Tame, S. Kéna-Cohen, F. Dieleman, Özdemir, M. Kim, S. Maier, Observation of Quantum Interference in the Plasmonic Hong-Ou-Mandel Effect, Physical Review Applied **1**(3), 034004 (2014), https://doi.org/10.1103/PhysRevApplied.1.034004.

[173] S. Kreinberg, T. Grbešić, M. Strauß, A. Carmele, M. Emmerling, C. Schneider, S. Höfling, X. Porte, S. Reitzenstein, Quantum-optical spectroscopy of a two-level system using an electrically driven micropillar laser as a resonant excitation source, Light: Science & Applications **7**(1), 41, number: 1 (2018), https://doi.org/10.1038/s41377-018-0045-6.

[174] L. Huang, L. Xu, M. Woolley, A. E. Miroshnichenko, Trends in Quantum Nanophotonics, Advanced Quantum Technologies **3**(4), 1900126 (2020), https://doi.org/10.1002/qute.201900126.

[175] S. R. Marschner, S. H. Westin, E. P. F. Lafortune, K. E. Torrance, Image-based bidirectional reflectance distribution function measurement, Applied Optics **39**(16), 2592 (2000), https://doi.org/10.1364/AO.39.002592.

[176] Y. Wang, T. Yang, M. T. Tuominen, M. Achermann, Radiative Rate Enhancements in Ensembles of Hybrid Metal-Semiconductor Nanostructures, Physical Review Letters **102**(16), 163001 (2009), https://doi.org/10.1103/PhysRevLett.102.163001.

[177] T. Hinamoto, M. Hamada, H. Sugimoto, M. Fujii, Angle-, Polarization-, and Wavelength-Resolved Light Scattering of Single Mie Resonators Using Fourier-Plane Spectroscopy, Advanced Optical Materials **9**(8), 2002192 (2021), https://doi.org/10.1002/adom.202002192.

[178] C. Seo, J.-E. Shim, C. Kim, E. Lee, G. H. Choi, P. J. Yoo, G.-R. Yi, J. Kim, T.-T. Kim, Back-focal plane scanning spectroscopy for investigating the optical dispersion of large-area two-dimensional photonic crystal fabricated by capillary force lithography, Current Applied Physics **65**, 47–52 (2024), https://doi.org/10.1016/j.cap.2024.06.001.

[179] N. H. M. Dang, S. Zanotti, E. Drouard, C. Chevalier, G. Trippé-Allard, M. Amara, E. Deleporte, V. Ardizzone, D. Sanvitto, L. C. Andreani, C. Seassal, D. Gerace, H. S. Nguyen, Realization of Polaritonic Topological Charge at Room Temperature Using Polariton Bound States in the Continuum from Perovskite Metasurface, Advanced Optical Materials **10**(6), 2102386 (2022), https://doi.org/10.1002/adom.202102386.

[180] E. Engay, D. Huo, R. Malureanu, A.-I. Bunea, A. Lavrinenko, Polarization-Dependent All-Dielectric Metasurface for Single-Shot Quantitative Phase Imaging, Nano Letters **21**(9), 3820–3826 (2021), https://doi.org/10.1021/acs.nanolett.1c00190.

[181] H. Zhao, C. Wang, C. Lyu, X. Zhao, B. Sun, Y. Gao, Efficient Lasing Enabled by Enhanced Light-Matter Interaction through Aligned Nanoplatelets in Resonators, ACS Photonics **11**(11), 4559–4566 (2024), https://doi.org/10.1021/acsphotonics.4c00807.

[182] R. A. DeCrescent, S. J. Brown, R. A. Schlitz, M. L. Chabinyc, J. A. Schuller, Model-blind characterization of thin-film optical constants with momentum-resolved reflectometry, Optics Express **24**(25), 28842 (2016), https://doi.org/10.1364/OE.24.028842.

[183] Y. Su, H. Lu, D. Li, C. Wang, J. Zhao, Strong photoluminescence enhancement from a WS_2 atomic layer integrated on a metallic nanogroove array with intermediate plasmon–exciton coupling, Photonics Research **12**(12), 3006 (2024), https://doi.org/10.1364/PRJ.537939.

[184] A. P. Manuel, A. Kirkey, N. Mahdi, K. Shankar, Plexcitonics – fundamental principles and optoelectronic applications, Journal of Materials Chemistry C **7**(7), 1821–1853 (2019), https://doi.org/10.1039/C8TC05054F.

[185] J. Wang, Y. Zhai, X. Pan, L. Xu, Z. Li, S. Cao, Y. Li, Surface Plasmon Coupled Directional Emission for Integrated Fluorescence-Raman Biodetection: A Proof-of-Concept Study, Chemistry–Methods **2**(6), e202100089, number: 6 (2022), https://doi.org/10.1002/cmtd.202100089.

[186] J. A. Hutchison, T. Schwartz, C. Genet, E. Devaux, T. W. Ebbesen, Modifying Chemical Landscapes by Coupling to Vacuum Fields, Angewandte Chemie International Edition **51**(7), 1592–1596, number: 7 (2012), https://doi.org/10.1002/anie.201107033.

[187] L. Novotny, Strong coupling, energy splitting, and level crossings: A classical perspective, American Journal of Physics **78**(11), 1199–1202, number: 11 (2010), https://doi.org/10.1119/1.3471177.

[188] F. Schlawin, D. M. Kennes, M. A. Sentef, Cavity quantum materials, Applied Physics Reviews **9**(1), 011312, number: 1 (2022), https://doi.org/10.1063/5.0083825.

[189] D. C. Gold, P. Huft, C. Young, A. Safari, T. G. Walker, M. Saffman, D. D. Yavuz, Spatial Coherence of Light in Collective Spontaneous Emission, PRX Quantum **3**(1), 010338 (2022), https://doi.org/10.1103/PRXQuantum.3.010338.

[190] M. Dowran, A. Butler, S. Lamichhane, A. Erickson, U. Kilic, S. Liou, C. Argyropoulos, A. Laraoui, Plasmon Enhanced Quantum Properties of Single Photon Emitters with Hybrid Hexagonal Boron Nitride Silver Nanocube Systems, Advanced Optical Materials **11**(16), 2300392 (2023), https://doi.org/10.1002/adom.202300392.

[191] O. Mollet, S. Huant, G. Dantelle, T. Gacoin, A. Drezet, Quantum plasmonics: Second-order coherence of surface plasmons launched by quantum emitters into a metallic film, Physical Review B **86**(4), 045401 (2012), https://doi.org/10.1103/PhysRevB.86.045401.

TRUMPOS ŽINIOS APIE AUTORIŲ

Vardas: Povilas

Pavardė: Jurkšaitis

El. paštas: povilas.jurksaitis@ftmc.lt

Išsilavinimas:

2021 – 2025	Vilniaus universitetas, Fizikos fakultetas bei Fizinių ir technologijos mokslų centras. *Doktorantūros studijos.*
2016 – 2018	Vilniaus universitetas, Fizikos fakultetas. *Lazerių fizikos magistro laipsnis.*
2015/02 – 2015/06	Bilkento universitetas, Turkija. Fizikos fakultetas. *Erasmus mainų programa.*
2012 – 2016	Kauno technologijos universitetas, Matematikos ir gamtos mokslų fakultetas. *Fizikos bakalauro laipsnis.*

Profesinė veikla:

2022/11 – dabar	FTMC, Plazmonikos ir nanofotonikos laboratorija. *Jaunesnysis mokslo darbuotojas.*
2019/04 – 2022/08	EKSPLA. *Inžinierius.*
2018/06 – 2019/03	BROLIS Semiconductors. *Inžinierius.*
2016/02 – 2018/06	FTMC, Optinių dangų laboratorija. *Technikas.*

Profesinės išvykos:

2023/09 – 2023/12 Ekstremalios šviesos grupė, prof. dr. Danielle Faccio *Glazgo universitetas.*

Apdovanojimai: „SPIE Global Early Career Researcher Accelerator Fund In Quantum Photonics“ 8000 svarų sterlingų dotacija, skirta remti pradedančiųjų tyrėjų mainų programai Glazgo universitete.

NOTES

NOTES

NOTES

Vilnius University Press
Saulėtekio Ave. 9, LT-10222 Vilnius
e-mail: info@leidykla.vu.lt, www.leidykla.vu.lt
bookshop.vu.lt, journals.vu.lt
14 Copies